Investigating the Regulatory Pathways of the Mitotic Oscillator Via a High-Throughput Droplet-Based System

by

Shiyuan Wang

A dissertation submitted in partial fulfillment
of the requirements for the degree of
Doctor of Philosophy
(Biophysics)
in the University of Michigan
2024

Doctoral Committee:

Associate Professor Qiong Yang, Chair
Assistant Professor Jordan Horowitz
Professor David Lubensky
Associate Professor Ryoma Ohi
Associate Professor Kevin Wood

Shiyuan Wang

wangshi@umich.edu

ORCID iD: 0000-0001-8676-8720

Dedication

To my family and friends, for all your love and support.

To those who showed compassion and came to my aid in times of need.

Acknowledgements

There are so many great people I want to thank for helping me along this long journey, without whose support I wouldn’t have finished my degree, especially towards the end. I want to thank my family, for supporting me through the years from across the seas. I would like to express my sincere gratitude to my advisor, Dr. Qiong Yang, for your help throughout my graduate studies. This dissertation cannot be completed without your tremendous support. As someone coming directly from their undergraduate studies and with little prior experience, I was able to explore my interests and hone my skills in the lab. I also want to thank my other thesis committee members, Dr. Jordan Horowitz, Dr. David Lubensky, Dr. Ryoma Ohi, and Dr. Kevin Wood for their feedback and their time and efforts on this dissertation. Their insights and suggestions are valuable for course-correcting my research. I have learned a lot from every one of my current and past lab members. To Ye, Zhengda, Meng, and Gembu, thank you for mentoring me and helping me build a fundamental understanding of research; to Owen and Minjun, thank you for your camaraderie through the ups and downs of our frog-related explorations; to Liam, Usha, Yeonghoon, and Derek, thank you for joining in my research project, for doing and continuing the hard work while I could not; and to other members of the lab, Chun-Yen and Franco, thank you for your input throughout the years. Finally, I would like to thank Dr. Sarah Veatch, for your council through the last stretch of my studies, without which I couldn’t have the dedication to finish it all.

Table of Contents

List of Figures

Abstract

This dissertation aims to investigate the properties of the mitotic oscillator and its complex regulatory mechanism. Responsible for the progression of the cell cycle through its various stages, the mitotic oscillator is highly conserved in organisms and is essential for life, however the design principles of the biochemical network behind the oscillator and the significance of its topology are not fully understood. Falling into the "activator-inhibitor" category, the mitotic circuit has a negative-plus-positive feedback structure. To untangle the complex interactions of this circuit, in this work I present a novel droplet-based platform combined with microfluidic techniques where *Xenopus* egg extracts were encapsulated in water-in-oil microemulsions. Our system allows for the fine tuning of all kinds of variables including droplet size and extract content and can reliably reconstitute the cell cycle dynamics. Primary tests using this system indicate that the mitotic oscillators are to a certain extent robust to perturbations while tunable in bi-stability, speed, and accuracy. Experimentations on partial inhibition of the network revealed shortcomings of current cell cycle models, which cannot explain the oscillator's multimodal behavior and thus suggests other essential regulatory pathways. Taking advantage of the setup. I also investigated the oscillator behavior at different energy levels and discovered a non-monotonic response in oscillator speed and accuracy, which points to interesting mechanisms designed to sense and respond to a cell's energy budget.

Chapter 1 Introduction

1.1 The Studies of Biological Oscillators and the Development of the *Xenopus* Egg Extract

Oscillations are prevalent in biological systems. From the single-celled to the most sophisticated organisms, oscillatory behaviors have been observed in a broad spectrum of biological processes, such as neuron firing, heartbeats, cell cycles, menstrual cycles and circadian rhythms. Their ability to keep time is essential to ensuring the correct and timely progression of critical biological events and processing information from both internal and external environments. Defects in these oscillators can cause a variety of diseases from insomnia to cancer[1], therefore mapping out the fundamental design principles of biological oscillators is of great significance to health-related studies.

Although theoretical works on oscillators date back decades, systematic experimental characterization of biological oscillators remains challenging. There are distinct advantages of observing the behaviors of a simulated molecular network over that in an experimental environment: the modeled system is cleaner with no unknown influencing factors; the modeled system has the ability to simultaneously track multiple molecule species with high resolution; and the modeled system allows for fine tuning of certain parameters such as molecular concentration, reaction rate, and even the molecular network topologies. On the contrary, traditional experimental methods include using cell cultures, tissues, whole organisms, or bulk cell extracts[2–4], which typically can only test a few discrete conditions, corresponding to a few points in the theoretical parameter space, and only limited replicates at each condition. When considering that minute changes in parameter can lead to bifurcations, resulting in complete shifts in system behavior, the especially coarse-grained experimental approach risks losing large amounts of intricate changing dynamics in oscillator behaviors. As a result, there is a significant imbalance in abundance between simulated and experimental data. The lack of experimental datasets comparable in size and resolution to simulation results makes it difficult to provide concrete evidence on the reliability of theoretical predictions, the reliability of the models, and according to recent findings the plausibility of the widely accepted network simplifications[5].

This type of mismatch in production power is also present in the subject of this dissertation, the mitotic oscillator, which is responsible for the normal progression of cell division. The regulation network behind the cell cycle has been extensively studied and remains an important field of interest. Pieces of this puzzle have been unveiled by studies done in numerous model organisms, including the budding yeast *Saccharomyces cerevisiae*, the common fruit fly *Drosophila melanogaster*, and mice. The African Clawed Frog, *Xenopus laevis*, is a particularly popular model, especially after Murray developed standard protocols for making various cell-free extracts from *Xenopus* eggs[6]. *Xenopus* egg extracts have made major contributions to the initial discovery and characterization of the mitotic oscillator. For example, Lohka et al. studied the M-phase promoting factor (MPF, or referred to as the cyclinB/Cdk1 complex in this work)[7–10], which was known at the time to induce oocyte maturation. They purified MPF from crushed Xenopus eggs and discovered its kinase activity, indicating that increased protein phosphorylation might be an important step during G2 to M phase transition. Murray et al., inspired by the isolation of MPF, demonstrated the role of cyclin synthesis and degradation in the control of Cdk1 complex activity using CSF arrested extract combined with normal and proteolysis-resistant cyclin B. Other contributions include discoveries in chromosome segregation[11], spindle assembly[12], nuclear transport[13], and chromosome assembly[14,15]. Based on current understandings acquired from previous discoveries in *Xenopus* as well as other model organisms, the correct progression of the cell cycle through its various stages is controlled by a complex network of interacting molecules, with each stage corresponding to a different subgroup of the network, notably revolving around different Cyclin/Cdk complexes (figure 1.1). However, it is bordering impossible to study such a complex system all at once, the modeling of all the species and their interactions is severely limited by current computation powers. Typical studies tend to focus on specific subsets of molecules or cell cycle stages. In line with contemporary studies, this dissertation focuses on the cell cycle clock, which describes the cyclic switching between interphase and mitotic phase during the G2/M transitions and mitotic exits. Due to the periodicity and regularity of this behavior, I hereby define the system involved in this process as a mitotic oscillator. However, even when looking at only this oscillator, there is still a complex network of interactive proteins that oversee the oscillatory process. Previous works have aimed to identify a simplified network including only the essential molecules that impact oscillatory behaviors[16–18]. This simplified network is defined as, and will be referred to as, the mitotic circuit.

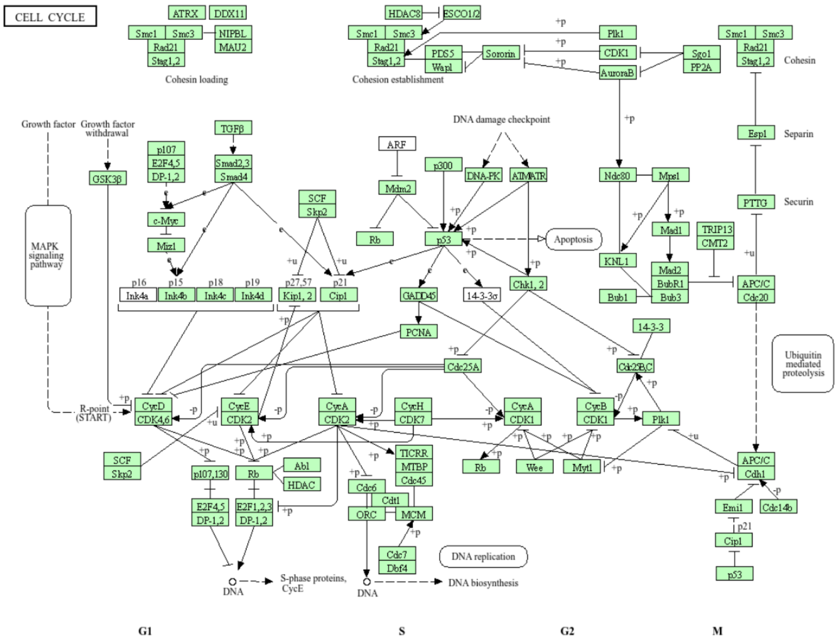

Figure 1.1. The molecular network regulating the various stages of cell cycle.

Reproduced from the KEGG PATHWAY Database[19].

The current widely accepted mitotic circuit (shown in figure 1.2) revolves around a negative feedback loop consisting of the cyclin B-cyclin dependent kinase 1 (Cdk1) complex and anaphase-promoting complex (APC/C), where Cdk1 is a protein functioning as a serine/threonine kinase and APC/C as an E3 ubiquitin ligase that targets cell cycle proteins for degradation. Cyclin B protein can bind and unbind from Cdk1, thus partially activating and inactivating its kinase activity. This circuit has also interdependent double-positive and double-negative feedback loops, involving the protein kinase Wee1, and the phosphatase Cdc25. Wee1 is a protein kinase that inhibits Cdk1 activity by phosphorylating it on two sites, Tyr15 and Thr14[20]. Cdc25 is a phosphatase that activates Cdk1 by dephosphorylating inhibitory residues on the same sites phosphorylated by Wee1[21]. Active cyclin B-Cdk1 activates its activating phosphatase Cdc25 and forms a double-positive feedback loop and inhibits the inhibitory kinase

Wee1, forming a double-negative feedback loop[22]. The double-positive and double-negative feedback loops collectively function as a bistable trigger[23,24]. The E3 ubiquitin ligase APC/C is also activated by the active cyclin B-Cdk1 complex, but the mechanism is still not well understood. Active APC/C polyubiquitinates the mitotic cyclin, tagging them for degradation by the proteasome, thus deactivating the cyclin B-Cdk1 complex. The cyclin B-Cdk1 complex is mainly responsible for the G2 to M phase transition in the cell cycle. The activation of Cdk1 drives the cell cycle into mitosis, while the activation of APC/C drives the cell back out of mitosis. Although the required minimum construction of an oscillator is only a time-delayed negative feedback loop, the extract structure in the mitotic circuit is still highly conserved in a variety of organisms, the significance of which is not fully understood. Some theoretical works have postulated the functions of certain components of the network. Tsai et al. proposed that the existence of positive feedbacks enables the oscillator to alter it frequency while maintaining a relatively constant amplitude[22]; Yang et al. proposed that the interactions between Cdk1 complex and Wee1/Cdc25 allows the system to act as an ultra-sensitive switch, which leads to ultrafast switching between interphase and mitotic phase[25]. Li et al. did a more comprehensive scan of different network topologies in addition to the mitotic circuit. The networks are treated as nodes (the molecules) and vertices (the interaction between molecules) and ranked according to their performance. They found that incoherent inputs, i.e. nodes receiving both positive and negative regulations, increase the molecular networks' tunability (the system's ability to alter its frequency while still maintaining it oscillatory status) and robustness (the system's ability to remain oscillating with parameter changes)[26].

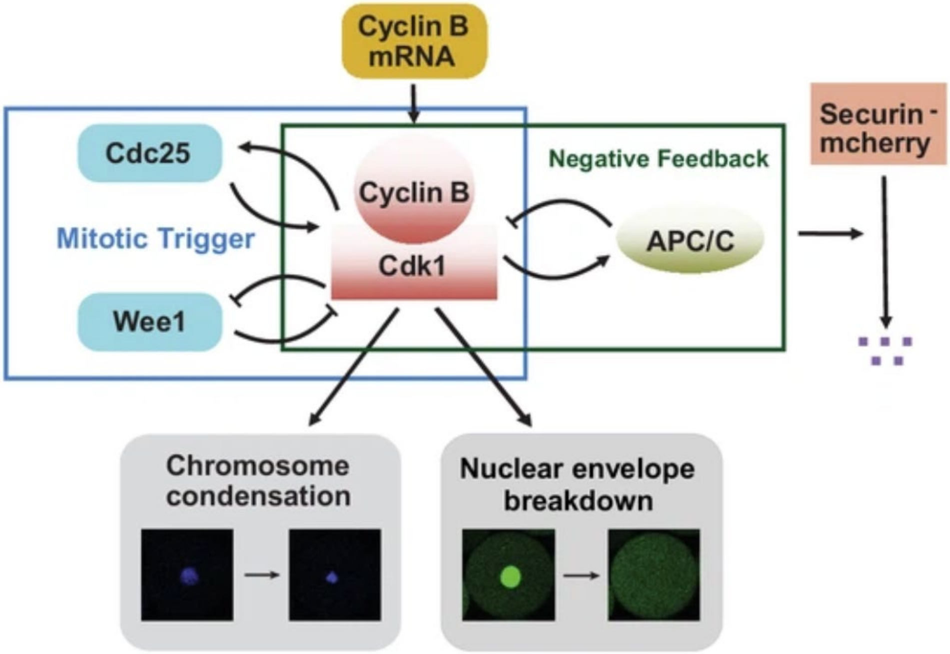

Figure 1.2 Schematic of the mitotic circuit.

Varius attempts have been made to model the mitotic circuit. Some examples include Novak and Tyson's detailed mass action 10-equation model[17] and their simplified 2-equation model based on Goldbeter-Koshland kinetics[18]; Yang and Ferrell's 2-equation model using Hill function-based rate equations[25]; and Cao et al.'s activator-inhibitor model[27]. In addition to studying the inherent properties of the oscillator, Certain explorations have been done to probe the circuit's ability to respond to environmental cues. Cases relative to the scope of this dissertation are focused on the oscillator's response to changing energy landscapes. Theoretical predictions show that the availability of free energy can significantly impact oscillator behavior, including the ability to oscillate, the switching threshold of total Cdk1 concentration[28], and the oscillating precision[27]. However, in most of the studies listed above, due to the lack of experimental evidence compared to the plethora of theoretical predictions, it remains to be seen whether the simulations faithfully recreate actual cellular dynamics. A systematic mapping of oscillator behavior and its response to perturbations is desperately needed for further understanding of the network and an experimental setup capable of producing satisfactory datasets is essential. Therefore, one of the main goals of this dissertation is to construct an experimental platform that can bridge the gap between the production capabilities of experimental and theoretical studies. Building upon the successful development of such a platform, I will further compare the experimental observations and theoretical predictions, and conduct an evaluation of popular cell cycle models concerning their ability to faithfully reproduce oscillatory dynamics.

1.2 Engineering Spatiotemporal Organization and Dynamics in Synthetic Cells

To address the previously mentioned lack of experimental tools, synthetic biology has recently become a popular area of research. Previous works in biochemistry and cell biology have revealed functional components involved in various biological processes. However, recreating any of these processes *in vitro* remains challenging. Currently, the development of synthetic cells, i.e. different kinds of encapsulated biochemical systems that can recapitulate one or more specific functions of a natural cell[29–31], provided unprecedented opportunities to untangle complex biochemical networks. The design of synthetic cells aims to recreate mainly 2 essential features of real cells—compartmentalization and spatiotemporal dynamics[32]. To achieve compartmentalization, special attention has been paid to the construction of a synthetic boundary to mimic the cell membrane. phospholipids, polypeptides, block copolymers, and polypeptide copolymers have all been utilized to form the membrane of synthetic cells[33–35]. Building upon these previous achievements and the need addressed above, my study aims to develop a system that allows quantitative manipulation and high yield. A droplet-based system that can generate artificial "cells" is selected as the blueprint for the new platform. The choice is made due to the need to generate sample replicates with high speed and high yield. A fluorosurfactant with a molecular structure functionally similar to lipids, having one hydrophobic end and one hydrophilic end, was used to create a single layer boundary for the water-in-oil droplet emulsion. Unlike the lipid bilayer of cell membrane, the single layer doesn't allow molecules to permeate into or out of the droplets or anchoring of membrane proteins, but this discrepancy is justifiable considering the scope of my studies, because although there is some evidence of the mitotic network communicating with other intercellular signaling pathways, such as the segmentation clock[4], it is not the focus of our study, therefore to possibly reduce influencing factors, selective permeability and membrane transportation that's made possible in other boundary generating methods is excluded our setup.

Regarding the reconstitution of cellular dynamics, considering most biological processes are regulated by a sophisticated regulatory network that involves a complex network of genes, proteins, and signaling molecules, it is difficult to construct the system by the elements from the bottom-up. To recreate essential cellular functions ranging from transportation of nutrients to sensing of physical and chemical information, attempts have been made in combining available components in cell-free extracts and additional machinery in the same system. Both prokaryotic and mammalian systems have successfully expressed structurally intact proteins[33,36]. Considering temporal dynamics, significant achievements have been made reconstituting the cell cycle[37,38]. Different systems have been proven to mimic both cell cycle oscillations and divisions in synthetic cells, one of which being the *Xenopus laevis* egg cytoplasm with recombinant proteins, mRNAs, and DNAs. The cytoplasm can be activated by the addition of Calcium ionophore, which mimics the release of Calcium ions from the mitochondria after the fertilization process. Cell cycle-related proteins are therefore initiated to oscillate, although the cytoplasm is not actually developing into an embryo. Fluorescent proteins with highly selective targets allow for live reporting of cell cycle dynamics over time.

Regarding spatial dynamics, although reconstitutions including protein organelles[39], chromosomal organization[40], DNA segregation[41], and components of the cell cycle[37,42], have been achieved in cell-free systems, introducing spatial heterogeneity risks introducing a whole new set of variables that can potentially alter dynamics of the mitotic circuit[43,44]. Spatial difference in molecular concentration can also lead to erroneous estimations of molecular reaction rates and synthesis/degradation rates, so in the scope of this study, I only proved that the droplets have the capability of reproducing spatial dynamics during the initial stages of developing the experimental platform, but when conducting quantitative studies, steps have been taken to ensure that individual droplet contents are homogeneous. For the same reason of eliminating as many interfering factors as possible, even though the mitotic circuit components go through oscillations inside droplets, spatial changes including cytokinesis are not present due to the intention chemical destruction of the cytoskeleton by not constructing a functional cell membrane and blocking the formation of actin filaments with Cytochalasin B.

1.3 Summary of Thesis Questions, Designs, and Results

In this chapter, I reviewed previous research on the mitotic oscillator and the efforts to build functional synthetic biological systems. The first step of my study focuses on the development of a high-throughput *in vitro* system to reconstitute mitotic oscillations and demonstrating its various applications in studying the properties of the oscillator. In chapter 2 I will discuss the details of the system and its combination with novel microfluidic techniques, as well as some general characterizations of the droplets produced. Some primary findings made with this experiment setup indicate the droplets can faithfully reconstitute cell-cycle events and are thus an ideal platform for further studies. The results are described in published works *A robust and tunable mitotic oscillator in artificial cells*[38], *Reconstitution of Cell-cycle Oscillations in Microemulsions of Cell-free Xenopus Egg Extracts*[45], *Building Dynamic Cellular Machineries in Droplet-Based Artificial Cells with Single-Droplet Tracking and Analysis*[46], and *Plug-in tubes allow tunable oil removal, droplet packing, and reaction incubation for time-controlled droplet-based assays*[47]. In chapter 3 I will demonstrate the mitotic oscillator's highly tunable nature in response to perturbations. I comprehensively mapped the cell-cycle period landscape by continuously tuning single-cell parameters in multiple dimensions with full dynamic ranges to provide an experimental framework for global parameter space scans. I also made new observations that via inhibition of the Cdk1-counteracting phosphatase PP2A, monomodal or bimodal distributions can be seen across varying inhibition levels, underscoring the complex nature of cell cycle regulation. The data allowed us to challenge existing models and refine a new model that matches the observed response. The results are described in the published manuscript *Comprehensive Parameter Space Mapping of Cell Cycle Dynamics under Network Perturbations*[48]. In Chapter IV, I will present an ongoing work studying the energy-dependent behavior of the mitotic oscillator. By tuning the ATP content in extracts, I observed an intriguing non-monotonic response in oscillation characteristics to varying energy landscapes. The oscillator is able to adjust its speed and accuracy based on the available energy budget, however further research is needed to untangle the mechanisms that allow the oscillator to self-regulate in response to intracellular environments. A manuscript describing this work is in preparation.

Chapter 2 The Development of a Droplet-Based Microfluidic System to Reconstitute Mitotic Events and Fine-Tune the Mitotic Circuit

2.1 Introduction

Experimental platforms, whether whole organisms, isolated tissues or cell cultures, can be roughly categorized as either *in vivo* or *in vitro*. Both systems have been extensively used to study diseases and complex biological processes, and both have their own advantages and shortcomings. For example, *in vivo* testing is considered more representative of physiological conditions thus more reliable, however conducting experiments and acquiring statistically significant results in certain *in vivo* systems can be costly and resource consuming. Moreover, existing *in vivo* models can be too complex, containing more interfering factors when studying a specific pathway or circuit. Tried and tested *in vitro* systems have fewer such restrictions, allowing researchers to strip the complex cellular environment down to the bare necessities, and are open to all kinds of quantitative manipulations not possible in *in vivo* systems. Even though it is difficult for *in vitro* systems to wholly reproduce dynamic behaviors of living cells *in vitro*, it is possible to reconstruct certain aspects of a dynamic system of interest.

Many complex biological processes and their regulations concerning the cell cycle can be reconstituted in vitro using extracts made from *Xenopus laevis* eggs. Cytoplasmic extracts from *Xenopus* eggs have made major contributions to the initial discovery and characterization of the central cell-cycle regulators including the protein complex cyclin B1-Cdk1 and the anaphase-promoting complex or cyclosome (APC/C). Cell-free extracts have also been used to investigate downstream mitotic events such as spindle assembly and chromosome segregation. Today, *Xenopus* extracts are still widely used for studying the cell cycle, DNA replication and repair, spindle assembly and microtubule motor function. One specific type of *Xenopus* extract, the cycling extract, is the cytoplasmic extract prepared from *Xenopus* eggs that goes through the rapid cell division observed in early embryo development. The oscillating dynamics is achieved by "activating" the extract with Calcium ionophore, which mimics the calcium ion release after fertilization. Cycling extract is proven to have the ability to reconstitute mitotic cycles in *in vitro* environments[38], and thus is a powerful tool to study cell cycle. It has been used to investigate diverse cell cycle events such as chromosome morphology changes, nuclear envelope breakdown and reformation, DNA replication, spindle assembly and microtubule dynamics, and the budding and fusion of carrier vesicles involved in membrane transport. However, for most previous *in vitro* reconstitutions of *Xenopus* cycling extracts, tests are performed in well-mixed bulk solutions and exhibit only damped oscillations[49,50], possibly due to the desynchronization of multiple oscillators, making it difficult to study cell cycle dynamics. These bulk extracts also lack the ability to recreate the spatial organization achieved by functional compartmentalization in real cells. The dramatic disparity in physical dimensions between bulk extract and the real cell also casts shadow on whether the phenomena observed in bulk extract is comparable to that in actual cells.

Therefore, to our interest, an *in vitro* compartmentalized and easily manipulatable biochemical reaction system is needed to study the dynamics of biochemical oscillators. To this end, we developed a high-throughput artificial mitotic oscillation system by encapsulating

Xenopus cycling extracts in cell-like droplet emulsions. In the early developmental phase, the droplets were generated by simply creating an emulsion of the extract-oil mixture with a vortex machine[51], which yielded droplets of different sizes. This method was subsequently replaced by droplet generation with microfluidic devices, which yielded extremely uniform droplets. The droplets were loaded into a Teflon-coated 2-dimensional chamber, and the cell cycle dynamics were recorded with long-term time-lapse fluorescence microscopy. These droplet-based cells exhibit undamped, self-sustained oscillations that last for days, offering significant advantages than their bulk counterparts and outperforming the current existing *in vivo* and *in vitro* systems.

To enable real-time tracking of cell cycle dynamics, fluorescent reporters have been added to the droplets as needed. We have developed and used multiple reporters to label different cellular structure and components of the mitotic circuit. The fluorescence profile of each droplet was analyzed to obtain information of period, amplitude, number of cycles and droplet size, etc. The continuous output of fluorescent signals from reporters allowed us to measure the cell cycle dynamics in real time and explore the relationship between the variables of interest and the cell divisions quantitatively.

This chapter is adapted from the published articles *A robust and tunable mitotic oscillator in artificial cells*[38], *Reconstitution of Cell-cycle Oscillations in Microemulsions of Cell-free Xenopus Egg Extracts*[45], *Building Dynamic Cellular Machineries in Droplet-Based Artificial Cells with Single-Droplet Tracking and Analysis*[46], and *Plug-in tubes allow tunable oil removal, droplet packing, and reaction incubation for time-controlled droplet-based assays*[47]. My contributions to these projects include experimental platform design; experiment design; performing experiments; data collection, processing, and analysis; analysis script writing; and writing the manuscripts.

2.2 Cycling Xenopus Extracts Preparation

We optimized the cycling extract preparation process based on Murray's protocol for the extract preparation[45], some major changes include: 1) Xenopus egg activation: eggs were activated with Calcium ionophore A23187 (0.5 µg/mL) rather than electric shock to mimic the rapid release of Calcium after egg fertilization; 2) egg crushing method: we used long snap-cap LDPE tubes instead of Eppendorf tubes to more easily separate different layers after centrifugation, especially in small quantities; 3) extract separation: instead of extract the cytoplasm by syringes, which may decrease extract activity caused by potential shear forces, we cut out specific layers of the tubes with razors; 4) buffer removal: to preserve extract activity, we avoided the use of silicone oil during the buffer removal step.

Two mature female *Xenopus laevis* between over 12 months old were injected with 100 IU Human Chorionic Gonadotropin (HCG) one to two weeks prior to the experiment date. On the eve of the experiment, these *Xenopus* frogs were injected with 500 IU HCG to induce egg laying 12-16 hours later. Before the extract preparation, frogs were gently squeezed for eggs. The dorsal side was massaged, and gentle pressure was applied to induce egg laying. This step was repeated over 10-minute intervals until a desired amount of eggs were collected. Eggs laid before the arrival of staff were usually discarded as their ability to reconstitute cell cycle is proven to be poor. Eggs were squeezed into 100 mL petri dishes containing 1× MMR buffer and inspected. Batches of eggs that were stringy or had unclear boundaries between animal and vegetal poles or irregular white spots on top of animal poles were discarded. The frogs were allowed to rest for three months later until the next egg harvest.

The batch of eggs presenting a homogeneous population of oocytes with clearly differentiated animal and vegetal poles was chosen and transferred into a 600 mL beaker. Excess MMR buffer was poured out and 250 mL of 2.2g/100 mL cysteine (pH=7.8) in 1× extract buffer was added to eggs gently to de-jelly the transparent outer coat. The eggs were shaken vigorously by hand and inspected regularly to check the removal of the jelly layer. The cysteine solution was immediately removed when the eggs were visibly touching each other. The eggs were then washed with 1L 0.2× MMR solution over four washes. Meanwhile, eggs that turned white were discarded using a glass Pasteur pipette. The MMR buffer was then poured out and eggs were supplied with 200 mL 0.1 µg/mL calcium ionophore A23187 solution in 0.2× MMR buffer for activation. A glass pipette was used to stir the eggs gently. The eggs were checked regularly to determine the activation efficiency. For the well-activated eggs, there is a clear contraction of the animal pole toward the white spot on the top of the eggs. Most of the healthy eggs would self-orient with animal poles up and vegetal poles down. The overall activation efficiency can be estimated from the percentage of eggs with the vegetal side down. The whole activation process should ideally take less than 3 minutes. The activated eggs were then washed twice with 50 mL of 1× extract buffer supplemented with protease inhibitors (10µg/mL of leupeptin, pepstatin, and chymostatin each). Eggs were carefully transferred to 0.4 mL snap-cap tubes and then packed using a tabletop microcentrifuge at 200× g for 60 seconds, and then 600× g for 30 seconds. To reduce the dilution of extracts, extra extract buffer on top of the eggs was removed using a glass Pasteur pipette after each spin. The eggs were crushed at 20,000× g for ten minutes at 4°C in a centrifuge with a swinging bucket rotor. Typical tubes after centrifugation would have clear layers of dark pigment, yellow heavy membrane, clear cytosol, and light-yellow lipid layers from bottom to top. The tubes were cut to get the crude cytosolic extract in the middle layer. The crude cytoplasm was transferred into new 0.4mL tubes and supplemented with protease inhibitors. They were then spun at 20,000× g again at 4°C for 5 minutes. The cutting and extracting process was repeated after centrifugation to further remove any impurities and the extract was supplied with protease inhibitors again. The final extract was stored on ice ready for experimentation.

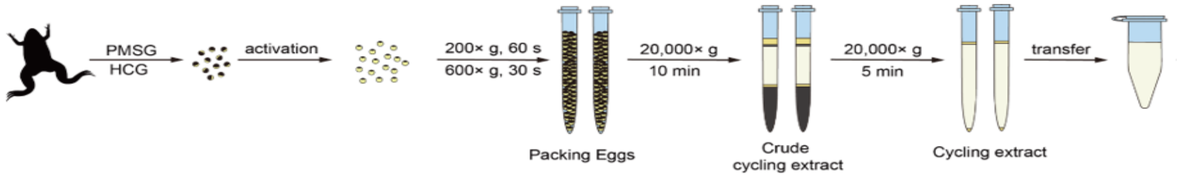

Figure 2.1 Schematic of Xenopus extract preparation.

Xenopus eggs were freshly collected from a female frog. The collected eggs were packed through low-speed centrifugation and crushed by high-speed centrifugation.

2.3 Droplet Generation and Imaging

Freshly prepared extracts were kept on ice while being supplied with different drugs and fluorescent markers as needed. For cell cycle dynamics, multiple fluorescent reporters were used for different research needs. NLS (nuclear localization signal)-tagged proteins, such as NLS-GFP, were used to mark the nuclear membrane when sperm DNA is added to the droplets. Securin tagged proteins such as securin-CFP and securin-mCherry were initially used to report Cdk1 activities as both securin and Cdk1 are substrates of APC/C[38,48]. The securin proteins were replaced when a Cdk1 specific FRET sensor was developed[44]. Cyclin tagged proteins such as cyclin-YFP were used to record cyclin activities[38,48].

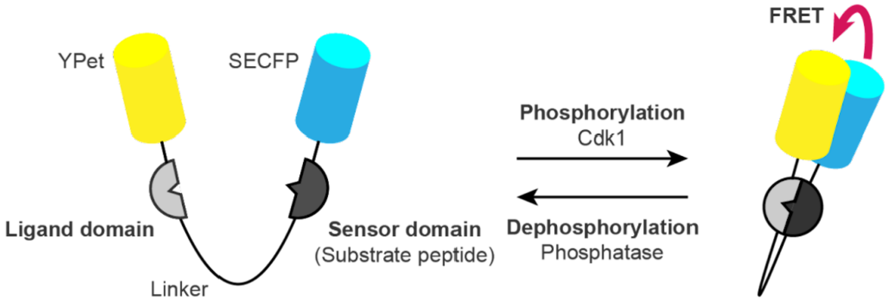

Figure 2.2 Scheme of Cdk1-EV FRET biosensor.

FRET efficiency reversibly increases or decreases via phosphorylation by Cdk1 and dephosphorylation by antagonistic phosphatases (PP1/PP2A). reproduced from Maryu et. al, 2022.

2.3.1 Droplet Generation with a Vortex Machine

The extracts were mixed with 2% Perfluoropolyether-polyethylene glycol (PFPE-PEG) surfactant oil to generate droplets. In the initial phase we applied a simple vortexing method to create droplets with a broad size distribution. 20 µL cycling extracts supplied with multiple biochemical molecules suspended in 200 µL 2% PFPE-PEG surfactant oil were emulsified by a vortex machine at a speed of level ten for 3 seconds. By adjusting the vibration speed and ratio between the aqueous and oil phase, we can obtain droplets of various radii, ranging from 20 µm to 500 µm. However, the varying sizes of droplets may pose unexpected variabilities when quantifying certain characteristics of the oscillator that are sensitive to reaction volumes.

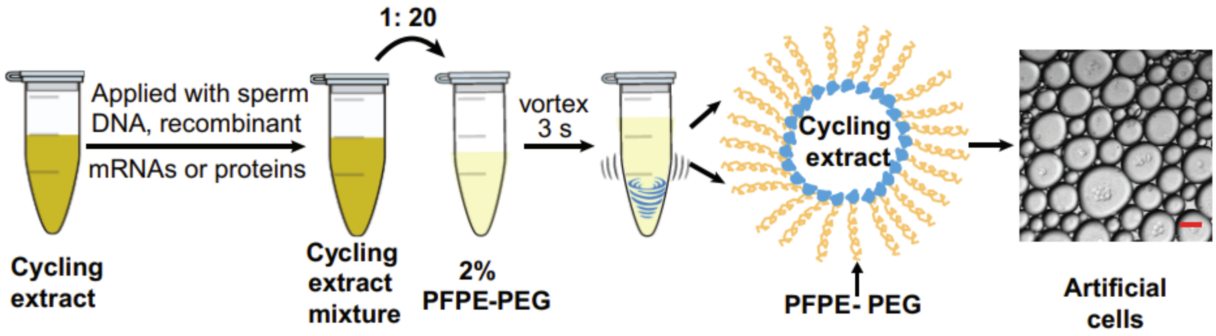

Figure 2.3 Experimental procedures for generation cycling extract.

Cycling Xenopus extracts are supplemented with various combinations of recombinant proteins, mRNAs, and de-membraned sperm DNAs, which are encapsulated in 2% PFPE-PEG oil microemulsions. Scale bar: 100 μm.

2.3.2 Droplet Generation with Microfluidic Devices

Considering the shortcomings of the vortexing method, we introduced a microfluidic system to our experimental setup[46]. Although the application of droplet microfluidics has grown exponentially in chemistry and biology over the past decades, robust universal platforms for routine generation and comprehensive analysis of droplet-based artificial cells are still rare. Our system enables full automation in tracking single droplets with high accuracy, high throughput, and high sensitivity. After the introduction of microfluidic techniques, we used custom PDMS flow-focusing devices to generate droplets of a uniform size. An SU-8 mold on silica wafer was first fabricated to replicate PDMS slabs (~5 mm thick) with microfluidic channels (40μm in depth) via traditional photolithography and soft lithography methods. PDMS slabs were fabricated with the mold by pouring PDMS and baking in an oven for 3h at 60°C or 24h at room temperature. After the slabs were cut off the mold with a razor, fluidic access holes and the droplet collection reservoirs were then made by punching through the PDMS slabs using 0.7 mm dispensing tips and 4 mm biopsy punches respectively. The thick slab was then bonded to a glass slide spin-coated with a thin and half-cured PDMS layer (~80µm), the assembled slab and slide was baked for an additional 1h at 60°C. The microfluidic devices were fabricated with 1, 2, or 3 inlets, which allows for mixing of different extracts with different contents and also fine tuning of certain chemical of molecular concentrations in the extract.

To generate droplets, the oil and aqueous phases were driven into the PDMS device with a multi-channel microfluidic flow controller. Microbore PTFE tubings (0.3 mm i.d., 0.76 mm o.d.) were used for fluidic connections. The generated droplets were first pooled in the reservoir, then loaded into thin glass tubes, which eliminated the need for space by microwells or microtraps fabricated on a chip and the complexity of manipulating fluid dynamics in microchannel networks. The inner dimensions of the glass tubes (inner dimension: 100µm in height, 2mm in width) were selected to force the droplets to settle in a single layer, forming an almost 2D array.

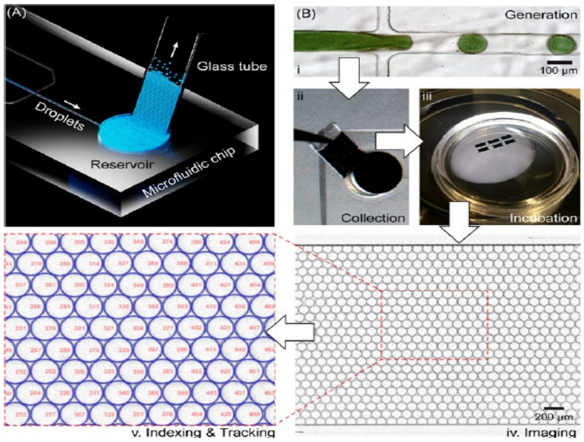

Figure 2.4 Droplet microfluidic platform.

(A) Schematic diagram showing droplet generation and loading into a glass tube: a reservoir opened at the end of a flow-focusing device with a diameter of 3 mm; the tube width is 2.1 mm. The arrows indicate the flow direction of droplets. (B) Droplet microfluidic workflow: droplet (i) generation;(ii) collection; (iii) incubation; (iv) imaging (e.g., a phase-contrast image showing the collected water droplets in a glass tube); and (v) bright-field indexing and tracking.

The glass tubes were pre-cut into 3−5mm pieces using a ceramic scoring wafer and then placed in a vacuum desiccator with vaporized trichloro (1H,1H,2H,2H-perfluorooctyl) silane for at least 1.5h to create a hydrophobic surface. The hydrophobic layer prevents the droplets from attaching to the tube wall. To assist the vaporization of Trichloro (1H,1H,2H,2H-perfluorooctyl) silane, A 1.5 mL Eppendorf tube containing 30 µL Trichlorosilane was placed in a heating block preheated to 95°C. The heating block and the tube were then placed in a vacuum desiccator with the glass tubes.

When droplets were generated, they were pooled in a reservoir in the PDMS device, which were then loaded into the glass tubes by dipping the tube into the reservoir. The tubes were only partially filled with droplets so as not to overload the glass chamber, which would result in more than one layer of droplets, creating difficulties during the segmentation step. After the droplets were loaded into the glass tubes, the tubes were immersed in a glass-bottom Petri dish filled with mineral oil to prevent sample evaporation.

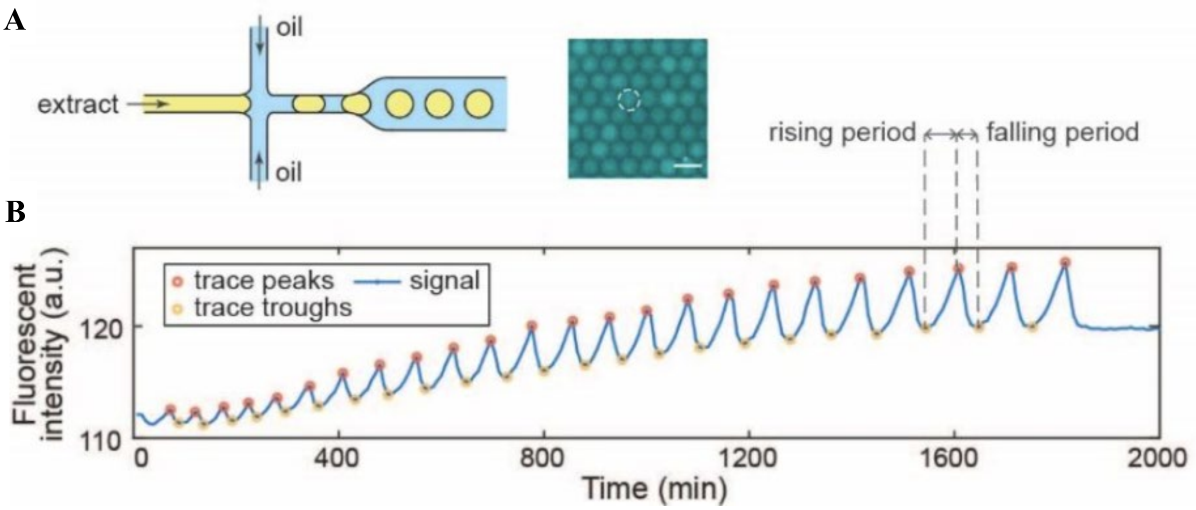

Figure 2.5 Single channel microfluidic device for droplet generation.

(A) Scheme of a single channel microfluidic device and the resulting droplets generated and collected in a glass chamber. Scale bar: 100 µm. (B) an example track of an individual droplet over time with peaks and troughs selected.

Images of droplets were captured by a digital CMOS camera installed on an inverted fluorescence microscope, which was controlled by Micro-Manager, an open-source microscopy software, for automatic stage positioning and droplet imaging. Corresponding filter cube or filter wheel was used to record fluorescent signals as well as brightfield images for subsequent analysis.

2.4 Data Analysis

Custom MATLAB scripts were used to analyze the time-lapse videos. The droplets were segmented and tracked using bright field images. Segmentation was achieved by a watershed algorithm with seed generated from the Hough circle detection. Tracking was performed by maximizing the segmentation feature correlation between two consecutive time frames. Although the script included tunable parameters such as droplets area, eccentricity, or maximal permitted positional shift, to improve tracking results, some droplets will inevitably be wrongly tracked caused by unideal conditions such as sudden movements between frames, droplet overlap caused by overcrowding, multiple droplets merging into one, droplet deformation, or extract darkening caused by apoptosis. These tracks were removed manually after inspection during subsequent analyses. Statistics involving useful information for each track over time were exported as tables, including the coordinates and areas of droplets, mean intensities of the fluorescent channels, the standard deviations of the intensities of the channels. The volume of a droplet was calculated using the formula proposed by the study of Good et al.[52].

The noise in the temporal profiles of mean fluorescent intensities poses difficulty for subsequent analysis. The whole imaging area had similar levels of fluctuation for each frame, which was likely caused by instrument error. Thus, we calculated the mean background intensity by manually selecting 3 blank rectangular areas in the field of view, calculating the mean intensity of the selected areas in each frame, then subtracting the mean from the measured intensity of our droplets at each frame to eliminate the noise.

For period calculation, a peak/trough finding algorithm was used to automatically detect peaks and troughs in the temporal profiles of the desired mean fluorescent intensity. To make sure the behaviors of oscillators were accurately detected, manual checking and correction was applied. The results were then exported as tables available for further statistical analysis.

2.5 Application of The Droplet System by Reconstituting Biological Processes in Artificial Cells

Our pipeline was applied to the study of the mitotic oscillator, which regulates the cell cycle. Spontaneous progression of cell cycles represents one of the most extensively studied biological oscillations. Detailed dissections of the regulatory circuits in these extracts have revealed architecture of interlinked positive and negative feedback[16,24,25,49,53–58]. Such interlinked feedback loops are also found in many other biological oscillators[59–62] and have been shown computationally to play an important role in achieving the essential clock functions such as robustness and tunability[22]. These studies have stimulated major interests in quantitative characterization of clock functions, for which an experimental platform is still lacking.

2.5.1 The Oscillator Reliably Drives the Periodic Progression of Multiple Mitotic Events

To examine the functionality of the droplet mitotic system, we added de-membranated sperm chromatin (to mimic the chromosomal dynamics during cell cycle), purified green fluorescent protein-nuclear localization signal (NLS-GFP), securin-mCherry mRNA and Hoechst 33342 dye to the cytoplasmic extracts. We demonstrated that the system is capable of reconstructing at least three cell cycle-specific events in parallel while alternating between interphase and mitosis. This autonomous alternation of distinct cell-cycle phases is indicated by securin-mCherry, which is synthesized by the extracts' own translation machinery and degraded periodically via APC/C marking. In interphase, the presence of sperm chromosomal DNA, labeled by Hoechst, initiatives the self-assembly process into a nucleus, upon which GFP-NLS protein was imported through the nuclear pores. The localization of Hoechst and GFP-NLS thus coincide in the interphase nucleus. As the artificial cell enters mitosis, the chromosome condenses resulting in a tighter distribution of Hoechst, while the nuclear envelope breaks down and GFP-NLS is quickly dispersed uniformly in the whole droplet. The time courses for these processes were analyzed, indicating that the chromosome condensation and nuclear envelope breakdown (NEB) happened almost at the same time, while securin degradation lags these two processes at each cycle. All together, these experiments showed that the droplet system successfully reconstituted a cell-free mitotic oscillator centered on Cdk1 and APC/C that can reliably drive the periodic progression of downstream events including chromosome morphology change and nuclear envelope breakdown and reassembly, reproducing what occurs *in vivo*.

We have successfully reconstituted the dynamics of nucleus during cell cycle, however the spatial-temporal dynamics introduced by nuclei, such as the transport of Cdk1 complex into and out of the nucleus at different cell cycle stages, might bring unnecessary complexities into the system, therefore subsequent experiments all used droplets with homogenous contents with no sperm chromatin added.

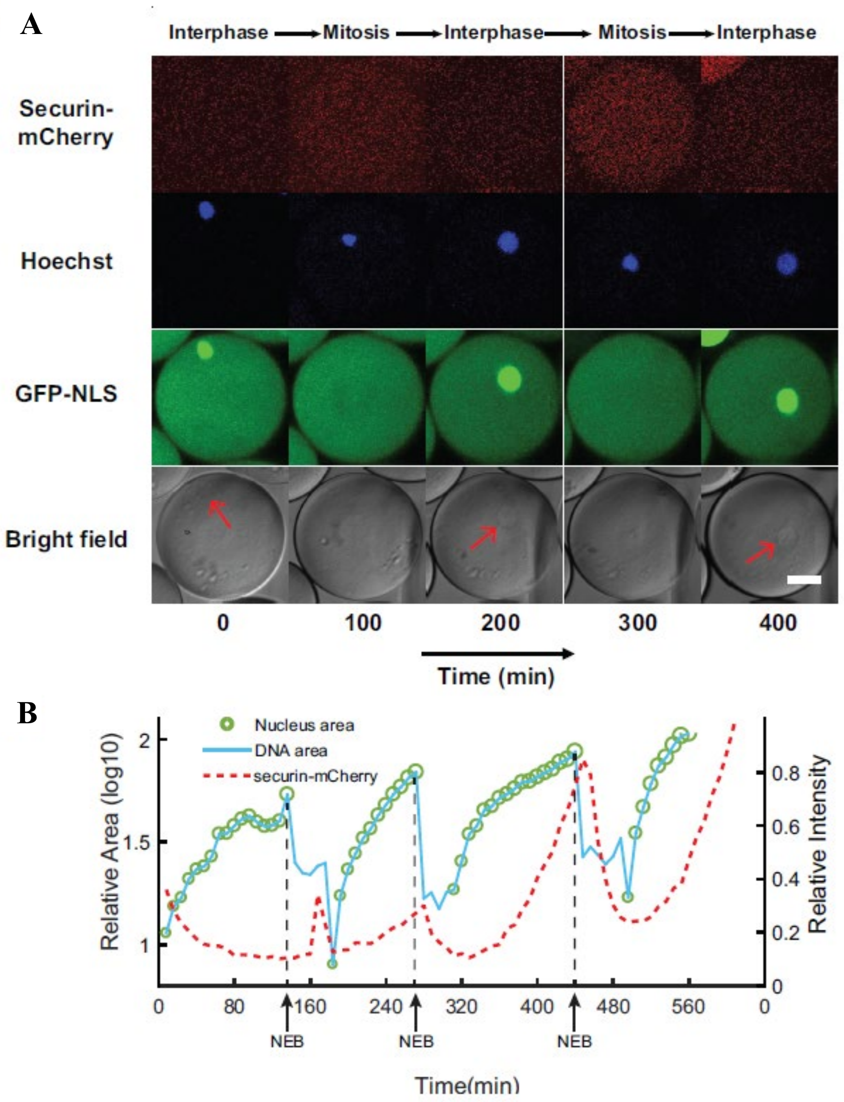

Figure 2.6 Reconstitution of cell cycle events in droplets.

(A) Snapshots of a droplet were taken periodically both in fluorescence channels (top three rows) and bright field (the last row). The cyclic progression of the cell cycle clock and its downstream mitotic processes are simultaneously tracked by multiple fluorescence reporters. The clock regulator APC/C activity is reported by its substrate securin-mCherry, chromosomal morphology changes by the Hoechst stains, and NEB by GFP-NLS. Nuclear envelopes (red arrows) are also detectable on bright field images, matching the localization of GFP-NLS indicated nuclei. Scale bar is 30 mm. (B) Multi-channel measurements for the droplet above. The nucleus area (green circle) is calculated from the area of the nuclear envelope indicated by GFP-NLS, noting that the areas of the green circles are also scaled with the real areas calculated for the nuclei. DNA area curve (blue line) shows the chromosome area identified by Hoechst 33342 dye. Chromosome condensation happens almost at the same time as the nuclear envelope breaks down (black dashed line). The red dashed line represents the intensity of securin-mCherry over time, suggesting that degradation of the APC/C substrate lags NEB consistently at each cycle.

2.5.2 The Oscillator Is Effectively Tunable

The ability to adjust frequency is an important feature shared by many oscillators[22]. Here, we demonstrated that the present system provides an effective experimental solution to the study of tunability of the clock. To avoid any interference from the complicated nuclear dynamics, we reconstituted a minimal mitotic oscillatory system which, in the absence of sperm chromatin, formed no nuclei. This simple, cytoplasmic-only oscillator produced highly robust, undamped, self-sustained oscillations up to 32 cycles over a lifetime of 4 days, significantly better than many existing synthetic oscillators. To modulate the speed of the oscillations, we supplied the system with various concentrations of purified mRNAs of full-length cyclin B1 fused to YFP (cyclin B1-YFP), which function both as a reporter of APC/C activity and as an activator of Cdk1. A droplet supplied with both cyclin B1-YFP and securin-mCherry mRNAs exhibited oscillations with highly correlated signals, suggesting that both are reliable reporters for the oscillator activity.

With an increased concentration of cyclin B1-YFP mRNAs added to the system, we observed a decrease in the average period, meaning that a higher cyclin B1 concentration tends to speed up oscillations. However, the average number of cycles was also reduced with increased cyclin B1 concentrations, resulting in a negative correlation between the lifetime of oscillations and the amount of cyclin B1 mRNAs. The extracts will eventually arrest at a mitotic phase in the presence of high concentrations of cyclin B1.

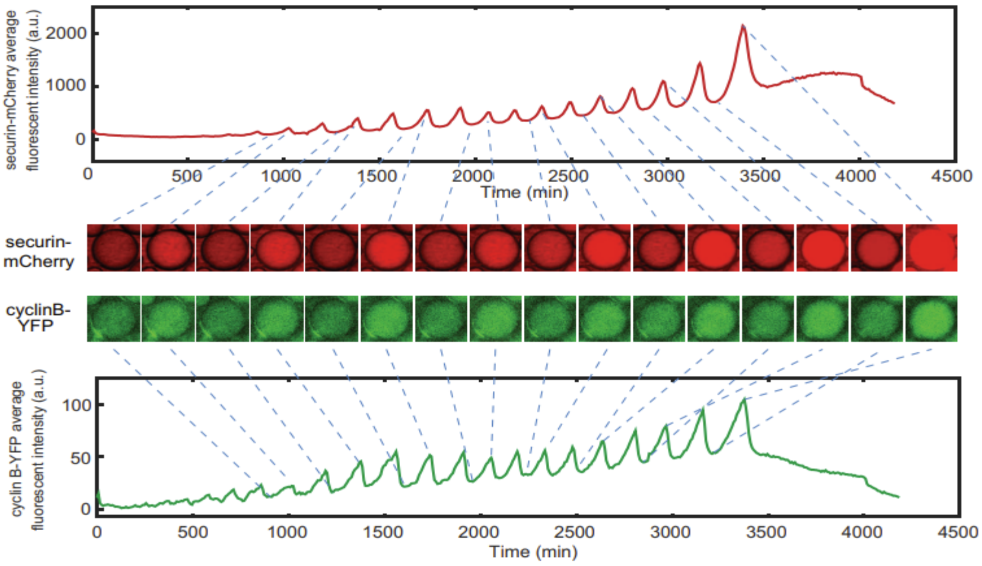

Figure 2.7. Simultaneous measurements of fluorescence intensities of securin-mCherry (upper panel) and cyclin B-YFP (lower panel), showing sustained oscillations for about 58 hr.

The mRNA concentrations of securin-mCherry and cyclin B-YFP are 10 ng/mL and 1 ng/mL. The series of mCherry and YFP images correspond to selected peaks and troughs in the time courses of fluorescence intensities. The two channels have coincident peaks and troughs for all cycles, suggesting that they both are reliable reporters for the cell cycle oscillator.

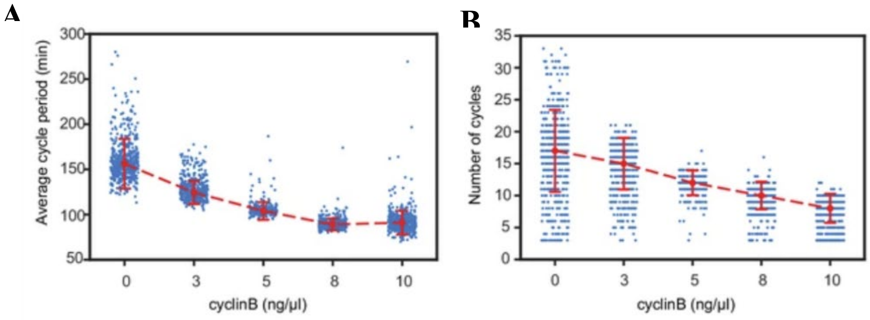

Figure 2.8. The oscillator is tunable in frequency (A) and number of cycles (B) as a function of the concentration of cyclin B mRNAs.

Cyclin B not only functions as a substrate of APC/C but also binds to Cdk1 for its activation, functioning as an 'input' of the clock. The cell cycle periods are shortened by increasing the mRNA concentrations and the number of total cell cycles is reduced in response to increasing cyclin B mRNA concentrations. Each data point represents a single droplet that was collected from one of the loading replicates. Red dashed line connects medians at different conditions. Error bar indicates median absolute deviation (MAD).

2.5.3 The Behavior of The Single Droplet Oscillator is Size-Dependent

With the vortexing method, droplets were generated with radii ranging from a few µm to 300 µm, enabling characterization of size-dependent behaviors of cell cycles. At the scale of a cell, the dynamics of biochemical reactions may become stochastic. Although stochastic phenomena have been studied extensively in genetic expressions, studying a stochastic system that is out of steady state can be challenging in living organisms due to low throughput and complications from cell growth, divisions and other complex cellular environments. These limitations can be overcome by reconstitution of in vitro oscillators inside cell-scale droplets, which are in absence of cell growth and divisions. Parallel tracking of droplets also enables high-throughput data generation for statistical analysis. In vitro compartmentalization of molecules, especially rate-limiting molecules such as cyclin B1 mRNAs, into cell-sized droplets may have a major effect on the reaction kinetics of cell cycles. The smaller the size of a droplet, the smaller the copy number of molecules encapsulated inside the droplet and the larger the inherent stochasticity of biochemical reactions. Additionally, the partition errors of these molecules resulting from compartmentalization may further contribute to the variations of droplet behaviors in a size-dependent manner. Our results showed that smaller droplets led to slower oscillations with a larger variance of the periods, consistent with the size effect reported on an in vitro transcriptional oscillator[63].

We also observed a reduced number of oscillations and a smaller variance of the cycle number in smaller droplets. Interestingly, these size effects become less dramatic for droplets with larger sizes or with higher concentrations of cyclin B1 mRNAs. Therefore, our concerns of size-dependent behavior and subsequent switch to microfluidic devices were justified.

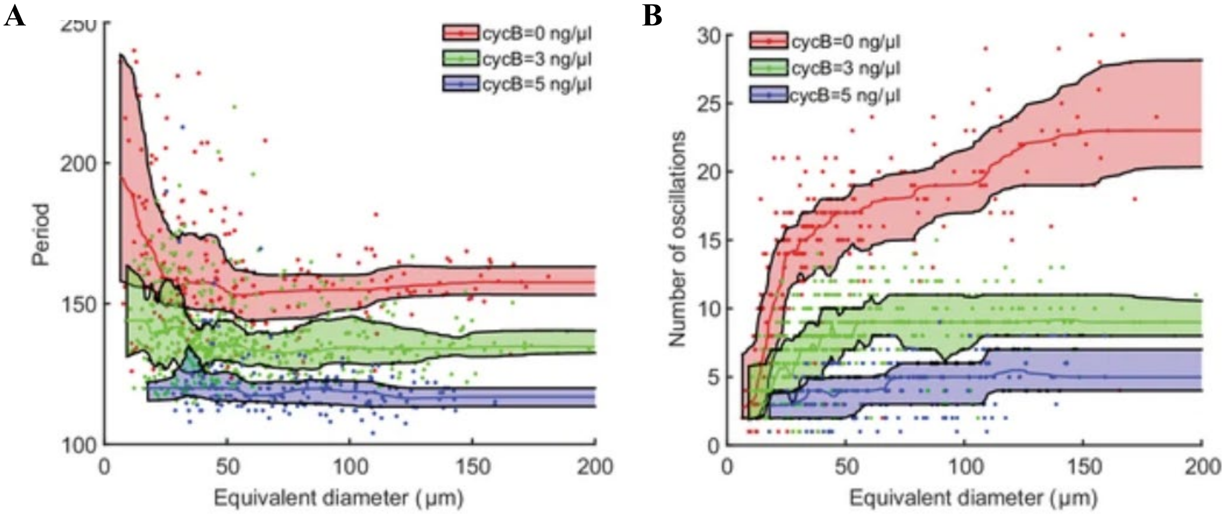

Figure 2.9. Droplets with smaller diameters have larger periods on average and a wider distribution of periods (A) and exhibit smaller number of oscillations on average (B).

Colored areas represent moving 25 percentiles to 75 percentiles and are smoothed using the LOWESS smoothing method. The equivalent diameter is defined as the diameter of a sphere that has an equal volume to that of a droplet, estimated by a volume formula in literature. Note that these size effects are smaller for droplets with higher cyclin B mRNA concentrations.

2.5.4 *In Vitro* Transcription and Translation

Protein synthesis and degradation are among the most essential reactions of a cell and can provide a fundamental source-sink basis for various complicated nonlinear dynamic processes (e.g., genetic switches, oscillations, morphogenesis, etc.). However, analyzing transcription and translation can be difficult in live cells since these processes are embedded in larger complex genetic regulatory networks that are subject to changes in intracellular and extracellular environments. Using cell-free extract, these processes can be isolated and better controlled, which directly led to the deciphering of RNA codons in the early 1960s[64]. Recent research has shown that cell-free expression system can also be used to engineer genetic circuits[65], perform fast and scalable screens to characterize gene editing systems, such as CRISPR-Cas[66], and, in combination with droplet microfluidics, produce a detailed dynamical analysis of the transcription/translation process[67,68].

To demonstrate the analytical power of our system in kinetic measurements, we reconstituted cell-free TXTL and TL systems side by side, by encapsulating wheat germ extracts supplied with plasmid DNA and mRNAs, respectively, of securin-CFP. Securin is a separase binding protein that prevents premature chromosome separation, which is critical for reliable cell cycle progression. In live cells, securin is actively synthesized in interphase and degraded upon anaphase onset, which makes it complicated to study its translation kinetics. This assay enabled high-resolution, high-throughput, real-time kinetic measurements of both TXTL and TL reactions simultaneously for more than 10 h.

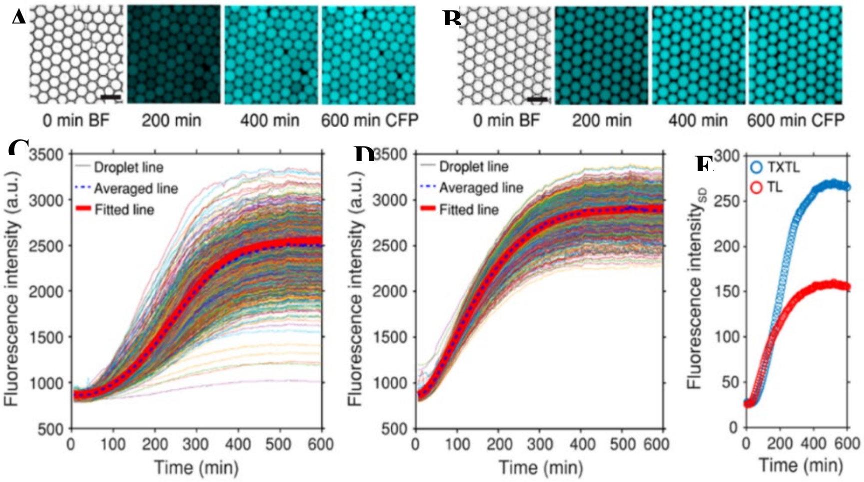

Figure 2.10. Synthesis of securin-CFP in artificial droplet cells via in vitro transcription−translation (TXTL) and translation (TL).

Selected time-lapse images showing the increasing brightness of CFP signal in droplets over a course of 600 min in both TXTL and TL assays. The fluorescence intensities of droplets at time zero are invisible, and bright-field images are shown instead. Solid colored lines showing CFP fluorescent intensities increased with protein synthesis and reached plateaus in individual droplets in TXTLassays (n= 1639) and TL assays (n= 1604), respectively. The blue dashed lines showing the medians and the thick red lines showing the model fit results. Standard deviations of the fluorescence intensities indicate the variation difference in the TXTL and TL assays. Images and data were collected every 5 min at room temperature. Scale bars: 100µm.

Interestingly, in the TXTL system, which undergoes a two-step transcription and translation process, droplets show an increasingly larger variance in intensities over time compared to the TL-alone assay, as indicated by the higher heterogeneity in brightness of droplets and the wider distribution of the curve intensity after the transcription and translation initiated. We attribute the more pronounced increasing variations of protein expression in the TXTL system to the additional transcription noise (i.e., stochastic mRNA production and degradation rates) in pL-scale encapsulations, compared to the TL system; it was found that such variation was not caused by the dispersed sizes of droplets. To further verify this hypothesis, we built a model based on previous research[6,69] to simulate the transcription and translation processes over time. By fitting each curve with our model, we found that the translation resource variation produces similar effects on both systems, while the introduction of transcriptional resource variation among droplets in the TXTL system can account for their differential variations, supporting our hypothesis.

2.6 Conclusion

In conclusion, we have developed a microfluidic platform and analytical algorithm that enables generation, incubation, and detection of arrays of individual droplets. The unique and powerful combination of analytical abilities opens up exciting possibilities for studying cell-free systems, which oftentimes require microscale analyses at high throughput, high sensitivity, and high spatiotemporal resolution. Specifically, in this chapter, we reconstructed and quantified various cellular machineries in cell-free microdroplets (i.e., cell-cycle oscillations, and nuclear morphology changes, and protein expression and degradation). Our results indicated that the droplet artificial cells enable efficient constitution and quantification of sophisticated spatiotemporal dynamics *in vitro*, manifesting its transforming potential in synthetic biology. It may eventually benefit the study of diseases and disorders at early stages of embryonic development that has been previously difficult to achieve without such a tool. In addition, the framework is easy to set up and straightforward to use, therefore, it can be adopted by any regular lab that has already been equipped with a conventional fluorescence microscope as a universal and low-cost solution to perform diversified types of droplet analysis; thus, it will ultimately be lowering the barrier of using droplet microfluidic technology for a broader range of applications, particularly in the fields of chemistry, physics, medicine, and biology.

Chapter 3 Comprehensive Parameter Space Mapping of Cell Cycle Dynamics Under Network Perturbations

Studies in quantitative systems and synthetic biology have extensively utilized models to interpret data, make predictions, and guide experimental designs. However, models often simplify complex biological systems and lack experimentally validated parameters, making their reliability in perturbed systems unclear. Based on the findings of the previous chapter, the mitotic oscillator is highly tunable, so here we used the previously described droplet-based synthetic cell system to continuously tune single-cell parameters in multiple dimensions with full dynamic ranges to provide an experimental framework for global parameter space scans. We systematically perturbed the cell-cycle oscillator, enabling comprehensive mapping of period landscapes in response to network perturbations. The data allowed us to challenge existing models and refine a new model that matches the observed response. Our analysis demonstrated that Cdk1 positive feedback inhibition restricts cell cycle frequency range, confirming model predictions; furthermore, it revealed new observations of cellular responses to the Cdk1-counteracting phosphatase PP2A inhibition, exhibiting monomodal or bimodal distributions across varying inhibition levels, underscoring the complex nature of cell cycle regulation that can be explained by our model. This global perturbation platform may be generalizable to exploring other complex dynamic systems.

3.1 Introduction

Most multicellular life starts with a series of rapid synchronous embryonic cell cycles. Unlike somatic cells that undergo four distinct cell cycle phases, early embryonic cells skip G1/G2 gap phases, checkpoint machinery, or transcriptional activity, and oscillate between the S phase and M phase until zygotic genome activation[70–72]. Nonetheless, the basic components of the oscillatory networks are shared among early embryonic and somatic cell cycles and evolutionarily conserved across almost all eukaryotic species.

In theory, a negative feedback loop alone can generate oscillations. In reality, however, cell cycle networks involve many more complicated regulatory components that form coupled positive and negative feedback loops. Researchers have constructed mathematical models, both simple and complex, to understand the role of these regulatory circuits in cell cycle behaviors observed in experiments. Novak & Tyson[16] and Thron[58] first proposed the role of the Cdk1/Cdc25/Wee1 positive feedback system as a bistable trigger for mitotic entry, which was later confirmed by experiments[24]. Novak and Tyson constructed a detailed mass action model with 10 equations[17]. Following that initial work, they then simplified it into a two-equation model based on Goldbeter-Koshland kinetics (Novak-Tyson-2equ)[73]. Yang and Ferrell also developed a two-equation model using Hill function-based rate equations. This model highlighted the important role of hypersensitive response of APC/C to Cdk1 and a sufficient time delay in the robust cell cycle oscillations, which were verified experimentally. Modeling work by Tsai and Ferrell also predicted that the interlinked positive and negative feedback promotes robust oscillation and expands the frequency range (i.e., tunability) of cell cycles[22]. Remarkably, cell cycle modeling also predicted a significant role of phosphatase(s) in cell cycle regulation, before the discovery of the importance of the protein phosphatase 2A (PP2A)[73].

Despite the fact that these models played a significant role in advancing the understanding of cell cycle regulation principles and informing experimental design, there are key challenges for all current models. First, even the simplest models may contain many unknown parameters that are challenging to estimate. Experimentally measuring parameters is labor-intensive and can yield inconsistent results across different laboratories and batches. Direct measurement from experiments is impractical for some highly abstract parameters in simplified models. Second, to reduce complex biological systems, models often have assumptions of chemical reactions that are not necessarily realistic. For instance, the three aforementioned cell-cycle models used different rate functions and simplified the Cdk1 network differently. Therefore, the effectiveness of these models in altered conditions is questionable. Lastly, additional regulatory networks of the cell cycle have been discovered in recent years and the classical models need to be modified to incorporate these new circuits. Notably, while previous models only considered positive feedback loops involving Wee1 and Cdc25, recent research suggests the need to include additional positive feedback regulation between Cdk1 and its counteracting phosphatase, especially PP2A[5,74–76]. Yet, there has not been a systematic study on how PP2A affects embryonic cell cycle dynamics.

An important step towards addressing these challenges is to systematically quantify cell cycle dynamics and map the entire oscillation landscape of the network under global parameter perturbations. Compared to measuring parameters individually, such fine-grained multi-dimensional dataset enables more reliable parameter estimation by global fitting and hence provides better constraints of models for their efficacy evaluation.

To this end, we systematically scrutinized cell cycle dynamics in droplets under perturbations of cyclin B1, Wee1, and the recently identified PP2A circuit, either individually or in combination. The cell-free extracts provide an exceptional system for such perturbation analysis, as it permits the direct incorporation of various cell-impermeable molecules such as mRNAs, proteins, and sensors. We further examined the behavior of classical cell cycle models under these combinatory perturbations and compared them with our experimental results. To incorporate the PP2A perturbation data, we constructed a cell cycle model including the PP2A circuit based on the Yang-Ferrell-2equ model and identified the parameter space that supports free-running oscillation. Modeling the experimental perturbation responses offers insights into how this newly incorporated PP2A circuit contributes to the cell cycle oscillation and its dynamical properties.

This chapter is adapted from the published article *Comprehensive Parameter Space Mapping of Cell Cycle Dynamics under Network Perturbations*[48]. My contributions to the project include experimental platform design; experiment design; performing experiments; data collection, processing, and analysis; and writing the manuscript.

3.2 Droplets Experience Gradual Phase Diffusion Over Time

We first set out to estimate the innate variations of our experimental platforms by using a single-inlet microfluidic device that generates droplets of cycling Xenopus egg extracts at a uniform size and constitution. Analysis of the temporal signal of securin-CFP oscillation revealed that initially the droplets were highly synchronized in the first few cell cycles (cycle #1 through #4), but gradually desynchronized in later cycles (starting cycle #5).

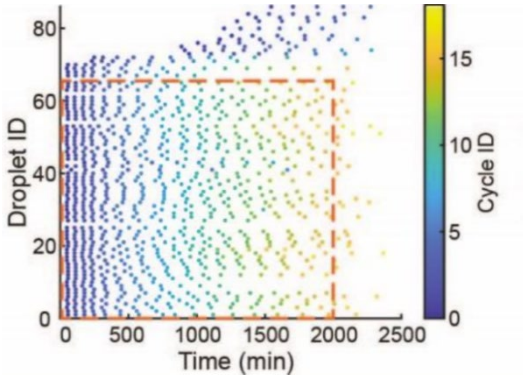

Figure 3.1. Raster plot of mitotic oscillations over time.

Each dot represents one peak in the fluorescent profile of one droplet placed at the time of the peak.

To identify the source of cell cycle desynchronization, we analyzed the variations (standard deviation, SD, and variance) of the droplet securin-CFP peak time (T_peak) of each cycle, from the first to the 15th cycle, resulting in a linear increase in the SD of T_peak over the average time of T_peak.

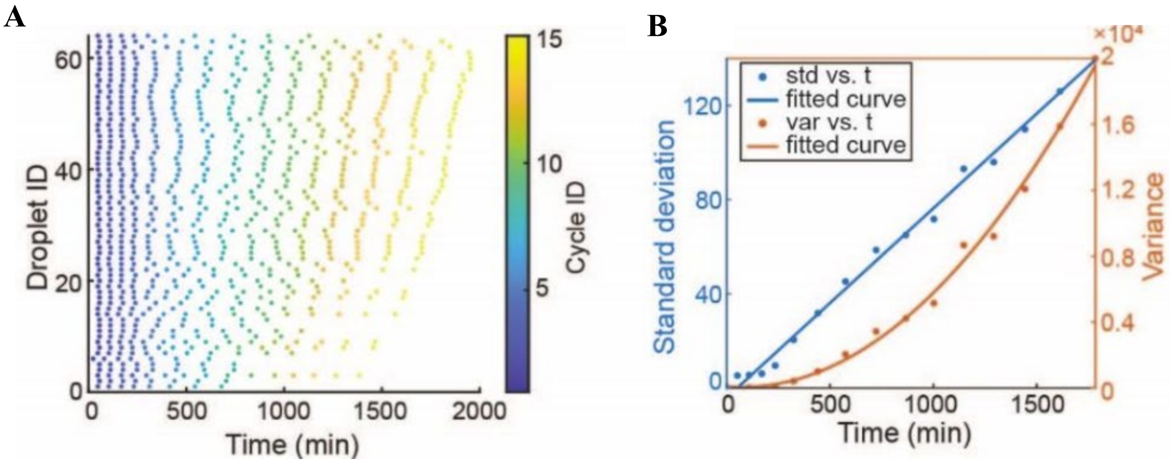

Figure 3.2. Phase diffusion of droplets with control extract.

(A) Raster plot of the same dataset. Incomplete tracks are discarded, the remaining droplets (the selected area from the left figure) are sorted by average period length and reassigned droplet IDs. All points beyond the 15th cycle are also discarded. (B) standard deviation and variance of peak times against time. Each point represents all droplets with the same cycle ID.

If random phase diffusion dominates the system noise, the peak time variance should be linearly correlated with time[27]. Instead, our results showed a concave-up curve of peak time variance over time. These results may be explained by the observation that the droplets generated from the same batch and constitution of extract had innate differences in oscillation periods, which becomes apparent when sorting all droplets by their average period. A possible cause of the droplet period difference is the partitioning noise during the microemulsion encapsulation process[63]. Together, these results suggested that the major source of system noise is not the phase fluctuation of cell cycles, but the initial period variation among the population of individual droplets that can propagate throughout cycles. Nevertheless, the droplet period noise (SD) is ~8% of the average droplet period, which is still much lower compared to the effect of the perturbations used in the study.

In addition, we found that the droplet oscillations gradually slowed down after the first three to four cycles with increasing periods. This is possibly caused by the depletion of some rate-limiting factors in the droplets, such as energy or cyclin B1 mRNA. The first three cycles maintained a roughly constant cycle period, which is likely a more accurate representation of the physiological state of droplets. Therefore, in the following analyses of this study, we only focused on the first three cycles.

3.3 Multi-Inlet Microfluidic Platform for Comprehensive Parameter Space Perturbations Shows Interphase Period Is Highly Tunable by Cyclin B Levels

The single-inlet microfluidic device could only generate droplets with identical initial states, despite small variations, as described above. To enable global exploration in parameter space, we extended our microfluidic design to incorporate up to three inlets prior to droplet formation. In this study, one of the inlets was reserved for Xenopus egg extracts, while the remaining channels were utilized to introduce recombinant mRNA molecules or chemical agonists/antagonists of cell cycle regulators for perturbation purposes. Content from the channels is mixed during droplet formation. The ratio of the content from the inlets can be dynamically adjusted by changing the pressure difference of the channels. The total flow rate from all channels is kept constant to ensure constant droplet size. In this study, the droplet size is kept at around 100 µm which is comparable to early embryonic cells.

Consequently, depending on which of the single-inlet, two-inlet, or three-inlet microfluidic devices are employed, for any single batch of extracts, our microfluidic platform can be programmed to generate droplets of uniform size and multiple pre-set constitutions, such as discrete levels of a cell cycle regulator, a continuous parametric sweep of one component, or a two-dimensional array of two components. Stable chemical fluorophores, such as Alexa 594 and Oregon Green, were used as indexing dyes for different inlets, so the composition of individual droplets can be quantified based on the fluorescent levels of these indexing dyes.

We used securin-CFP, as an anaphase substrate cell cycle reporter to monitor the cell cycle progression in all experiments of this study. To maintain a consistent concentration of the securin reporter mRNA in all droplets generated in a batch, we added the mRNA in all inlets at the same concentration. We developed an in-house image processing and droplet tracking algorithm to track and quantify the securin-CFP dynamics in individual droplets.

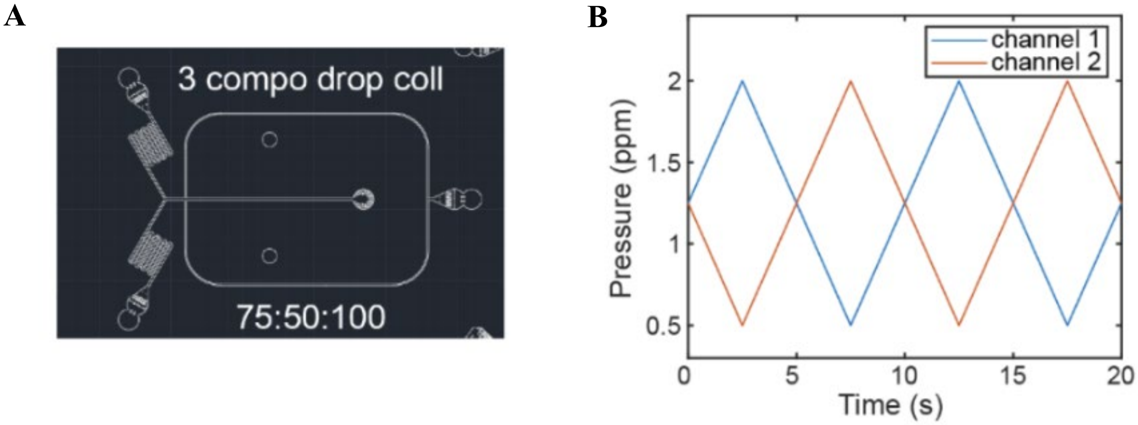

Figure 3.3. 2-channel tuning device and pressure profile.

(A) Design of 2-channel microfluidic device for droplet generation. Extracts were flown in from the 2 inlets on the left, surfactant oil was flown in from the right, droplets were collected in a well in the middle punched in after fabrication. (B) Temporal pressure profile of the 2 extract channels for continuous content tuning. The sum of total pressure is kept constant.

Varying cyclin B synthesis rate could effectively tune the cell cycle duration, as previously demonstrated in chapter 2. In our investigation, we aimed to generate an experimental dataset to measure the cell-cycle response through a single-variable parameter sweep focusing on the cyclin B synthesis rate in both directions.

To tune down cyclin B production rate in droplets, we designed and applied cyclin B morpholino antisense oligonucleotides to block the transcription of endogenous Xenopus cyclin B (x-cyclin B) mRNA species. A mixture of four morpholinos was used, two for x-cyclin B1 and two for x-cyclin B2. We used a 2-inlet microfluidic device, with one inlet injected with unmodified cycling Xenopus extract, and the other with extract containing additional morpholino mixture and an indexing dye. By varying the pressure of the two inlets following a pre-programmed profile, we generated droplets with a continuous gradient of morpholino concentration, ranging from 0 to 5 μM total morpholinos. For each droplet, the concentration of added morpholinos was calibrated by the fluorescence intensity of the indexing dye.

Morpholino addition significantly slowed endogenous oscillations with up to 5-fold increase in the cell cycle period, affirming that cyclin B level significantly affects the cell cycle period. However, not all phases of the cell cycle are equally affected. The rising phase of the securin-CFP oscillation, which comprises mainly the interphase and the initial part of the M-phase, showed a roughly linear increase in duration, whereas the falling phase, approximately corresponding to the start of anaphase until mitotic exit, maintained a relatively constant duration. The insensitivity of the falling phase period to cyclin B variation is consistent with previous reports that the mitotic phase is temporally more robust compared to other phases, which can be explained by the positive feedback loops in the mitotic circuit.

We then examined cell cycle dynamics when introducing additional recombinant human cyclin B (h-cyclin B) mRNAs to the extracts that were treated with 5 μM morpholinos to inhibit endogenous cyclin B mRNA. We used the same 2-inlet microfluidic device to generate droplets having 0 to 25 ng/μL h-cyclin B mRNAs. In the absence of h-cyclin B mRNA, the system oscillated at a speed similar to that observed when 5 μM morpholino was applied, likely driven by residual endogenous x-cyclin B mRNA. The addition of h-cyclin B mRNA significantly accelerated cell cycle oscillations with up to 4-fold increase in the cell cycle frequency.

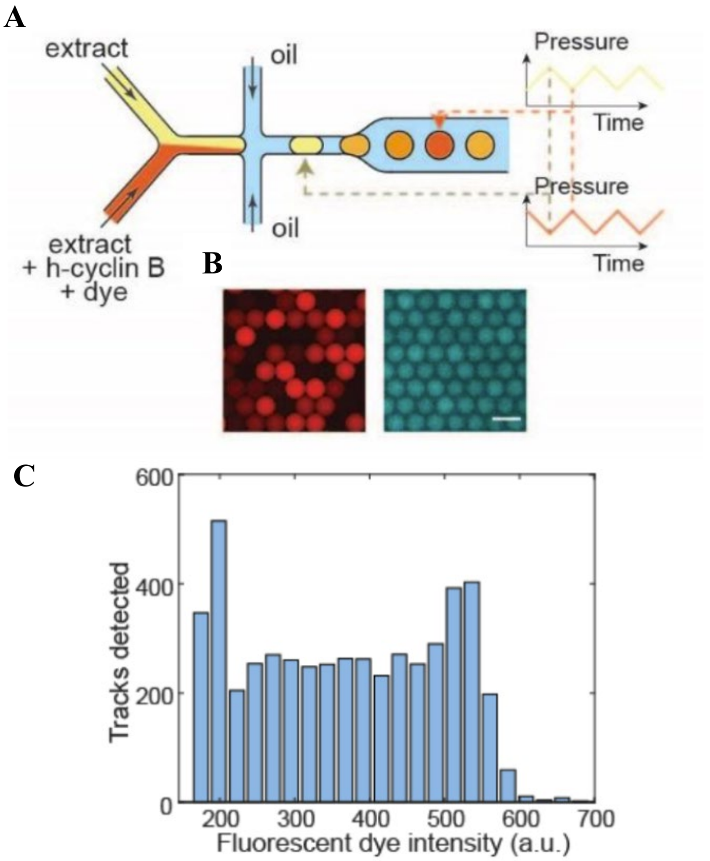

Figure 3.4. Experimental setup for 2-channel tuning microfluidic device.

(A) schematic view of a two-channel microfluidic device. Fluorescent dye is co-added with cyclin B mRNA to index concentration. (B) fluorescent images of droplets generated. Left: fluorescent dye. Right: securin-CFP. Scale bar 100 µm. (C) Histogram of fluorescent dye intensity in droplets generated by 2-channel tuning.

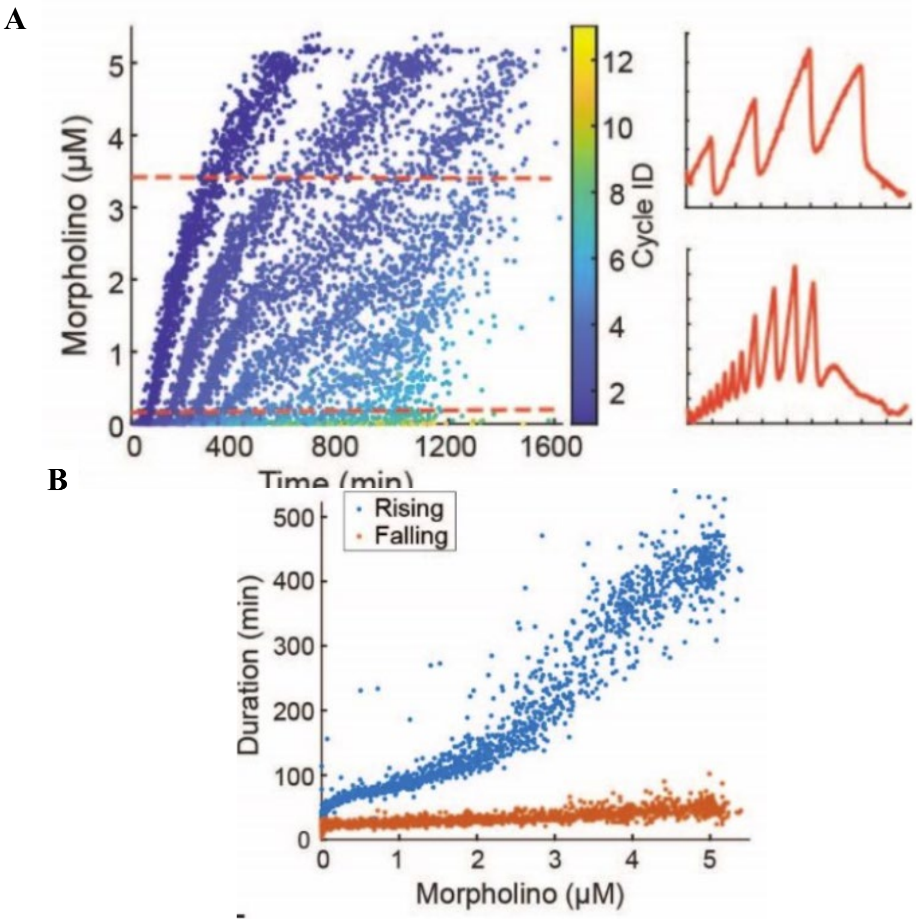

Figure 3.5. Oscillation characteristics with the tuning of Morpholino.

(A) Left: Raster plot of droplets with varying morpholino concentrations. Right: fluorescent profiles of two example droplets with different morpholino concentrations, indicated by dashed lines in the left figure. (B) Rising and falling period vs morpholino concentration. Only the first cycle periods are included in the figure for clarity.

Consistent with the impact of morpholinos, only the period of the rising phase significantly shortened with increasing cyclin B mRNA concentration, whereas the falling phase period was almost unaffected. Both the cyclin B mRNA and morpholino tuning consistently demonstrated that the cell cycle period monotonically and gradually decreases with an increasing cyclin B synthesis rate.

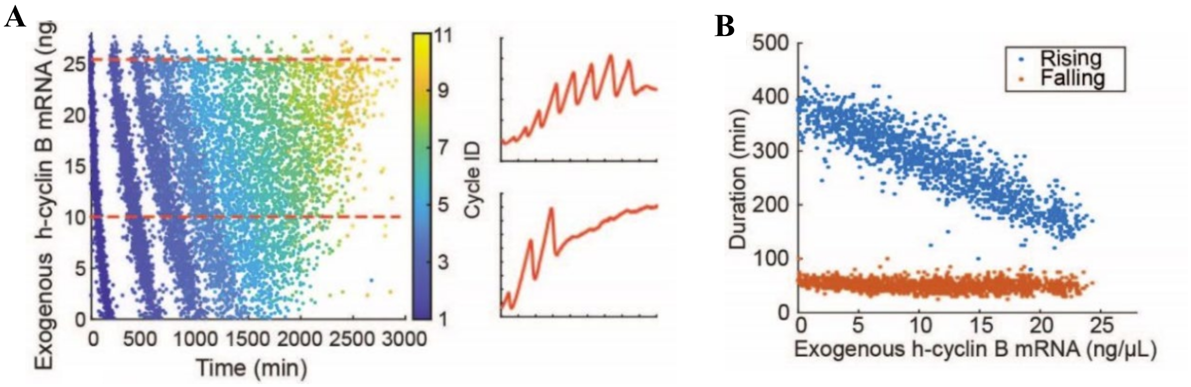

Figure 3.6. Oscillation characteristics with the tuning of cyclin B mRNA.

(A) Left: Raster plot of droplets with varying Cyclin B mRNA concentrations. Right: fluorescent profiles of two example droplets with different cyclin B mRNA concentrations, indicated by dashed lines in the left figure. (B) The rising and falling period vs cyclin B mRNA concentration. Definitions of the rising and falling phases of the fluorescent profile are indicated in Figure 2.5. Only the first cycle periods are included in the figure for clarity.

With these datasets, we could evaluate the three published cell cycle models to test if they correctly recapitulate the cell cycle response to cyclin B tuning. All three models assumed that the oscillation is driven by the negative feedback loop between cyclin B-Cdk1 and APC/C but used different rate equations. The Yang-Ferrell’s model11 and Novak-Tyson-2equ model are simple two-equation systems that use Hill function and Goldbeter-Koshland kinetics, respectively, to construct the rate equations. The third, Novak-Tyson-full model is a detailed mass action model with 10 equations. All three models correctly predicted the cell cycle responses to mRNA concentration at a relative low cyclin B synthesis rate.

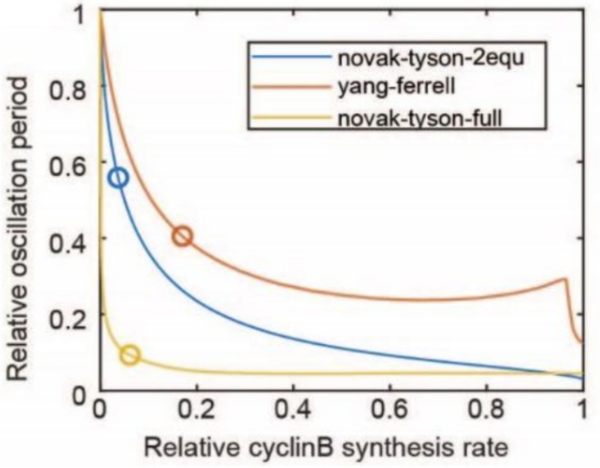

Figure 3.7. Relative period (normalized to maximum) when tuning cyclinB synthesis rate (minimum value to maximum is normalized to 0-1) in three models.

ksynth in yang-ferrell model and k1 in novak-tyson-2equ and full model are perturbed to simulate mRNA variation. Initial parameter value is circled.

However, at a high cyclin B synthesis rate, both Yang-Ferrell's two-equation model and Novak-Tyson's full model showed a slight increase in the oscillation period, which was not experimentally observed. The increase in period at high cyclin B levels in the two models resulted from the increases in the period of falling phase of cyclin B (i.e., late mitotic phase), presumably because faster synthesis rate resulted in more cyclin B proteins to be degraded at the falling phase. In contrast, Novak-Tyson's two-equation model recapitulated the monotonic and gradual decrease of cell cycle period with increasing cyclin B synthesis rate, presumably because the Michaelis–Menten kinetics derived steady state allowed a faster initial degradation of cyclin B protein. These results suggest that the dynamics of Wee1-Cdk1 and Cdc25-Cdk1 regulations under fast equilibrium assumption, used in both the two-equation models, might be better modeled by Goldbeter–Koshland kinetics.

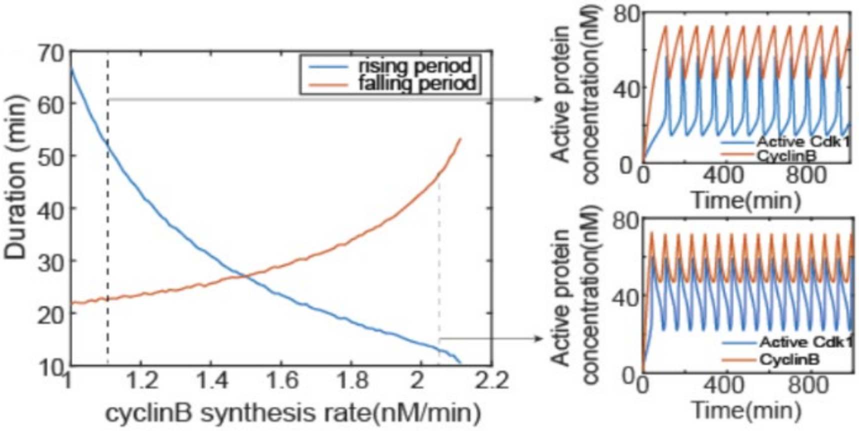

Figure 3.8. Simulated oscillations with changing cyclin B synthesis rate.

Left: Increasing and decreasing period of Qiong-Ferrell model, showing that decreasing period significantly increases at high cyclinB synthesis rate. Right: example oscillatory trace of cyclinB (red) and active Cdk1 (blue) from high cyclinB synthesis rate (lower) and low cyclinB synthesis rate (higher).

3.4 The Wee1 and Cdc25 Positive Feedback Loops Increase Cell Cycle Period Tunability

Theoretical studies have suggested that the strength of the Cdk1/Cdc25/Wee1 positive feedback is essential for the period tunability by cyclin B[22]. To examine such relations, we applied a 3-inlet microfluidic platform to simultaneously vary the positive feedback strength and the cell cycle speed by changing the cyclin B synthesis rate. This systematic mapping of the cell cycle period landscape can inform how the period tunability responds to fine-tuning of the feedback strength.

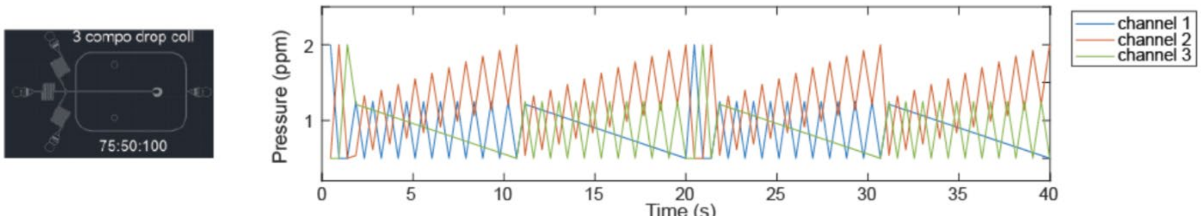

Figure 3.9. 3-channel tuning device and pressure profile.

Left: Design of 3-channel microfluidic device for droplet generation. Extracts were flown in from the 3 inlets on the left, surfactant oil was flown in from the right, droplets were collected in a well in the middle punched in after fabrication. Right: Temporal pressure profile of the 3 extract channels for continuous content tuning. The sum of total pressure is kept constant. The cycles are designed so the parameter space is evenly scanned.

To suppress the positive feedback strength, we compromised the kinase activity of Wee1 with a chemical tyrosine kinase inhibitor PD16628525[77]. Note that applying a Wee1 inhibitor also inevitably suppresses the Cdc25 positive feedback loop, because Wee1 and Cdc25 antagonistically regulate the same phosphate groups of Tyr15 and Thr14 on Cdk1.

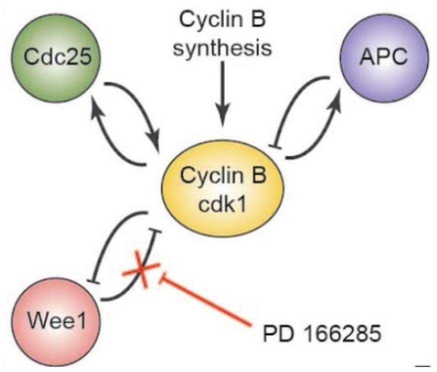

Figure 3.10. Schematic view of the function of PD166285 on the mitotic circuit.

We first applied different concentrations of PD166285 and performed 2-channel cyclin B mRNA tuning to test if the cell cycle period tunability is affected. The results revealed that while droplets with no PD166285 showed a wide range of oscillation frequencies, this range was dramatically reduced when 2 µM or more of inhibitor was present (Figure 3C, Figure S2D). In the group with the highest inhibitor concentration (10 µM), the period change was on the same level as background noise. This suggested that interrupting Cdc25/Wee1-based positive feedback could impose a significant impact on the cell cycle tunability, even though the cell cycle oscillations were sustained.

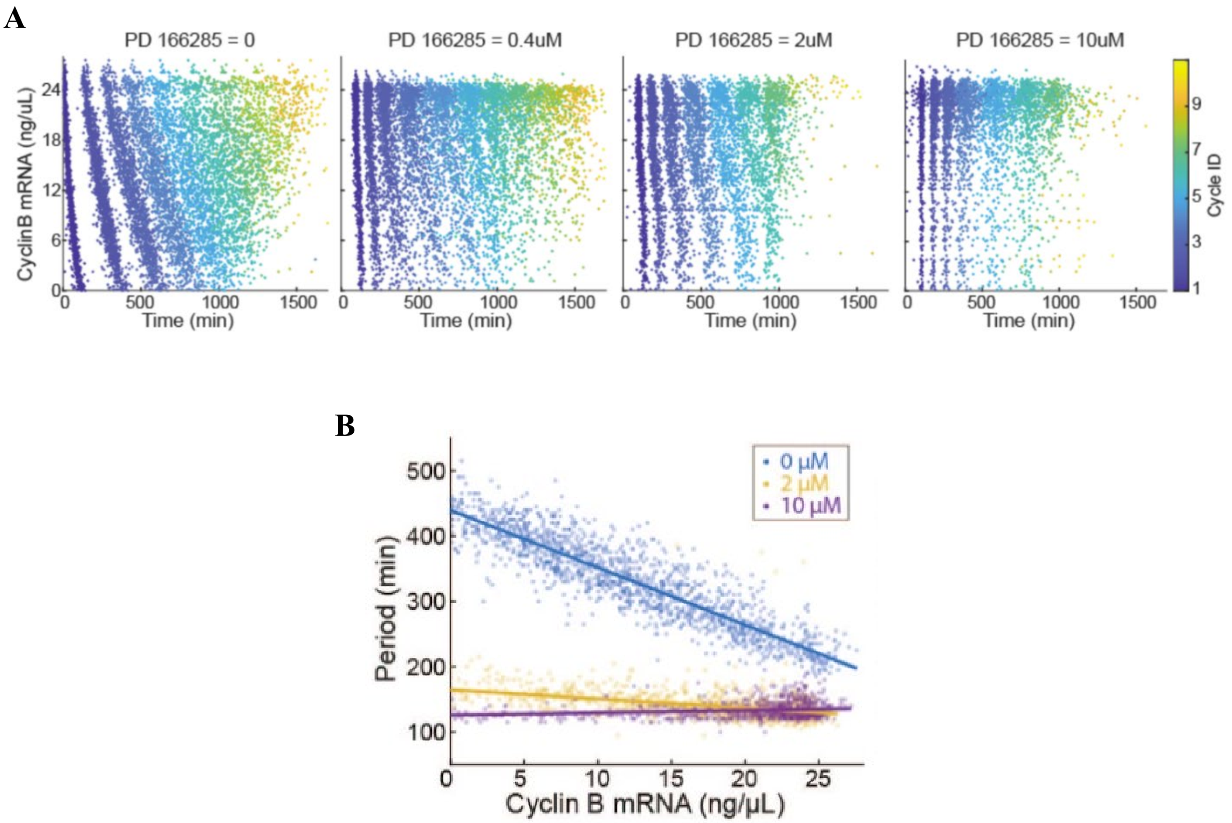

Figure 3.11. Oscillation characteristics with the addition of discrete levels of Wee1 inhibition.

(A) Raster plot of mitotic oscillations of droplets with different cyclin B mRNA concentrations at 4 separate PD 166285 concentrations (0, 0.4, 2, 10µM). Color bar indicates cycle ID. (B) Period tuning by cyclin B mRNA under coarse-grained Wee1 perturbations. The colored scatter plots represent 3 distinct PD166285 concentrations. The lines indicate linear approximations of the experimental data.

We then used the 3-inlet setup to generate a fine-grained tuning of both cyclin B (by adding 0 to 6 ng/mL h-cyclin B mRNA to extracts supplied with 5 µM x-cyclin B morpholinos) and Wee1 (by 0 to 2 μM PD166285). We programmed a 3-inlet pressure profile, so that the generated droplets have relatively uniform distributions of PD166285 and cyclin B mRNA concentrations. The results showed that increases in PD166285 concentration gradually reduced the range of droplet cell cycle periods under the same tuning range of cyclin B mRNA concentration, and the difference is more evident in the lower cyclin B mRNA concentration region.

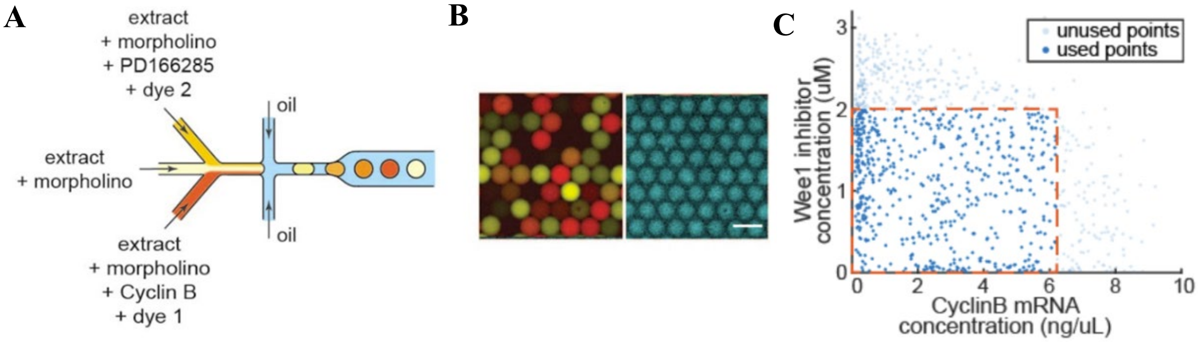

Figure 3.12. 3-channel tuning experiment setup.

(A) schematic view of a three-channel microfluidic device. Fluorescent dyes are co-added with cyclin B mRNA and PD166285 respectively to index their concentrations. (B) fluorescent images of droplets: composite of fluorescent dyes (left) and securin-CFP (right). Scale bar 100 μm. (C) The resulting concentration of Cyclin B mRNA and PD 166285 in droplets generated by 3-channel tuning. Only data points in the selected area were used for further analyses.

To examine if computational models could recapitulate the observed results, we then perturbed parameters representing Wee1 activity in the aforementioned three models. We first examined the model responses to Wee1 without cyclin B tuning. When decreasing Wee1 activities to 20-30%, all models showed an oscillation arrest, which was not observed experimentally at 10 μM PD166285. This suggests that these three models were incomplete, and other components may be required to properly explain the cell cycle dynamics when Wee1 is inhibited.

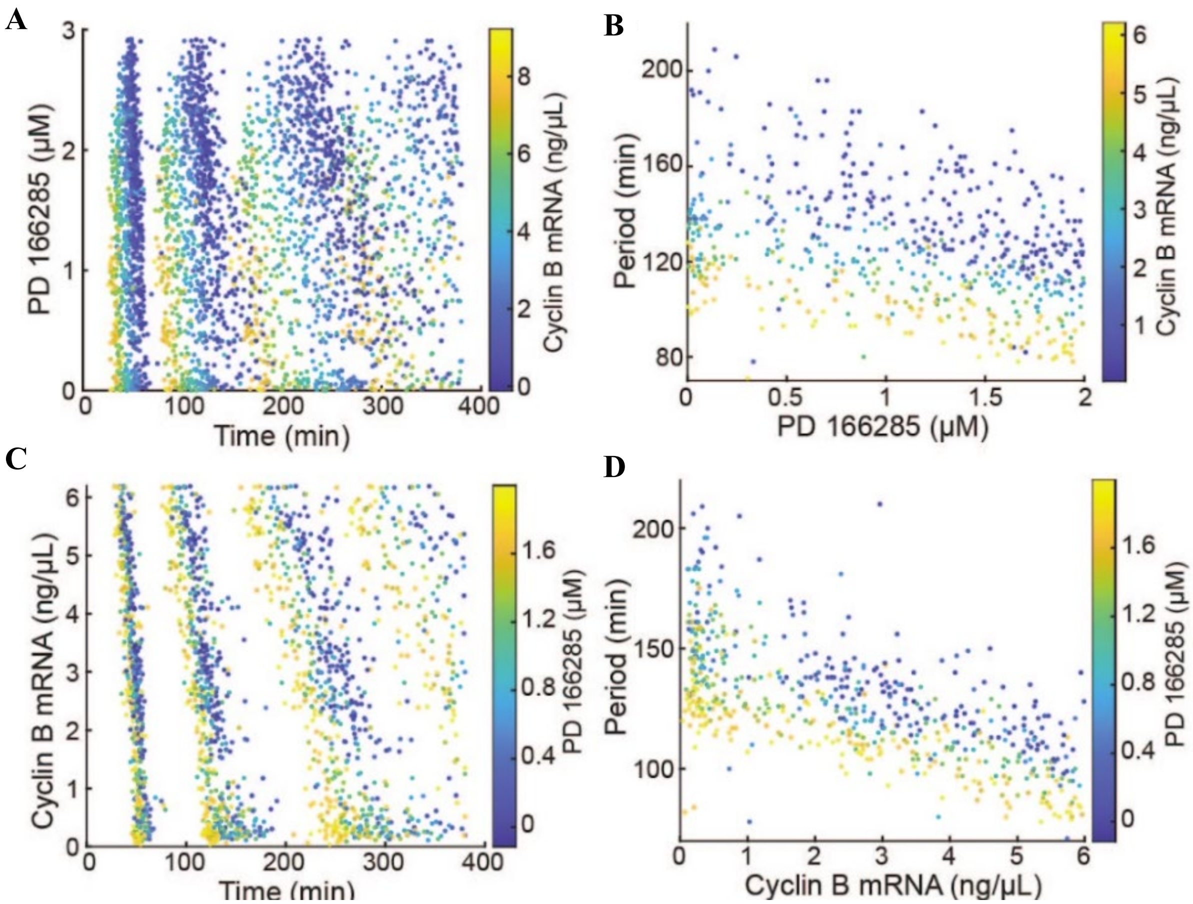

Figure 3.13. Raster plot of cyclinB and Wee1 3-channel tuning.

(A) Raster plot of droplets with varying cyclin B mRNA concentrations. (B) Scatter of oscillation period vs cyclin B mRNA concentration. Only the first cycle periods are shown in the figure to eliminate the period elongation effect. (C) Raster plot of droplets with varying PD166285 concentrations. (D) Scatter of oscillation period vs PD166285 concentration. Only the first cycle periods are shown in the figure.

We next examined model responses to Wee1 under cyclin B tuning to test how Wee1 activity and its associated positive feedback loops affect cell cycle period tunability. We simulated each of the three models and calculated the period range as we tuned both cyclin B synthesis rate and Wee1 activity respectively.

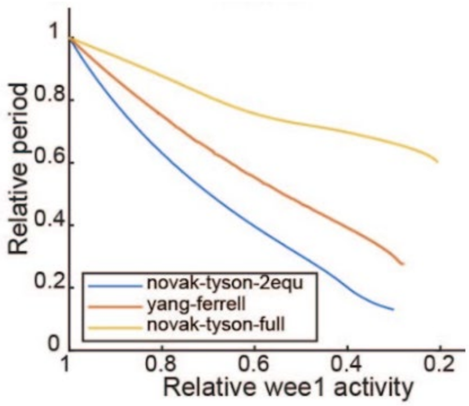

Figure 3.14. Relative period (normalized to maximum) when decreasing Wee1 activity in three different models.

Decreasing of bWee1 in yang-ferrell model, kWee1 in novak-tyson-2equ and kWee1 in novak-tyson-full model is used to simulate the Wee1 inhibitor effect.

All three models captured the overall trend and range of cycle periods in response to changes in both Wee1 activity and cyclin B mRNA levels. In general, Novak-Tyson-2equ model seems to best describe the experimental behavior; Yang-Ferrell model showed unexpected frequency tunability increases in high mRNA and high Wee1 domains, while Novak-Tyson-full model showed smaller tunability decrease compared with experimental results. These results indicate that the existing models could predict local response to changes in Wee1 activity and cyclin B mRNA levels but failed to recapitulate experimental results in high Wee1 inhibitor concentrations, suggesting the possible contribution of other mechanisms in addition to the Cdk1/Cdc25/Wee1 positive feedback.

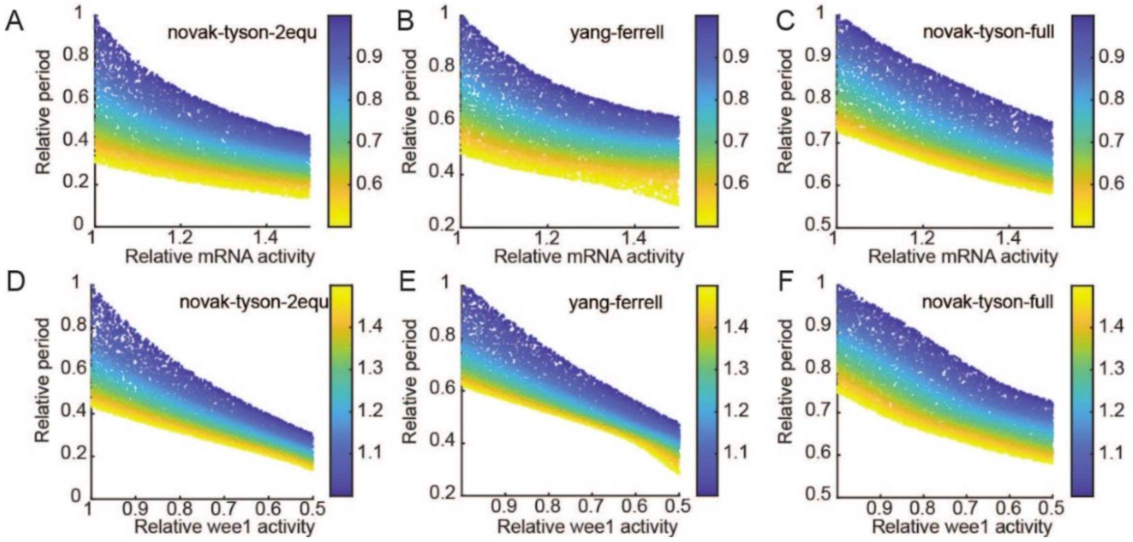

Figure 3.15. Computational simulation of cell cycle frequency change by perturbing cyclinB or Wee1 activity.

Top: Period response of relative cyclinB mRNA activity in yang-ferrell model, novak-tyson-2equ and novak-tyson-full model respectively, color code Wee1 activity. Bottom: Period response of Wee1 activity inhibition in yang-ferrell model, novak-tyson-2equ and novak-tyson-full model respectively, color code mRNA concentration.

3.5 PP2A Is Required for Cell Cycle Oscillation

Other than the extensively characterized Cdk1/Cdc25/Wee1 positive feedback, studies have identified additional positive feedback regulation centered on the Cdk1-counteracting phosphatase, PP2A[75]. PP2A dephosphorylates many Cdk1 substrates, including Wee1, APC/C and Cdc25[78]. In addition, PP2A forms a double negative feedback loop with the Endosulfine Alpha/Greatwall (ENSA/Gwl) pathway. Recent studies[5,76] reported that the PP2A-ENSA/Gwl feedback loop is necessary for the bistability of Cdk1 substrate phosphorylation. However, it is unclear whether and how PP2A affects the cell cycle dynamics.

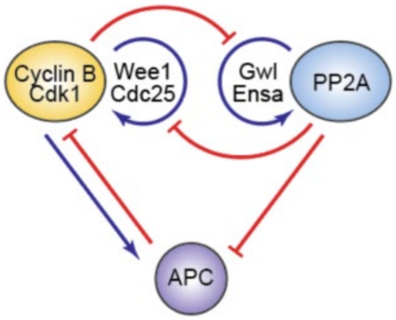

Figure 3.16. Schematic view of molecular circuits including PP2A activities.

To study the influence of PP2A on the cell cycle, we applied okadaic acid (OA), a PP2A inhibitor with a reported IC50 of 0.14nM *in vitro*[79], to tune PP2A activity in our droplet cells. Using two-channel tuning, we generated droplets of OA concentration ranging from 0 to 600 nM. We observed that PP2A inhibition by OA had a significant impact on cell cycle dynamics, and droplets treated with >500 nM OA had always shown a complete cell cycle arrest. These results supported that, unlike Wee1, which could be fully inhibited without terminating cell cycles, PP2A activity is necessary for mitotic oscillation.

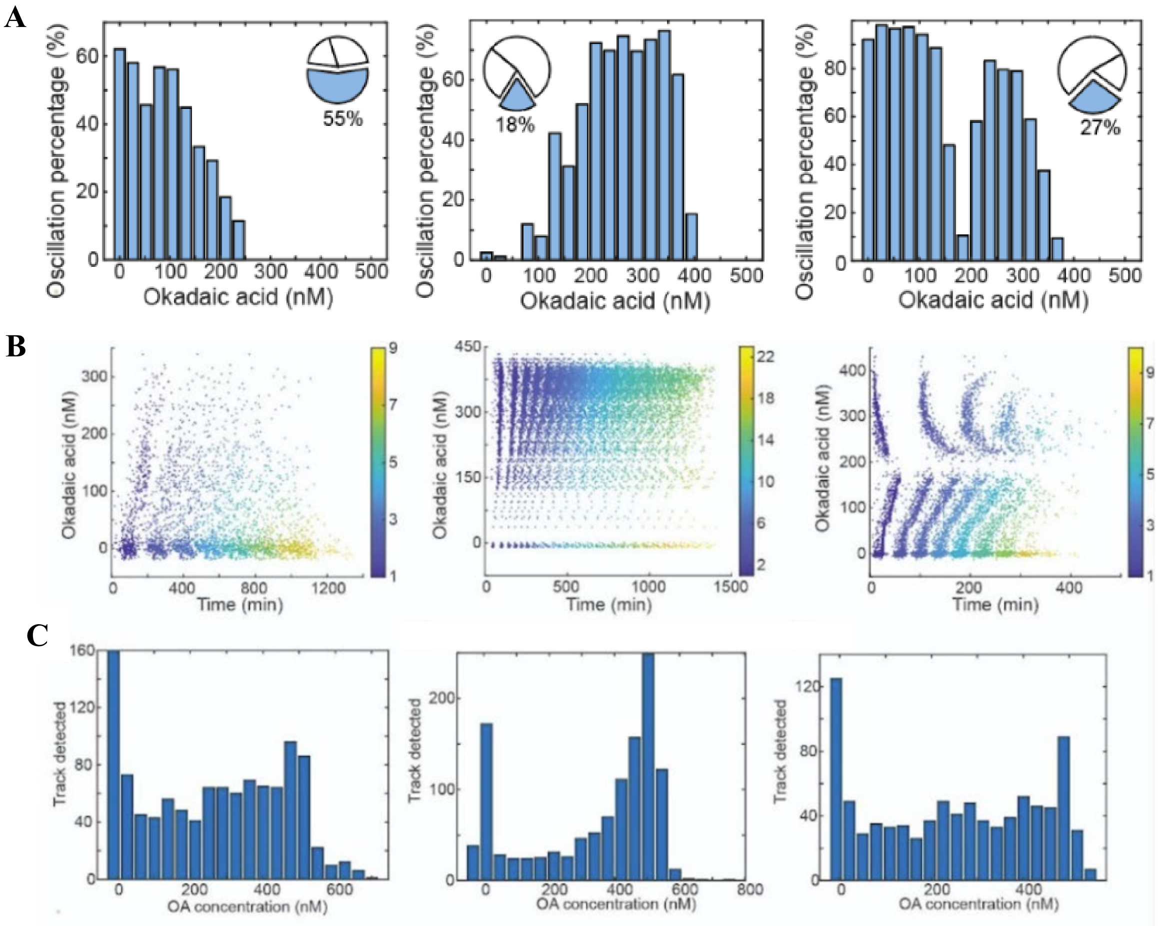

Figure 3.17. Multimodal response in oscillation behavior in response to PP2A inhibition.

(A) Percentage of oscillatory droplets vs OA concentration, showing 3 types of responses. The pie chart shows the percentage of each type in all experiment results. (B) Representative raster plot of 3 types of OA response. Droplets are sorted by OA concentration, and the color codes the peak index. (C) Histogram of tracked droplets corresponding to 3 types of OA responses.

3.6 Cell Cycle Dynamics Exhibits Multimodal Responses to PP2A Inhibition

Furthermore, we observed that cells responded to OA inhibition in distinct patterns that appeared to be batch dependent. Across 11 independent experiments with identical setup, we observed three distinct types of response patterns. The first type, observed in over half (6 times) of the experiments, was characterized by a gradual decrease in the percent of oscillating droplets as OA concentration increased from 0 to 300 nM, and a complete cell cycle arrest at higher OA levels. The second type, which was less frequent (appeared 3 times), showed a similar response as in type 1 in the lower OA region, but at higher OA, droplets “resumed” robust oscillation. In other words, type 2 response was characterized by a gap at an intermediate OA level where the cell cycle was arrested. For the third, the least frequent type (appeared twice), only a small percent of droplets had oscillations at low OA, but as OA increased, droplets showed an increasing tendency to oscillate before the percent of oscillating droplets dropped again as OA reached 400 nM. Therefore, the type 3 response resembled the trend seen in the second half of type 2 response (after the gap).

We next examined the effects of PP2A inhibition on the cell cycle period and also observed responses of multiple forms. Because of the small number of occasions of type 2 and type 3 responses, we focused on period analysis for type 1 only. The cell cycle period showed either a monotonic decrease, a monotonic increase, or a slight decrease followed by an increase. We then separately examined the durations of the increasing phase (i.e interphase and early mitotic phase) and decreasing phase (corresponding to late mitotic phase after the anaphase substrates, cyclin B or securin proteins, started to decay). This revealed that the multimodal responses in the cell cycle period mainly reflected the multimodal changes in the increasing phase. In contrast, the duration of the decreasing phase remained a simple increasing trend in all tested conditions, although the slope of the increases varied.

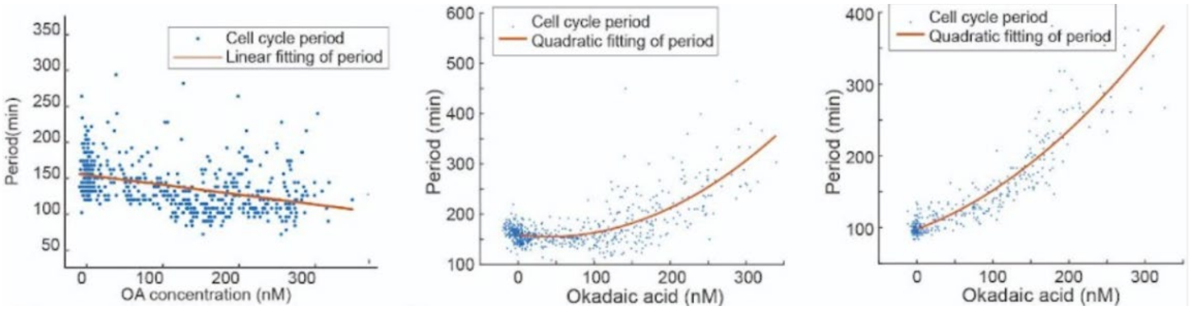

Figure 3.18. Oscillation period changes when tuning OA.

Showing three different responses: monotonic decreasing (left), decreasing and then increasing (middle), and monotonic increasing (right). Red lines are fitted curves with linear (left) or quadratic models (middle & right).

These different responses were not caused by technical errors such as uneven sampling of OA concentrations in the droplets, as checked by sampling histograms. To further confirm the observations were independent of channel-tuning setup, especially to verify the rare type 2 bimodal distribution that was never reported before in literature, we performed alternative experiments using coarse-grained manual tuning. We divided the same batch of extract into separate tubes each treated with OA at a final concentration of 0, 50, 100, 200, 400, and 800 nM. We then used single-inlet microfluidics to create identical droplets for each OA group. One of the experiments clearly recapitulated the type 2 response: oscillations were self-sustained at 0, 50, and 400 nM, but arrested at 100, 200, and 800 nM. These experiments ruled out potential technical artifacts associated with the multi-inlet sampling, suggesting that the multimodal phenomena observed could reflect biological heterogeneity of the system.

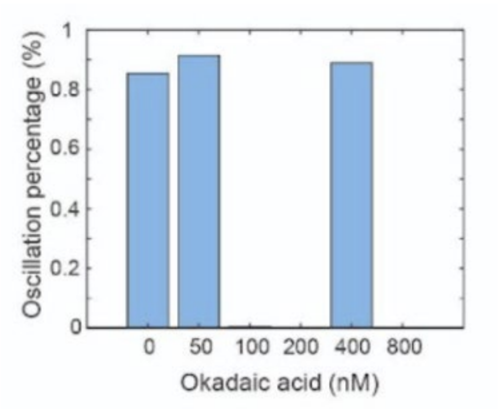

Figure 3.19. Percentage of droplets that show oscillatory behavior when adding different concentrations of OA.

Note that no oscillation is detected in 200 nM or 800 nM conditions.

Okadaic acid (OA) as a widely used phosphatase inhibitor is highly selective for PP2A over other protein phosphatases. However, when applied in high concentrations, the possibility that okadaic acid can inhibit other phosphatases including PP1 and PP4 cannot be ruled out. Therefore, we also checked to rule out any drug-specific artifacts, e.g., off-target effects of OA. We performed additional control experiments by testing multiple control inhibitors alongside with OA, including two that are more selective for PP2A: fostriecin (IC50 values for PP2A, PP4, and PP1 are 3.2 nM, 3 nM, and 40 μM, respectively) and endothall (IC50 values for PP2A and PP1 are 90 nM and 5 μM, respectively), and two versions of the PP1 inhibitor: IPP2-His and IPP2-GST (Inhibitor-2 with His-tagged and GST-tagged, respectively). Comparisons of the responses to different inhibitors are made exclusively between tests carried out on the same extracts on the same day to eliminate the impact of batch variances. Multiple iterations of the same experiment are done to ensure the results are repeatable and the effect of the inhibitors are consistent when the extracts exhibit different types of response to OA.

When applied to the same batches of extracts as OA, endothall and fostriecin both showed similar effects to OA. In contrast, Inhibitor-2, both IPP2-His and IPP2-GST, led to drastically different cell cycle behaviors from OA and endothall, such as oscillation percentage, raster plot and cycle period. Furthermore, we also observed polymorphism for different batches of extracts in response to PP2A inhibition. These polymorphic responses are likely not an artifact of OA, as they are also observed in droplets treated with fostriecin and endothall which exhibit consistent results with the OA-treated droplets of the same batches of extracts. Together, these results suggest that the OA concentrations used in our studies are likely within the range that specifically targets PP2A without disrupting other protein phosphatases. We found that these alternative PP2A inhibitors showed a similar response as OA whereas PP1 inhibitors had different effects on the droplet mitotic cycle. Moreover, droplets prepared from the same Xenopus extract batch but treated with different PP2A inhibitors showed the same type of responses. These results suggested that the multimodal responses were specific to PP2A inhibition and were extract batch dependent.

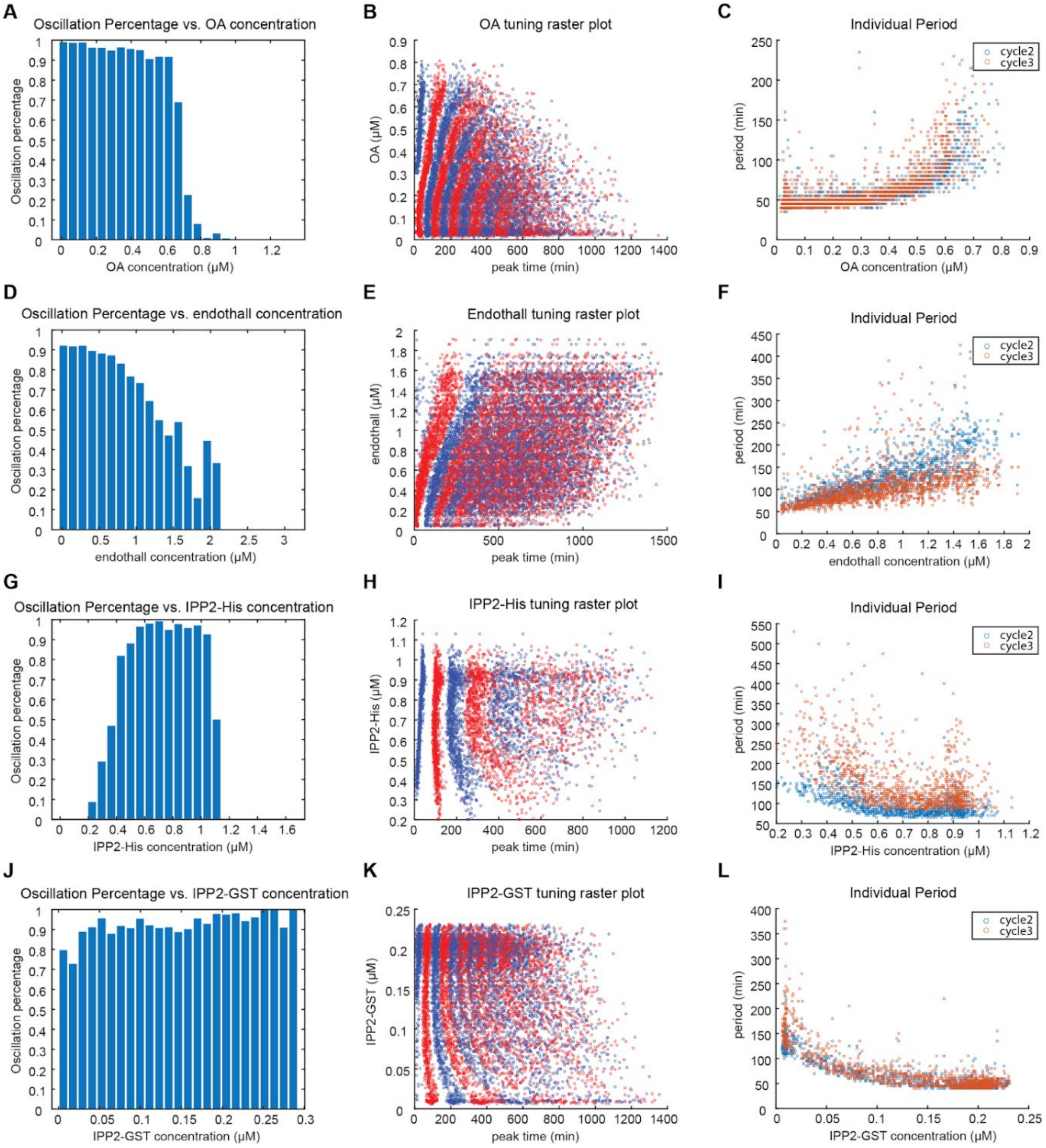

Figure 3.20. Cell cycle responses to endothall (A)-(C), okadaic acid (D)-(F), IPP2-His (G)-(I), IPP2-GST (J)-(L).

(A)(D)(G)(L) percentage of oscillatory droplets vs endothall or okadaic acid concentration. (B)(E)(H)(K) raster plot of droplets with varying concentration of endothall or okadaic acid concentration. Each point is a detected peak of an individual droplet. (C)(F)(I)(L), cell cycle period vs endothall or okadaic acid concentration.

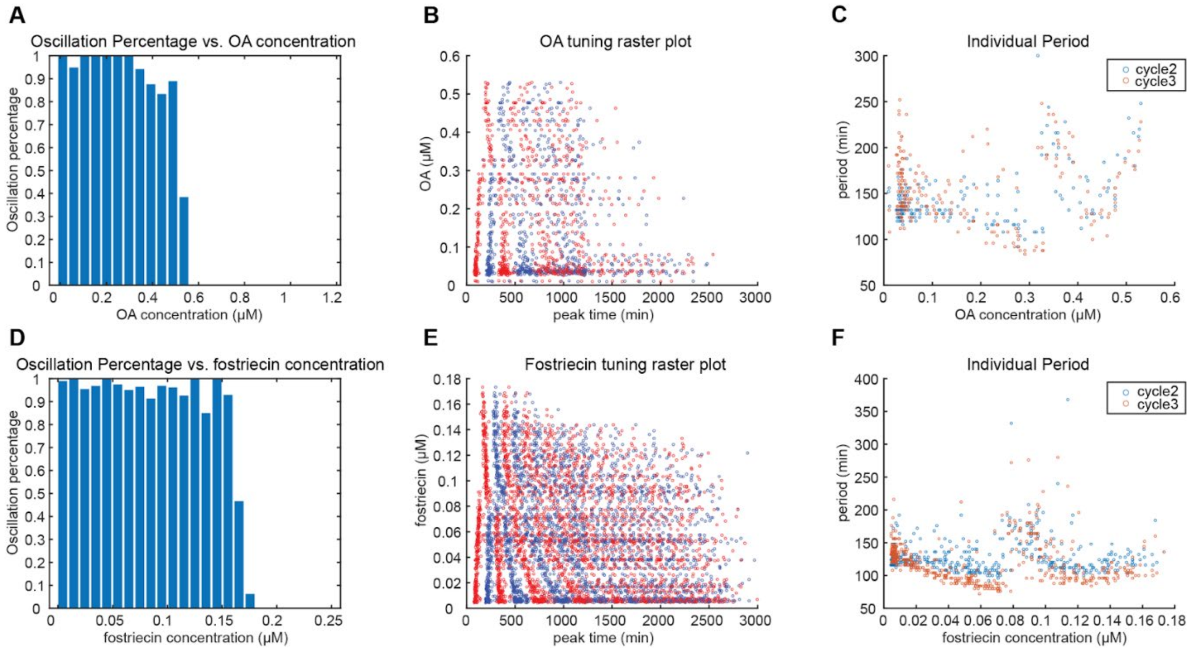

Figure 3.21. Cell cycle responses to fostriecin (A)-(C) and okadaic acid (D)-(F).

(A)(D) percentage of oscillatory droplets vs fostriecin or okadaic acid concentration. (B)(E), raster plot of droplets with varying concentration of fostriecin or okadaic acid concentration. Each point is a detected peak of an individual droplet. (C)(F) cell cycle period vs fostriecin or okadaic acid concentration.

Altogether, these results suggest that PP2A activity can significantly affect cell cycle dynamics. At high inhibitor concentration when PP2A is mostly inhibited, the cell cycle is fully arrested. However, partial inhibition of PP2A may pose different effects to the cell cycle oscillator. The fact that the droplet response depends on the batches of extracts but not the types of PP2A inhibitors strongly suggests that the distinct response patterns arise from variations in the properties of the Xenopus extract batches. Possible sources of such variations include biological heterogeneity in frogs and the maternally deposited materials in batches of Xenopus eggs as well as uncontrollable day-to-day variability in extract preparation processes. Modeling could help understand the underlying circuit design that makes the system’s response to PP2A sensitive to these variations.

3.7 Modeling Suggests Greatwall Variations Can Result in the Multimodal Responses of Cell Cycle Dynamics to PP2A Inhibition

To understand why partial inhibition of PP2A resulted in qualitatively different responses, we applied mathematical modeling and computational simulation. Because there has not been a well-recognized model that describe embryonic cell cycle oscillation of Xenopus extract that considers PP2A/Gwl/Ensa, and the existing model we tested could not recapitulate experimental perturbation in our system, we developed a new model based on the Yang-Ferrell model and the PP2A-Cdk1 interactions proposed in Kamenz et al. This simple model contains four variables (including concentrations of activated Cdk1, cyclin B, free PP2A, and phosphorylated Ensa) and 26 parameters. We hypothesized that batch-to-batch variations in the concentration of certain molecules and/or their chemical properties in the Xenopus extract resulted in differential response of the mitotic oscillator to PP2A partial inhibition. Therefore, we applied random sampling in the 22-dimension space of model parameters that reflect extract properties, excluding 4 parameters representing Hill coefficients that are unlikely to vary in different extract batches. We therefore searched for the parameter that has the highest association to causing multimodal responses with increasing PP2A inhibitor level (modeled as an additional parameter Kinh).

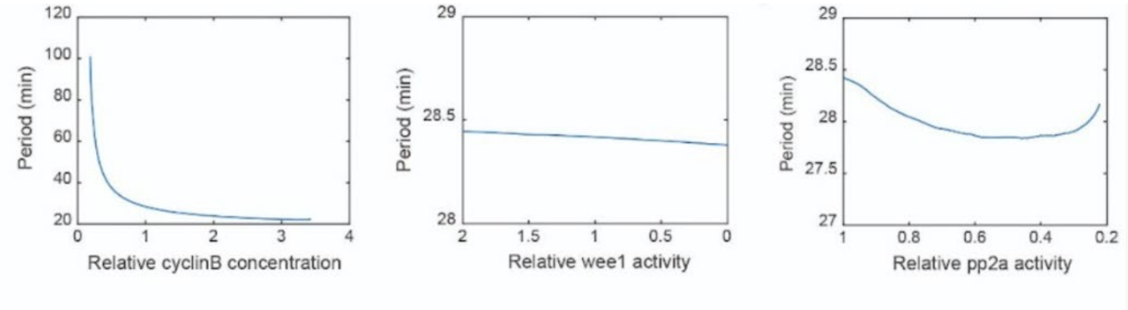

Figure 3.22. period response in Zhang-Novak model when tuning cyclinB (left), Wee1 (middle) and PP2A (right).

To reduce the computational load, we first searched ~50,000 random parameter sets for model perturbations that can result in the characteristic type 2 response, which involves a gap of cell cycle oscillation at intermediate concentration of PP2A inhibitor, oscillations at both lower and higher PP2A inhibition, and a full oscillation arrest at high PP2A inhibition, namely an oscillate-arrest-oscillate-arrest behavior. This revealed a rare fraction (15 points, ~0.3%) of the conditions with an oscillate-arrest-oscillate-arrest behavior over increasing concentration of PP2A inhibitor.

Next, we examined these conditions and the distribution for each of the 22 perturbed parameters. Interestingly, although most parameters followed a relatively uniform distribution covering a wide sample range, one parameter, Kgwl (EC50 of Cdk1 phosphorylating Gwl), showed a narrowed distribution. This suggested that a type 2 response requires a specific value range of the Kgwl. Consequently, we tested if changing Kgwl would result in type 1 and 3 responses of the model, while maintaining other parameters at the centroid of the previously identified points that support type 2 responses. Indeed, we found that higher Kgwl resulted in type 1 whereas lower Kgwl resulted in a type 3 response. This finding suggested that the frog extract variations in Greatwall could explain the puzzling multimodal responses of cell cycle oscillation to PP2A inhibition. In support of the model prediction, Kamenz et al. measured Kgwl, and found about an approximately two-fold variation in its level among three replicate experiments.

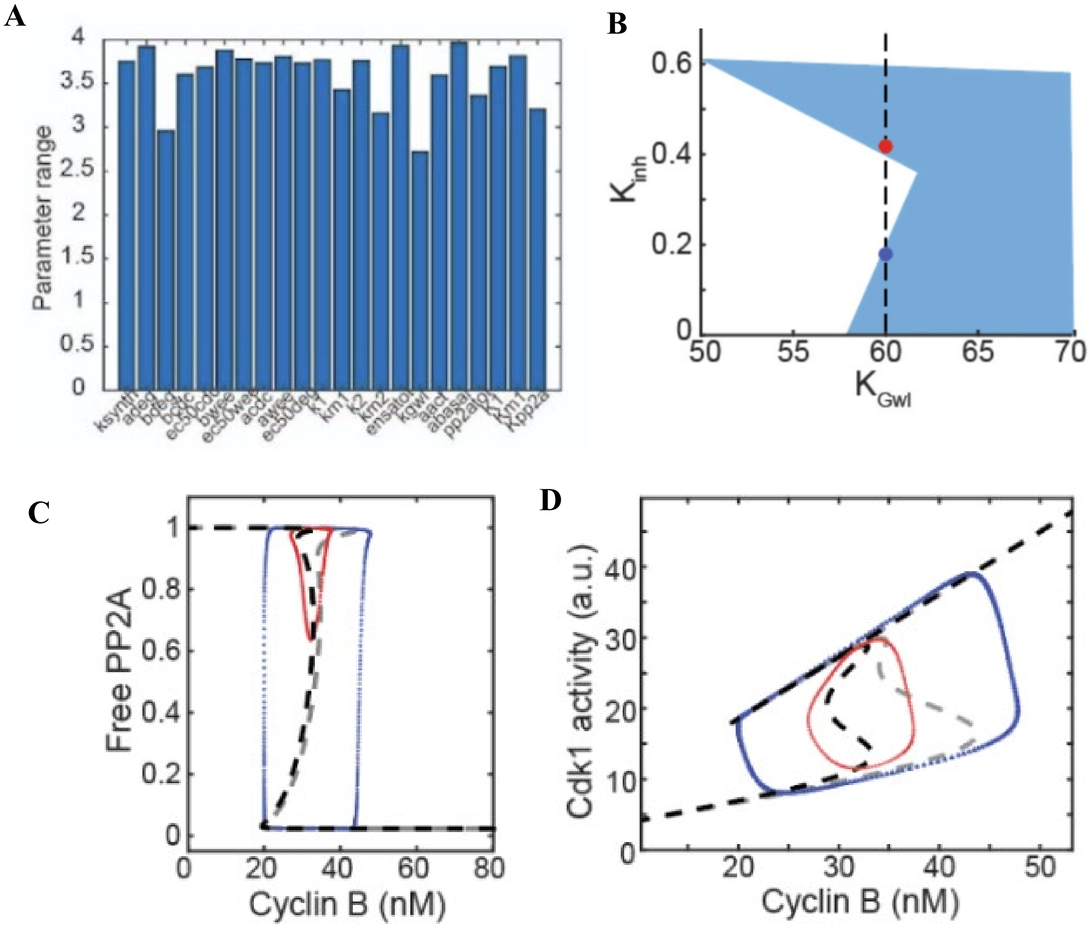

Figure 3.23. Simulation results of the bistability of Cdk1 and PP2A.

(A) Parameter range of selected oscillators that perform type2 oscillation in logarithm space. (B) Parameter regions that support oscillation when changing KGwl and Kinh (OA). Changing Kinh at a specific value of KGwl (along the dotted black line) may lead to type 3 OA response. Blue and red dots show oscillations in low and high OA concentration respectively. (C)(D) Dashed lines show response curves of steady-state free PP2A (C) or Cdk1 (D) activity when changing Cyclin B concentration under low (gray) or high OA (black). Dotted lines show phase plots of limit cycles with low (blue) or high (red) OA.

To understand how changes in Kgwl lead to different responses in the oscillator, we plotted the steady state response curves of free PP2A and active Cdk1 to cyclin B. This revealed that our cell cycle model can switch between two different stable limit cycles under partial PP2A inhibition. Previous work has shown that the activation of Cdk1 by cyclin B is bistable8, and the inactivation of PP2A by Cdk1 is also bistable. Combining both circuits, our new model gave rise to tri-stability of Cdk1 activity and free PP2A with cyclin B, which resulted in two different limit cycles. Consistent with our model-detected tri-stability, the existence of a third intermediate steady-state that arrests the cell cycle between the interphase and M phase has been predicted and experimentally verified in a previous study in mammalian cells15. When the OA level is low, the cell cycle oscillates between high and low steady states of PP2A, resulting in a high-amplitude cycle. Both Cdk1 bistability and PP2A bistability are involved during oscillations. Cell cycles from the type 1 response and the type 2 first-half response (before the gap) belong to this type of oscillation. When the OA level is high, Wee1 and Cdc25 are hyperphosphorylated, causing easier Cdk1 activation. As a result, the peak Cdk1 activity is lower and could not fully inhibit PP2A to trigger PP2A-ENSA-Gwl bistability. The oscillation occurs between the intermediate and high steady states of PP2A. In this case, the oscillation is solely driven by the bistability based on Wee1/Cdc25 positive feedback. Cell cycles from the type 3 response and the type 2 second-half response (after the gap) belong to this type of oscillation.

3.8 Modeling Suggests APC/C Variations Can Result in Multimodal Responses in Cell Cycle Period to PP2A Partial Inhibition

Although variations in Gwl might account for polymodal patterns in cell cycle oscillations, it did not explain the variations in cell cycle period response when tuning PP2A, implying the potential involvement of other molecules. Because the negative feedback core of an oscillator (i.e., the Cdk1-APC/C negative feedback loop in the cell cycle) could significantly affect the oscillator period, we hypothesized that variations in relative APC/C activity (Kdeg) could result in the variations in the cell cycle period response observed for type 1 responses. Using the same model, we varied Kdeg and examined the changes in period while varying PP2A inhibition (Kinh). As hypothesized, we found that small variations in Kdeg can result in the different period responses. Specifically, the oscillating period monotonically decreased over Kinh at high Kdeg, monotonically increased at low Kdeg, and showed a decrease-then-increase trend at intermediate Kdeg.

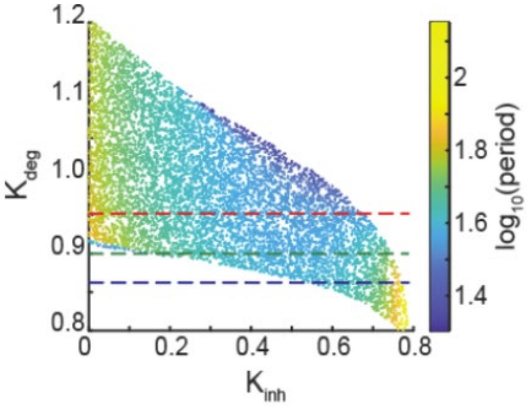

Figure 3.24. Oscillation period (color-coded) changes when tuning Kinh (OA concentration) and ec50apc (activity threshold for Cdk1 substrate).

Red, green, blue dotted lines show three different OA period responses.

To gain further insight into the cell cycle period variations over OA, we divided the cell cycle into increasing and decreasing phases, following the previous definitions in experimental analyses. Experimentally, we used securin-CFP as our cell cycle reporter, which is not a model variable. However, both securin and cyclin B are substrates of APC/C, accumulating via protein translation in the interphase and degrading at onset of anaphase, therefore the two proteins should share similar increasing and decreasing phases. Indeed, we found that the trend for cyclin B increasing and decreasing phases in the model resembles that of the securin-CFP in the experiments. We also examined the changes in the duration of increasing and decreasing phases of Cdk1 activity when tuning PP2A. Interestingly, the Cdk1 increasing and decreasing phase durations were conserved across all conditions: the Cdk1 increasing period had always decreased with OA concentration whereas the decreasing period increased. This result suggests that the variations in period response is determined by the relative sensitivity of the increasing/decreasing phase of Cdk1 activity to PP2A inhibition. As illustrated, PP2A inhibition affects both the mitotic entry and exit. During mitotic entry, PP2A inhibition inhibits Wee1 but activates Cdc25, which reduces the threshold of Cdk1 activation and leads to accelerated cell cycle progression. However, during mitotic exit, applying PP2A inhibitor complicates the ability of APC/C to deactivate and leave mitosis, which prolongs the mitotic phase, and at high concentration, it leads to cell cycle arrest.

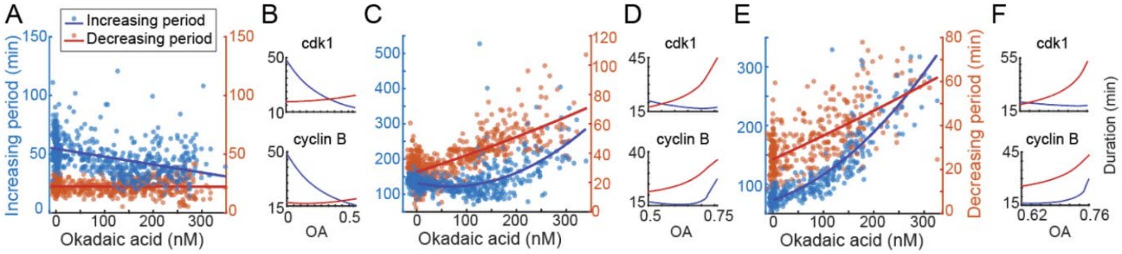

Figure 3.25. Dynamics of different phases of cell cycle in response to PP2A inhibition.

(A)(C)(E) Experimental results of increasing and decreasing period when tuning OA, showing three different types of period response: monotonically decreasing (A), decreasing and then increasing (C), or monotonically increasing (E). Solid lines are fitted curves with linear or quadratic regression. (B)(D)(F) Simulated results of increasing and decreasing period of cyclin B concentration and Cdk1 activity when adding OA, corresponding to three different types of responses.

3.9 Changes in Cell Cycle Oscillation in Response to Both Wee1 and PP2A Inhibition

To understand how both the Cdk1/Cdc25/Wee1 and PP2A/ENSA/Gwl positive feedback loops work together to influence cell cycle period tunability, we simulated the PP2A cell cycle model in response to changes in both Wee1 and PP2A levels (Figure 8B). Interestingly, we found that inhibitions of PP2A (Kinh) and Wee1 reduced each other's range to sustain oscillations. To test this observation, we used the 2-inlet system to generate droplets of Xenopus extract and tuned the concentration of OA under 3 different levels of Wee1 inhibitor PD166285. In support of the model prediction, higher PD166285 indeed reduced the OA tuning range that supports oscillation and the range of the oscillation periods.

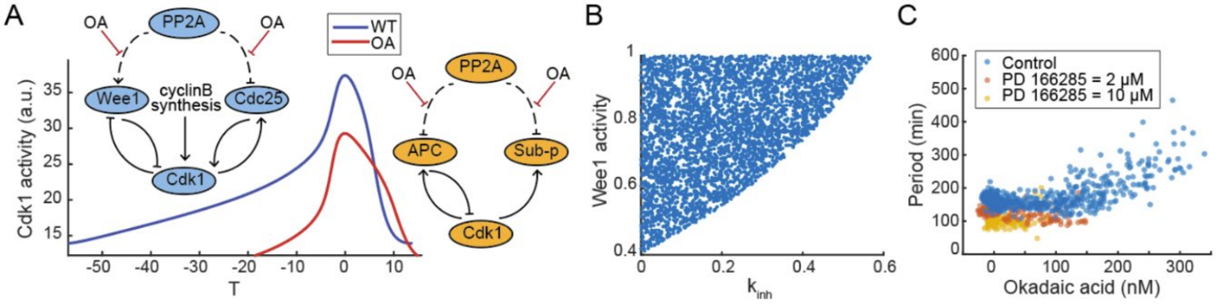

Figure 3.26. Changes in cell cycle oscillation in response to both Wee1 and PP2A inhibition.

(A) Representative time series of Cdk1 activity of WT and OA treated cycles. The schematic molecular circuits show different OA effects during increasing and decreasing phases of oscillation. (B) Oscillatory region when tuning Wee1 activity and Kinh (OA) in a computational model, showing that Wee1 inhibition leads to a smaller region of oscillation when adding OA. (C) Period responses to OA when adding PD166285 in different concentrations.

3.9.1 Four-ODE Model of the Cell Cycle with Cdk1 and PP2A Feedback

The significance of PP2A feedback in cell cycle regulation has been under intense investigation, and many models have been proposed to explain the dynamics of Cdk1-PP2A in cell cycle oscillations. We first tested existing models[3] that describe PP2A response in *Xenopus* extract. While the model predicts cyclinB response well, it only shows little frequency change in Wee1 and PP2A tuning and could not explain polymorphism of PP2A response. Part of the reason could be that the model was constructed early when some of the molecular circuits and their parameters were still unclear.

Here we chose the simplest model that could capture the general dynamics of PP2A feedback with two equations. Combining with the Cdk1-APC system model presented by Yang and Ferrel, we get a four-equation system that could explain the general dynamics of the cell cycle. Since here we consider the PP2A to be the phosphatase that counteracts Cdk1, the fast balancing of substrate reaction from the previous model needs to be modified. Take the example of Cdc25, $\frac{d[cdc25p]}{dt} = k_1[cdk1_{active}](1-[cdc25p]) - k_{-1}[pp2a_{active}]\cdot[cdc25p]$. if we assume $\frac{d[cdc25p]}{dt} = 0$, then $[cdc25p] = \frac{\frac{[cdk1]_{active}}{[pp2a]_{active}}}{\frac{[cdk1]_{active}}{[pp2a]_{active}} + \frac{k_{-1}}{k_1}}$. We added Hill coefficient to account for experimentally observed hypersensitivity. Note that the term with Hill coefficient does not represent the actual reaction mechanism, and it is just used to describe the experimentally observed responses. After incorporating the static Cdc25, Wee1, and APC activity, we get a four-equation system:

$$\frac{d[cdk1_a]}{dt} = k_s - [cdk1_a]\left(a_{\deg} + b_{\deg} \frac{\left(\frac{[cdk1_a]}{[pp2a_a]}\right)^{n\deg}}{\left(\frac{[cdk1_a]}{[pp2a_a]}\right)^{n\deg} + ec50_{\deg}^{n\deg}} \right) + ([cycb] - [cdk1_a])\left(a_{cdc} + b_{cdc} \frac{\left(\frac{[cdk1_a]}{[pp2a_a]}\right)^{ncdc25}}{\left(\frac{[cdk1_a]}{[pp2a_a]}\right)^{ncdc25} + ec50_{cdc25}^{ncdc25}} \right)$$

$$-[cdk1_a]\left(a_{wee1} + b_{wee1} \frac{ec50_{wee1}^{nwee1}}{\left(\frac{[cdk1_a]}{[pp2a_a]}\right)^{nwee1} + ec50_{wee1}^{nwee1}} \right)[cdk1_a]$$

Equation 3

$$\frac{d[cycb\ ]}{dt} = ks - [cycb]\left(a_{\deg} + b_{\deg} \frac{\left(\frac{[cdk1_a]}{[pp2a_a]}\right)^{n\deg}}{\left(\frac{[cdk1_a]}{[pp2a_a]}\right)^{n\deg} + ec50_{\deg}^{n\deg}} \right)$$

Equation 4

$$\frac{d[ENSAP]}{dt} = k_1 \frac{[cdk1_a]^n}{K_{Gwl}^n + [cdk1_a]^n} \cdot \frac{[ENSA]}{K_1 + [ENSA]} - k_{-1}[pp2a_a]\frac{[ENSAP]}{K_{-1} + [ENSAP]}$$
$$-k_2[ENSAP] \cdot [PP2A] + k_{-2}complex$$

Equation 5

$$\frac{d[PP2A]}{dt} = -k_2[ENSAP] \cdot [PP2A] + k_{-2}complex$$

Equation 6

Here the complex represents the PP2A-ENSA complex, note that the PP2A, ENSA, and complex have the following conservation.

$$ENSA_{tot} = [ENSA] + [ENSAP] + complex$$

$$PP2A_{tot} = [PP2A] + complex$$

From the observations of previous research, the PP2A may have two different states, and the Cdk1 activity is positively correlated with higher activity PP2A state, so we have active and basal PP2A concentration with the following expression:

$$[PP2A_p] = [PP2A]\frac{[cdk1_a]}{K_3 + [cdk1_a]}$$

$$[PP2A_b] = [PP2A]\frac{K_3}{K_3 + [cdk1_a]}$$

Then we can calculate PP2A activity based on normalized basal and active PP2A concentration

$$[pp2a_a] = \alpha_{basal}[PP2A_b] + \alpha_{act}[PP2A_p]$$

Upon adding OA, the PP2A activity is modified as

$$[pp2a_a]' = \frac{[pp2a_a]}{1 + K_{inh}}$$

Note that even though Gwl could also be dephosphorylated by PP2A, previous research has suggested that Gwl is mainly regulated by pp1. In addition, hyperphosphorylation is only weakly correlated with Gwl activity. As a result, the inhibitory effect of PP2A on Gwl is not explicitly indicated in our model.

The simulation is performed in MatLab 2019b with ode15s method, relative tolerance= 10e-6 and absolute tolerance =10e-8. The initial condition is [Cdk1$_a$]=10, [cycb]=10, [ENSAP]=0.1, [PP2A]=0.1. We use the same parameters as the original model, and the new parameters are chosen after scans to ensure persistent oscillations.

Parameter	**Value**
k_s	1
a_{deg}	0.01
b_{deg}	0.04
a_{cdc}	0.16
b_{cdc}	0.8

$ec50_{cdc}$	35
n_{cdc}	11
a_{wee}	0.08
b_{wee}	0.4
$ec50_{wee}$	35
n_{wee}	3.5
$ec50_{deg}$	32
n_{deg}	17
k_1	15
K_1	0.1
k_{-1}	1.5
K_{-1}	0.01
k_2	600
k_{-2}	15
n	5
K_3	10
a_{basal}	0.024
K_{Gwl}	100
α_{act}	1.2
$PP2A_{tot}$	1
$ENSA_{tot}$	2

3.10 Conclusions

While mathematical models have often been built to understand biological systems at specific conditions, their effectiveness is difficult to evaluate across perturbed environments. In our study, we have developed a platform to systematically perturb system parameters and utilized it to challenge existing cell cycle models. We found that most cell cycle models could predict the system's response to cyclin B mRNA tuning, but not Wee1 or PP2A perturbations. By combining and modifying existing models, we constructed a new model that could predict all perturbation effects in our study. This approach could help us understand the limitations of current models and identify biological mechanisms that contradict models derived from past hypotheses.

Through global parameter searching, we also made new discoveries for comprehensive understanding of positive feedback regulations on cell cycle dynamics, which would be challenging to recapitulate through low-throughput studies of a few specific phenotypes. Many biological oscillators have well-conserved positive feedback despite that, in theory, single time-delayed negative feedback is sufficient to generate sustained oscillations. Although extensive computational work has been done suggesting that positive feedback may play a role in clock tunability and robustness, essential experimental studies in this regard have been missing. With our platform, we analyzed the whole spectra of phenotypes by high-resolution mapping of the period landscape over perturbations in multiple dimensions, which provides comprehensive information necessary for testing theories and understanding the underlying mechanisms at the systems level. We showed that the previously proposed Cdk1/Cdc25/Wee1 positive feedback only contributes partially to the tunability of the cell cycle and Wee1 inhibition alone could not abolish oscillations. These results inspired us to dissect the role of the additional positive feedback involving PP2A. Intriguingly, we observed multimodal behaviors in both oscillatory percentage and period. While we have not yet fully understood the mechanisms underlying these phenomena, our model suggests that the multimodal behaviors could be explained by the relative sensitivity of Cdk1's substrate Gwl or APC/C to Cdk1. The sensitivity of a substrate can be considered as to how soon the substrate is activated in response to Cdk1 activation. This highlights the importance of the temporal order of activation of APC/C and Gwl, and a slight change in the temporal order of the cell cycle may result in a substantial change in oscillatory patterns.

While it requires future studies to verify these observations in live embryos, our findings in synthetic cells suggested that there could be more than one mode of cell cycle behaviors, and the oscillation properties and the temporal order of mitotic events might vary in these different oscillatory modes. These complex behaviors could not have been detected by the conventional low-throughput and low-resolution network perturbations in live embryos or bulk extract assays. Our high-dimensional, high-throughput, high-resolution framework provides a generalizable strategy to explore the frequency regulation in other biological oscillators, which may lead to a more comprehensive quantitative understanding of this fundamental phenomenon shared by biological clocks.

Chapter 4 Mitotic Oscillator Precision is Governed by ATP-Dependent Free Energy Dissipation

4.1 Introduction

The precise regulation of the cell cycle during early embryonic development relies on a tightly controlled mitotic clock centered around the cyclinB-CDK1 complex. Like information processing and many other biological processes functioning accurately against noise, the accuracy of a far-from-equilibrium oscillatory system like the cell cycle is energetically costly[27,28]. One example of this would be the mitotic circuit, where multiple Phosphorylation/dephosphorylation (PdP) cycles need to occur to ensure the correct progression of the cell cycle, including CyclinB/Cdk1 phosphorylating Wee1 and Cdc25 and Wee1 in turn phosphorylating CyclinB/Cdk1, which are all driven by the free energy generated via ATP hydrolysis, therefore the mitotic oscillations are energy costly.

Theoretical studies have suggested a link between oscillator property and energy dissipation. Wang et al. studied the G2/M transition in yeast cells[28] and discovered that the free energy dissipation shows significant impact on cell cycle dynamics. Phosphorylation energy, the free energy generated from the hydrolysis of 1 mole of ATP is defined as ΔG and $\Delta G=RT\ln\gamma$, where $\gamma=[ATP]/(K_{eq}[ADP][Pi])$ and K_{eq} is the equilibrium constant for ATP synthesis. Using their thermodynamically realistic kinetic model that features reversable reaction steps, they found that in the 2 dimensional parameter space of ΔG and total cdc13/cdc2 (the equivalent of CyclinB/Cdk1 complex in yeast, which from here now on will be referred to as the total

CyclinB/Cdk1 complex or [CyclinB/Cdk1]^T for the interest of this study and to avoid confusion), the 2 parameters synergistically determines the activation of Cdk1, resulting in a finite area that supports the bi-stability of Cdk1 activity, implying that only a certain range of free energy allows mitotic oscillation. Interestingly, there are 2 critical values of ΔG, beyond or below which the system will switch to Cdk1 mono-stability, indicating extreme conditions will arrest oscillations. Furthermore, as ΔG increases, the threshold of total [CyclinB/Cdk1]^T required for Cdk1 activation becomes lower, resulting in a more rapid switching from interphase to mitosis.

From a more generalized angle, the thermodynamic uncertainty relation in biochemical oscillations has been extensively characterized[80]. Regarding the scope of this study specifically, Cao et al. studied the phase diffusion of three basic oscillation motifs shared by oscillatory systems[27]: the activator-inhibitor system, the repressilator, and the substrate-depletion model, of which the activator-inhibitor model closely resembles the mitotic network. By simulating identical oscillator replicates with the same period T using the Gillespie method, they are able to quantity the phase diffusion over time. They discovered a linear relationship between the oscillation peak variance σ^2 and time t: $\sigma^2=Dt$ and defined the dimensionless peak time diffusion constant D/T as a quantitative measurement of the extent of phase diffusion. A larger diffusion constant indicates faster diffusion and lower precision. Furthermore, they defined ΔW to characterize the free-energy dissipation per period per volume, which is determined by cellular concentration [ATP], [ADP], and [Pi]. By scanning the parameter space, they uncovered a relationship between D/T and ΔW: the ΔW dictates the theoretical lower bound of D/T, implying that free energy dissipation determines the highest precision an oscillator can be. Further dissections of the conditions show that this theoretical lower bound of diffusion coefficient is not reached by extreme conditions but when [*ATP*] and [*ADP*]/[*Pi*] are at intermediate values, which could imply there is an optimal energy landscape for accurate oscillations.

However, although theoretical analyses abound, experimental quantification of energy flow at the single-cell level has been challenging. Taking advantage of the droplet-based system, I systematically manipulated ATP levels and network topology and discovered a non-monotonic response in the oscillator's speed and precision. The results reveal that the mitotic oscillator exhibits maximal speed and minimal dephasing at intermediate ATP levels, with the oscillations slowing down rapidly over time. However, as the ATP levels approach the upper and lower bounds that sustain mitotic cycles, the oscillation speed decreases, and the system undergoes a progressively faster dephasing rate. Additionally, the system continues to maintain a higher degree of regularity in its period. These insights shed light on the complex coupling between the free energy budget and the mitotic oscillator performance, suggesting that an optimal energy budget is required to promote fast, yet precise mitotic cycles. Furthermore, we found that manipulating the mitotic circuit design by removing the Wee1/Cdc25 regulations on Cdk1 has an impact on energy dissipation during mitotic entry, demonstrating that intercellular energy flow and dissipation play a crucial role in maintaining cell cycle rate and precision.

The main part of the project is in the stage of wrapping up and a manuscript is currently in the works. Section 4.2 and 4.3 are partially adapted from the published articles *A robust and tunable mitotic oscillator in artificial cells*[38]. I acted as leader in this project and my contributions include conceptualizing the research project; literature scan; experiment design; performing experiments; performing computational and modeling work; data collection, processing, and analysis; analysis script writing; and writing the manuscript.

4.2 Discrete Levels of ATP Effects Oscillation Properties

To explore the energy dependent behaviors experimentally, we first tested droplets supplied with a variety of concentrations of energy mix. We define the standard concentration of energy mix, based on established protocol, as 1×, which when added to the extract results in 1mM extra ATP and corresponding creatine phosphate that constitutes an energy regeneration system. For all energy mix concentrations that we tested (ranging from 0 to 10×) with the vortexing droplet generation system, we initially did not observe any oscillations in droplets with energy mix beyond 2×. We analyzed the oscillation behaviors in droplets prepared from the same batch of extracts except that they were supplied with different concentrations of energy mix (0×, 0.5×, 1×, 1.5×, with each condition performed in duplicates). There is a clear trend of decreasing baseline, amplitude, and period as the amount of energy mix is increasing. The dependence of period and amplitude on the energy level is quantitatively analyzed.

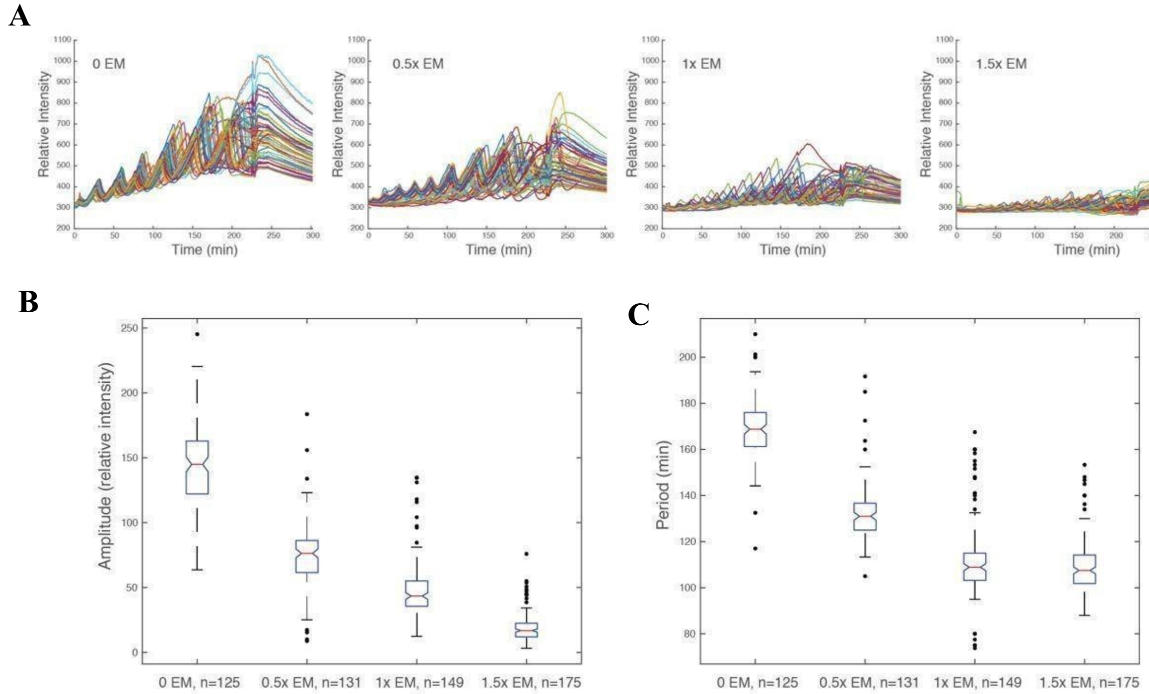

Figure 4.1. Oscillation characteristics with the addition of discrete levels of ATP.

(A) Time traces of individual droplets with different concentrations of energy mix. Each condition has two duplicate experiments and only one is shown. It is evident that the amplitude, baseline, and period decrease as the level of energy mix increases. (B)(C) Amplitude (B) and period (C) decrease as energy mix concentration increases.

The results in chapter 2 indicated that the system is tunable by cyclin B1 mRNA concentration and droplet size in different manners. Although the period and number of cycles responded to varying droplet sizes in opposite directions, they followed the same trend when modulated by cyclin B1 mRNAs, resulting in a lifespan of the oscillatory system sensitive to cyclin B1 mRNA concentration. Moreover, we have observed that securin-mCherry and cyclin B1-YFP both exhibited oscillations of increased amplitude, baseline, and period over time, of which the increasing period over time is evident by analysis. These trends cannot be explained by existing cell cycle models. Unlike intact embryos, cell-free extracts lack yolk as an energy source and lack sufficient mitochondria for energy regeneration. One hypothesis is that energy is an important regulator for a droplet system with a limited amount of energy source consumed over time.

4.3 2-ODE Model Suggest Link ATP Consumption and Cell Cycle Dynamics

4.3.1 Ratio of Energy Intensive Enzymes Wee1/Cdc25 Alters Cell Cycle Dynamics

To gain insights into our experimental observations and better understand the in vitro oscillator system, we first explored how energy consumption plays a role in modulating the oscillation behaviors. The energy depletion model is based on a well-established cell-cycle model modified by introducing ATP into all phosphorylation reactions.

In the cell cycle network, the activation of Cdk1 is co-regulated by double-positive feedback through a phosphatase Cdc25 and a double negative feedback through a kinase Wee1. The balance between Wee1 and Cdc25 activity was suggested to be crucial for the transition of cell cycle status during early embryo development[81]. In light of this, we defined the balance between Wee1 and Cdc25 by the ratio $R=k_{Wee1}[Wee1]/k_{Cdc25}[Cdc25]$. We noted that ATP-dependent phosphorylation of Cdc25 and Wee1 can decrease R by activating Cdc25 and inhibiting Wee1 simultaneously, resulting in a high dependence of R on the ATP concentration.

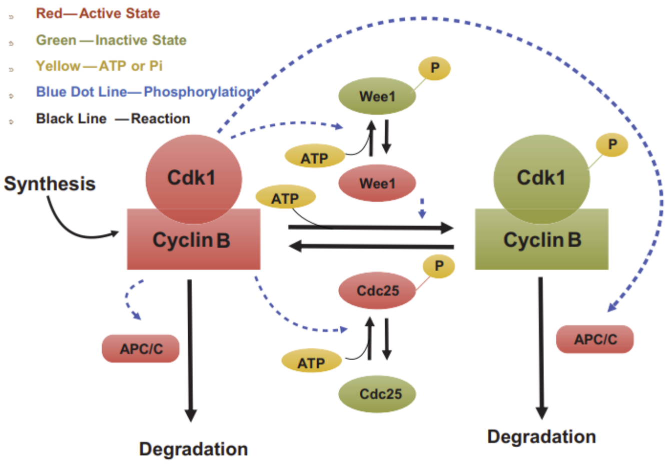

Figure 4.2. Schematic view of the cyclin B-Cdk1 oscillation system.

Note that ATP is taken into consideration. Activated molecules are marked in red, inactivated molecules in green and ATP or Pi in yellow. Black line indicates a reaction and blue dotted line a phosphorylation.

Using this model, we further investigated the relationship between ATP and the oscillation behaviors. We introduce a parameter r into our system to systematically change the ratio R. the results show that at a low r (e.g. 0.5), the system stays at a stable steady-state with low cyclin B concentration and at a high r (e.g. 2.5), the oscillation is arrested at a stable steady-state with high cyclin B concentration. At an intermediate value, increasing r can produce oscillations of increased amplitude, baseline and period. If we assume that the available ATP concentration decreases over time, we can readily recapitulate the experimentally observed increment of amplitude, baseline, and period of the cyclin B time course. The energy depletion model can also predict the experimental observations by showing that both period and number of cycles decrease with increasing cyclin B concentration. However, the changes of synthesis and degradation rates yielded no obvious effects on the amplitude and baseline.

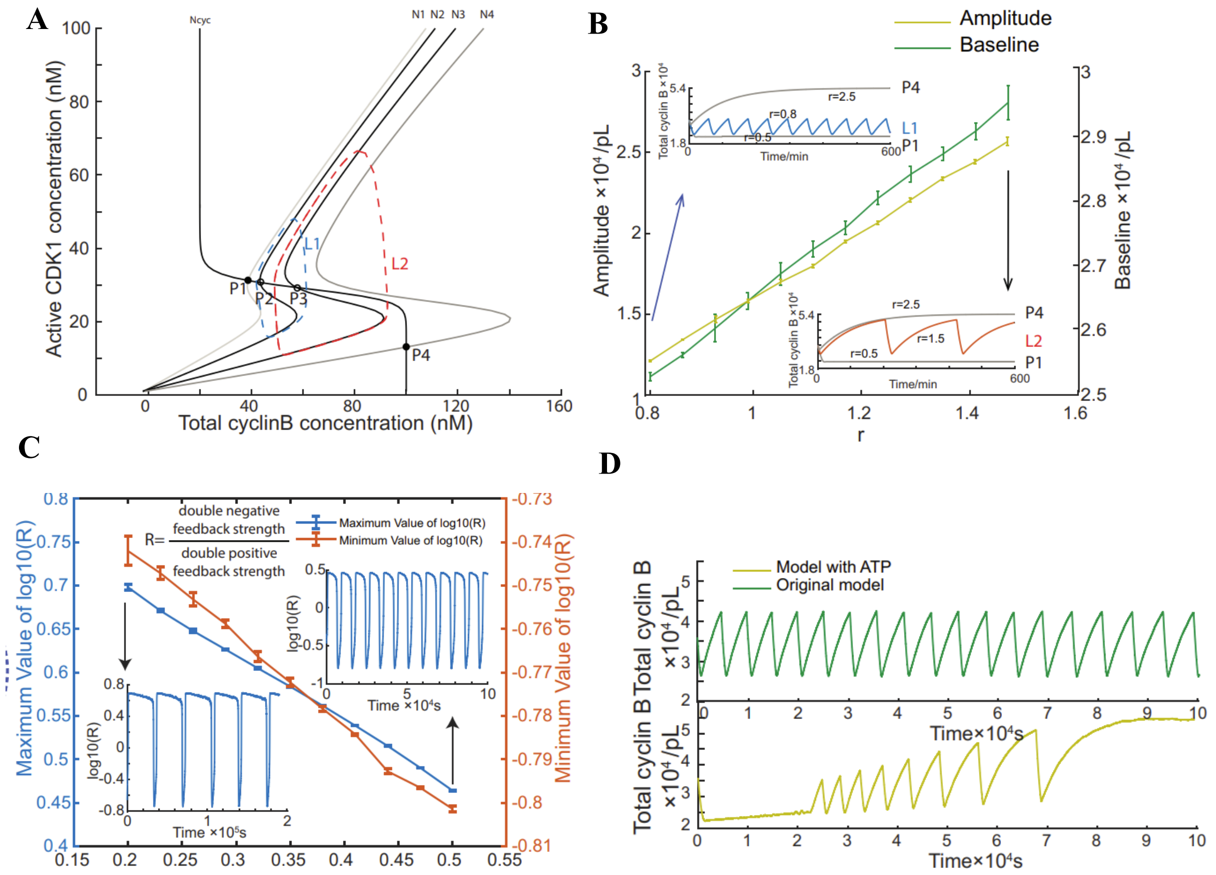

Figure 4.3. Simulated results of oscillation properties when changing the positive feedback strength ratio of Wee1/Cdc25.

(A) Phase plots of the two-ODE model. Parameters for the cyclin B nullcline (Ncyc) and the Cdk1 nullclines with a variety of values of r (N1, r = 0.5; N2, r = 0.8; N3, r = 1.5; N4, r = 2.5) were chosen based on previous experimental work[23,24]. Note that the r here is a parameter and is different from R in Figure 3B. Two sample traces of limit cycle oscillations are plotted for r = 0.8 (L1) and r = 1.5 (L2), showing that a larger r value leads to a higher amplitude and baseline. In addition, r = 0.5 (N1) generates a low stable steady-state of cyclin B (P1), while r = 2.5 (N4) a high stable steady-state of cyclin B (P4). These stable steady-states are indicated by the intersections of the nullclines (filled circles). The unstable steady states are labeled with open circles (P2 and P3). (B) Relationship between the oscillation baseline and amplitude values and ATP concentration (positively correlated with r). Error bars indicate the ranges of 3 replicates. Inserts show two example time courses of total cyclin B with different r values (L1, r = 0.8; L2, r = 1.5), colors of which match the ones in Figure 3C. Simulation is done using Gillespie algorithm. (C) Relationship between ATP percentage and R value, showing that decreasing the ATP concentration leads to a higher R value. Error bars represent ranges from three simulations. Two inserts represent the dynamics of R value over time when the ATP percentage [ATP]/([ATP]+[ADP]) is set as 0.2 (left) and 0.5 (right). The model is simulated using the Gillespie algorithm. (D) Time series of total cyclin B molecules from the model without ATP (top panel, green line) and with ATP (bottom panel, yellow line).

Our energy depletion model suggested an interesting mechanism to modulate oscillations with a single control parameter r that depends on the energy-tunable balance of two positive feedback loops. Considering that the rapid, synchronous cleavages of an early embryo require a large amount of energy that remains unchanged for the first cleavage stages before rapidly dropping until the mid-blastula stage when cell cycles slow down[82], this energy-dependent control may function as a ‘checkpoint’ to regulate cell cycles when r becomes large.

4.3.2 A Two-ODE Model of the Embryonic Cell Cycle and Stochastic Simulations

Complicated models have been proposed to describe the embryonic cell cycle oscillation[16,22,49,83]. However, simple two-ODE models with fewer parameters are more amenable to analysis, while still capturing the general property of the feedback loops. We described the net productions of cyclin B1 and active cyclinB-Cdk1 complex [Cdk1$_a$] using the following two equations[25,81]:

$$\frac{d}{dt}[CyclinB] = k_{sy} - k_{\mathrm{deg}}[CyclinB] = k_{sy} - \left(a_{deg} + \frac{b_{deg}[Cdk1_a]^{n_{deg}}}{[Cdk1_a]^{n_{deg}} + EC50_{deg}^{n_{deg}}}\right)[CyclinB] \tag{1}$$

$$\begin{aligned}\tfrac{d}{dt}[Cdk1_a] &= k_{sy} + k_{\mathrm{Cdc25}}[Cdc25-Pi]([CyclinB]-[Cdk1_a]) - k_{\mathrm{Wee1}}[Wee1][Cdk1_a] \\ &\quad - k_{deg}[Cdk1_a] \\ &= k_{sy} \\ &\quad + \tfrac{1}{\sqrt{r}}\left(a_{Cdc25} + \tfrac{b_{Cdc25}[Cdk1_a]^{n_{Cdc25}}}{[Cdk1_a]^{n_{Cdc25}} + EC50_{Cdc25}^{n_{Cdc25}}}\right)([CyclinB]-[Cdk1_a]) \\ &\quad - \sqrt{r}\left(a_{Wee1} + \tfrac{b_{Wee1}EC50_{Wee1}^{n_{Wee1}}}{[Cdk1_a]^{n_{Wee1}} + EC50_{Wee1}^{n_{Wee1}}}\right)[Cdk1_a] \\ &\quad - \left(a_{deg} + \tfrac{b_{deg}[Cdk1_a]^{n_{deg}}}{[Cdk1_a]^{n_{deg}} + EC50_{deg}^{n_{deg}}}\right)[Cdk1_a]\end{aligned} \tag{2}$$

k_{sy}	1 nM/min
a_{wee1}	0.08 nM/min
b_{wee1}	0.4 nM/min
n_{wee1}	3.5
$EC50_{wee1}$	35 nM
a_{cdc25}	0.16 nM/min
b_{cdc25}	0.8 nM/min
n_{cdc25}	11
$EC50_{cdc25}$	30 nM
a_{deg}	0.01 nM/min
b_{deg}	0.04 nM/min
n_{deg}	17
$EC50_{deg}$	32 nM

Here, [CyclinB] and [$Cdk1_a$] refer to the concentrations of cyclin B1 and active cyclin B1-Cdk1 complex. [Wee1] is the concentration of active Wee1, while [Cdc25-Pi] is the concentration of active Cdc25. We assumed that Cyclin B1 is synthesized at a constant rate. Its degradation rate is dependent on Cdk1 activity in the form of a Hill function with an exponent of 17[25]. Active cyclin B1-Cdk1 complex can also be eliminated through cyclin degradation. In addition, we considered the concentration of Cdk1 to be high compared to the peak concentration of cyclin B1[84,85] and the affinity of these cyclins for Cdk1 to be high[86]. Thus, there is no unbound form of cyclin B1, and the newly synthesized cyclin B1 is converted to cyclin-Cdk1 complexes, which are rapidly phosphorylated by the Cdk-activating kinase CAK to produce active Cdk1. According to previous studies, these complexes can then be inactivated by Wee1 and re-activated by Cdc25, via the double-negative and positive feedback loops, with Hill exponent of n_{Wee1} as 3.5 and n_{Cdc25} as 11[56,57]. We use a free parameter r, representing the ratio of the double negative and double positive feedback strengths, to permute the balance between the two feedback. This balance is suggested to be critical for oscillatory properties[81]. Note that this r is a parameter while R in the main text is a measurement that changes over a simulation. In droplets that have small volumes and contain small numbers of molecules, the stochastic nature of the underlying biochemical reactions must be considered. We adapted a stochastic two-ODE model[25], and converted our two-ODE model to the corresponding chemical master equations[87] and carried out numerical simulations using the Gillespie algorithm[88].

Table 1. Reaction rates and stoichiometry of the two-ODE model.

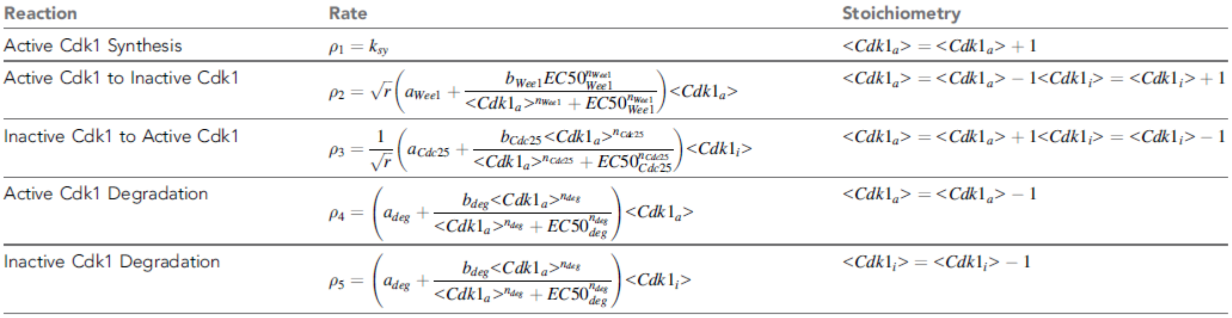

Reaction	**Rate**	**Stoichiometry**
Active Cdk1 Synthesis	$\rho_1 = k_{sy}$	$<Cdk1_a> = <Cdk1_a> + 1$
Active Cdk1 to Inactive Cdk1	$\rho_2 = \sqrt{r}\left(a_{Wee1} + \frac{b_{Wee1} EC50_{Wee1}^{n_{Wee1}}}{<Cdk1_a>^{n_{Wee1}} + EC50_{Wee1}^{n_{Wee1}}}\right)<Cdk1_a>$	$<Cdk1_a> = <Cdk1_a> - 1 <Cdk1_i> = <Cdk1_i> + 1$
Inactive Cdk1 to Active Cdk1	$\rho_3 = \frac{1}{\sqrt{r}}\left(a_{Cdc25} + \frac{b_{Cdc25} <Cdk1_a>^{n_{Cdc25}}}{<Cdk1_a>^{n_{Cdc25}} + EC50_{Cdc25}^{n_{Cdc25}}}\right)<Cdk1_i>$	$<Cdk1_a> = <Cdk1_a> + 1 <Cdk1_i> = <Cdk1_i> - 1$
Active Cdk1 Degradation	$\rho_4 = \left(a_{deg} + \frac{b_{deg} <Cdk1_a>^{n_{deg}}}{<Cdk1_a>^{n_{deg}} + EC50_{deg}^{n_{deg}}}\right)<Cdk1_a>$	$<Cdk1_a> = <Cdk1_a> - 1$
Inactive Cdk1 Degradation	$\rho_5 = \left(a_{deg} + \frac{b_{deg} <Cdk1_a>^{n_{deg}}}{<Cdk1_a>^{n_{deg}} + EC50_{deg}^{n_{deg}}}\right)<Cdk1_i>$	$<Cdk1_i> = <Cdk1_i> - 1$

To explore how energy consumption could affect the oscillations, we took ATP into account for phosphorylation and dephosphorylation of Wee1[89], such that:

$$Wee1 + ATPWee1 - Pi + ADP \tag{3}$$

In our model, we assumed Wee1 is in equilibrium with the activity of Cdk1 due to fast reactions between Cdk1 and Wee1. Using the reaction coefficients for Wee1 phosphorylation as k1Wee1 and that for Wee1-Pi dephosphorylation as k2Wee1, along with the steady-state approximation, we have:

$$k_{1Wee1}[Wee1][ATP] = k_{2Wee1}[Wee1 - Pi][ADP] \quad = k_{2Wee1}([Wee1_{tot}] - [Wee1])(1 - [ATP]) \tag{4}$$

All above modifications for Wee1 reactions were also applied to Cdc25. After normalizing [ATP] and [ADP] by [ATP]+[ADP], we have the updated reaction rates summarized in Table 2. Here the $[Wee1]_0$ and $[Cdc25\text{-}Pi]_0$ represent the steady-state concentration of active Wee1 and Cdc25 when ATP is not considered in reaction. The ratios of the steady state to total concentrations of Wee1 and Cdc25 can be calculated as a function of active Cdk1 using the parameters from Novak and Tyson's previous work[16].

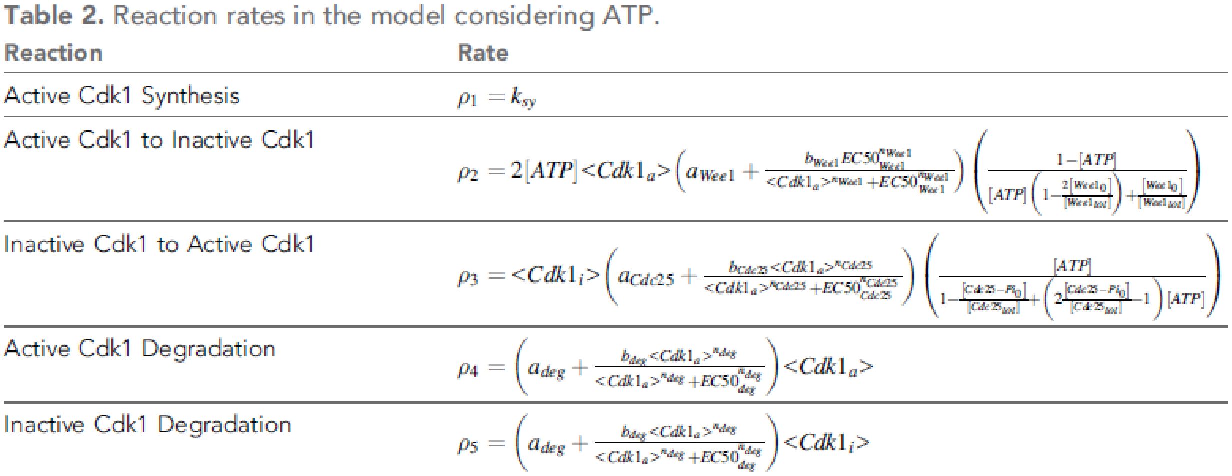

Table 2. Reaction rates in the model considering ATP.

Reaction	Rate
Active Cdk1 Synthesis	$\rho_1 = k_{sy}$
Active Cdk1 to Inactive Cdk1	$\rho_2 = 2[ATP]{<}Cdk1_a{>}\left(a_{Wee1} + \frac{b_{Wee1}EC50_{Wee1}^{n_{Wee1}}}{{<}Cdk1_a{>}^{n_{Wee1}} + EC50_{Wee1}^{n_{Wee1}}}\right)\left(\frac{1-[ATP]}{[ATP]\left(1-\frac{2[Wee1_0]}{[Wee1_{tot}]}\right)+\frac{[Wee1_0]}{[Wee1_{tot}]}}\right)$
Inactive Cdk1 to Active Cdk1	$\rho_3 = {<}Cdk1_i{>}\left(a_{Cdc25} + \frac{b_{Cdc25}{<}Cdk1_a{>}^{n_{Cdc25}}}{{<}Cdk1_a{>}^{n_{Cdc25}} + EC50_{Cdc25}^{n_{Cdc25}}}\right)\left(\frac{[ATP]}{1-\frac{[Cdc25-Pi_0]}{[Cdc25_{tot}]}+\left(2\frac{[Cdc25-Pi_0]}{[Cdc25_{tot}]}-1\right)[ATP]}\right)$
Active Cdk1 Degradation	$\rho_4 = \left(a_{deg} + \frac{b_{deg}{<}Cdk1_a{>}^{n_{deg}}}{{<}Cdk1_a{>}^{n_{deg}} + EC50_{deg}^{n_{deg}}}\right){<}Cdk1_a{>}$
Inactive Cdk1 Degradation	$\rho_5 = \left(a_{deg} + \frac{b_{deg}{<}Cdk1_a{>}^{n_{deg}}}{{<}Cdk1_a{>}^{n_{deg}} + EC50_{deg}^{n_{deg}}}\right){<}Cdk1_i{>}$

4.4 Quantitatively Manipulating Energy Level and Energy-Intensive Components of The Mitotic Circuit

As described in Chapter 3, the introduction of microfluidic devices enables fine-tuning of extract components. In order to comprehensively map how the intracellular energy landscape affects oscillator performance, we tuned the ATP level in cycling extracts by either adding ATP or adding apyrase to deplete ATP using a two-inlet microfluidic device. The change of ATP level in extracts has been verified through various assays. The Luciferase assay, for example, relies on the Firefly luciferase's use of ATP to oxidize D-Luciferin and the resulting production of light in order to assess the amount of ATP available in cell cultures. Aliquots were taken from bulk extracts at different time points after calcium activation to assess ATP level. When adding 1× energy mix, which is the suggested amount based on established protocols, the ATP concentration stayed relatively constant for at least 12 hours, significantly longer than the first 1 to 3 cycles (which are used for most statistical analysis in this study) would typically take. When supplied with different amounts of ATP, the ATP concentration surprisingly stayed constant at the adjusted level, which might suggest unidentified cellular mechanisms have participated in maintaining ATP level.

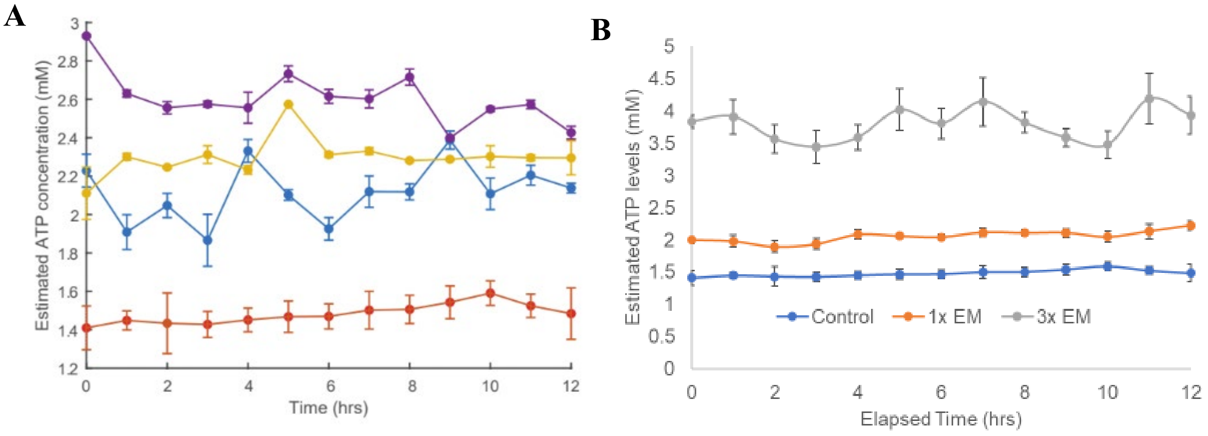

Figure 4.4. Luciferase assay measuring extract ATP concentration.

(A) ATP concentration of control extracts without ATP addition over time. (B) ATP concentration of extract supplied with 0×, 1×, 3× EM, respectively, over time.

A ratiometric single-fluorophore protein QUEEN, which is a circularly permuted enhanced green fluorescent protein (cpEGFP) inserted between 2 α-helices of the bacterial F_0F_1-ATP synthase ε subunit, whose fluorescent property is dependent on whether or not bound to an ATP molecule, was also added to droplets for live ATP concentration reporting. At t=0 of time-lapse imaging sessions, the ratio of fluorescent intensity at different excitation wavelengths shows the droplet ATP levels change as intended with ATP or apyrase addition. However, due to the high sensitivity of QUEEN to photobleaching and sensitivity to environmental cues such as pH, real-time QUEEN signals remain difficult to interpret. Nevertheless, with the combination of both QUEEN measurement and luciferase assay, it can be concluded that tuning ATP levels in our microfluidic system is achieved.

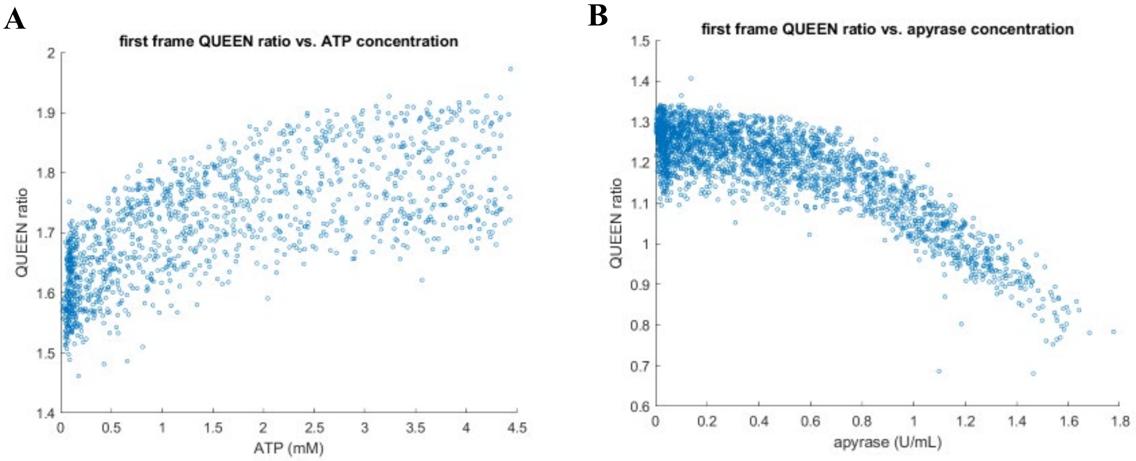

Figure 4.5. QUEEN measurements of droplet ATP concentration at t=0.

(A) QUEEN measurements of droplets with tuned ATP addition. (B) QUEEN measurements of droplets with tuned apyrase addition.

Tuning ATP in droplets has yielded several interesting observations. Based on the percentage of oscillating droplets, which is an indicator of the probability of oscillation, at different ATP or apyrase levels, only certain ATP concentration supports oscillation (figure 4.6). Combining the tuning results of ATP and apyrase, it is clear that when approaching a certain high or low ATP level, the oscillation percentage rapidly approaches zero. As [ATP] directly determines ΔG, this result is reminiscent of the predicted bifurcations when changing ΔG in Wang et al. described in section 4.1.

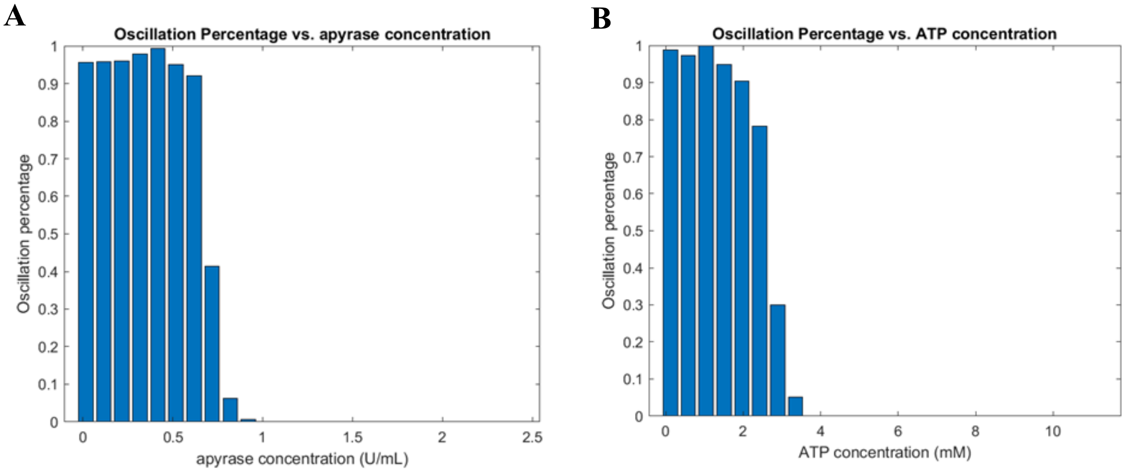

Figure 4.6. percentage of oscillating droplets at different ATP concentration levels. (A) droplets with tuned apyrase addition. (B) droplets with tuned ATP addition.

Furthermore, the mitotic oscillator is able to change its oscillation frequency in response to changing energy levels. While depleting ATP with apyrase results in gradually slower oscillation speed, supplying extra ATP causes a non-monotonic response (figure 4.7). There seems to be an optimal ATP concentration where the oscillator can achieve maximal speed. This phenomenon is reproducible using different batches of eggs in different experiments with the same setup. The optimal ATP concentration is approximately in the range of [0.5, 1.5] mM, the variability is probably due to the different endogenous ATP concentrations among different egg batches.

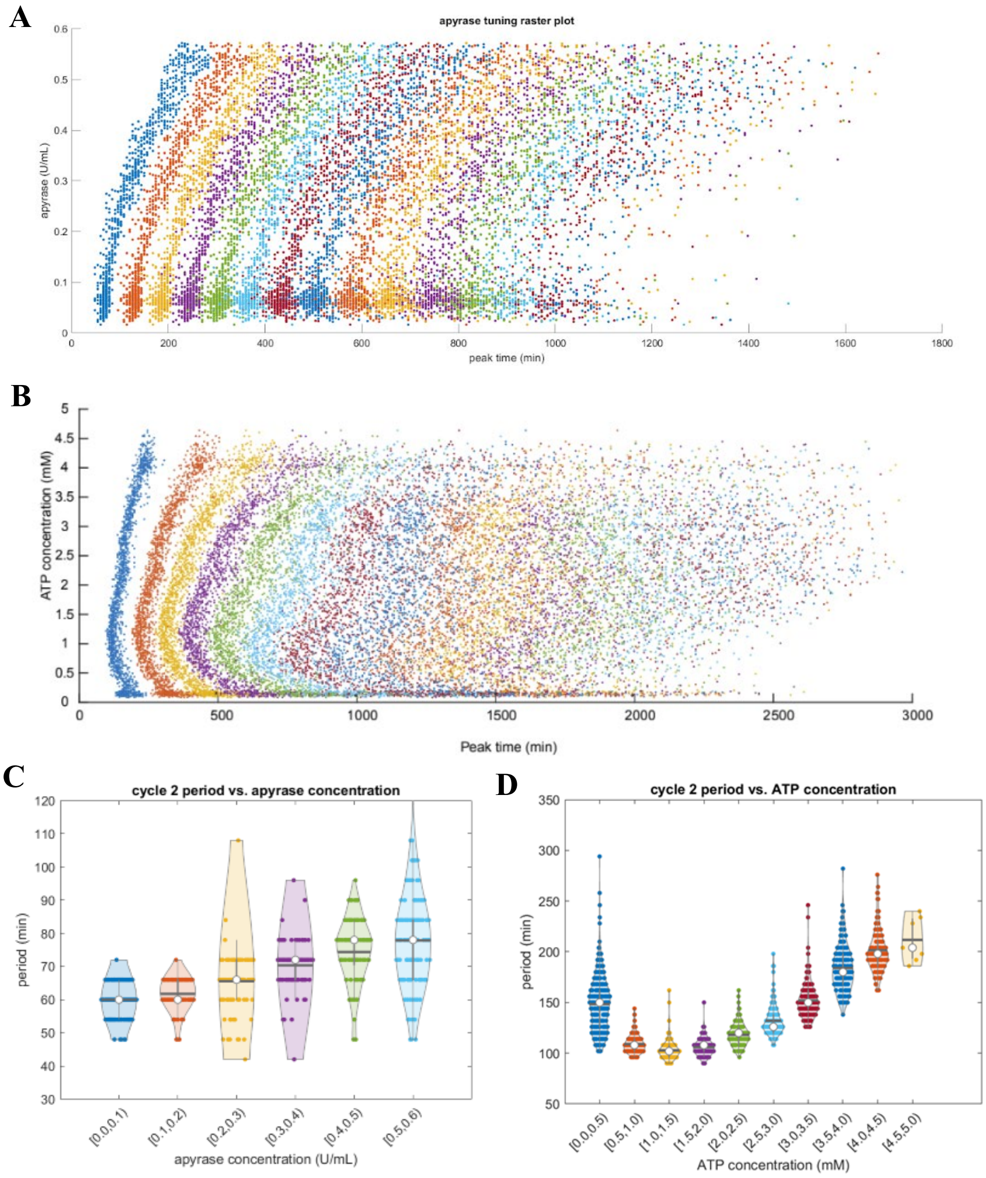

Figure 4.7. Non-monotonic changes in oscillation behavior in response to ATP concentration changes.

(A) raster plot of droplets with tuned apyrase addition. (B) raster plot of droplets with tuned ATP addition. (C) violin plot of first cycle period vs. apyrase concentration. (D) violin plot of first cycle period vs. ATP concentration.

Observations of various raster plots of the ATP/apyrase tuning experiments also led to the exploration of whether available energy plays a role in the time-keeping capabilities of the mitotic oscillator, especially oscillation accuracy. As described in section 4.1, the available free energy determines the upper bound of oscillation accuracy[27] and the highest accuracy was not achieved by extreme conditions but at a specific intermediate [*ATP*] and [*ADP*]/[*Pi*] ratio. Some initial observations seem to suggest the lowest phase diffusion seems to coincide with the previously mentioned optimal ATP concentration for oscillation speed (figure 4.8), which is in agreement with theoretical works, although further analysis is needed to correctly isolate the effect of varying periods from phase diffusion quantification, and also untangle multiple factors which can potentially introduce noise to the oscillator.

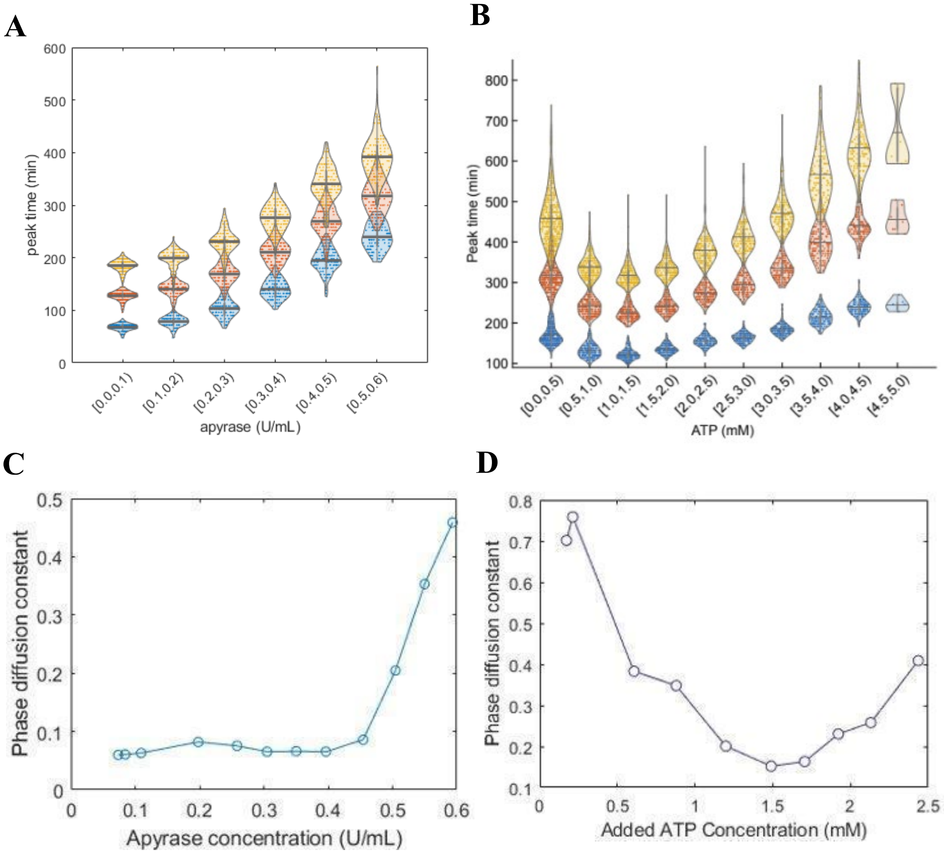

Figure 4.8. Non-monotonic changes in oscillation behavior in response to ATP concentration changes.

(A) violin plot of peak spread of the first 3 cycles of droplets with tuned apyrase addition. (B) violin plot of peak spread of the first 3 cycles of droplets with tuned ATP addition. (C) calculated phase diffusion constant vs. apyrase concentration. (D) calculated phase diffusion constant vs. ATP concentration.

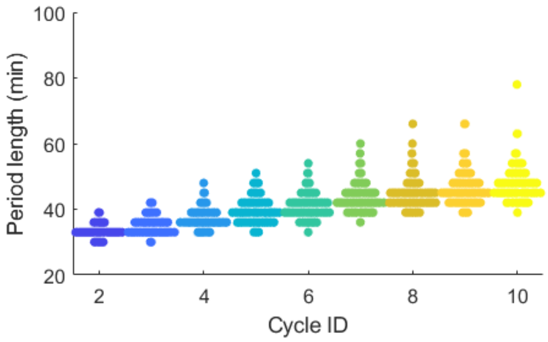

Figure 4.9. Oscillation period changes over time.

However, several discrepancies between my experimental results and Cao et al.'s simulation results made it difficult to directly implement the same analysis pipeline. Cao et al. assume statistically identical oscillators with constant periods. In their studies, stochastic reaction simulations were performed on oscillators with identical volumes and concentrations of chemical species. The phase diffusion coefficient *D* was defined as the rate of increase in peak time variance over successive cycles, serving as an inverse measure of precision. However, extract droplets in our system do not exhibit constant cycle periods over time (figure 4.9). Rather, we observe an approximately linear trend in the peak time standard deviation and therefore a quadratic peak time variance over time (figure 4.10). Secondarily, the period of oscillations is both a function of time and highly tunable with changes of ATP in solution. the oscillation period is not constant across different ATP concentrations (figure 4.7). As a result, linear fitting of σ^2=Dt for diffusion constant D/T is no longer practical.

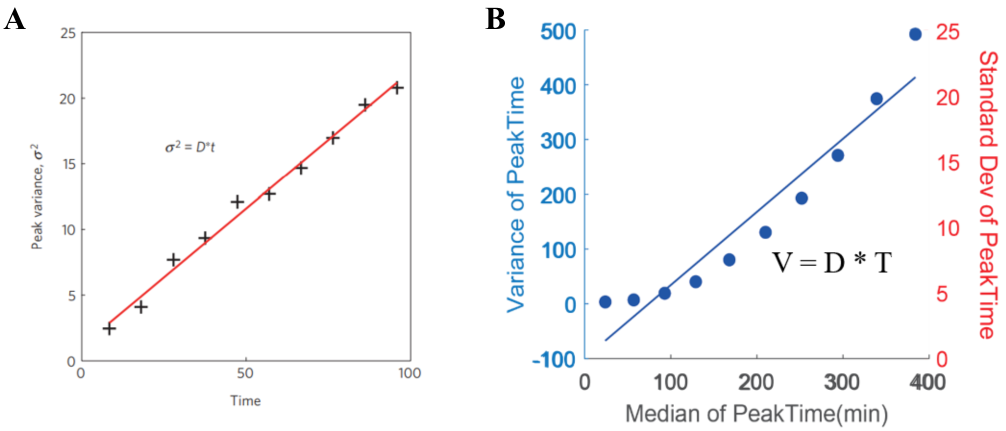

Figure 4.10. Discrepancies in analyzing simulation and experimental results.

(A) Linear fitting for diffusion constant D with simulated results. Reproduced from Cao et al. 2015[27]. (B) Linear fitting for diffusion constant D with experimental results.

To address this, we performed a phase correction, enabling the extraction of a phase diffusion coefficient that incorporates information about oscillation accuracy and facilitates comparisons across oscillators with varying intrinsic periodicities. For droplets that are replicates with identical conditions, this phase correction consists of a renormalization of each peak time distribution into 2π intervals. Medians of each peak time are designated as the standard peaks with phases 2π, 4π, 6π etc. and the timepoints in between are linearly interpolated from actual times to phases. This phase correction eliminates the changing periods over time, allowing the aforementioned method of calculating phase diffusion coefficient to be implemented to evaluate oscillation precision.

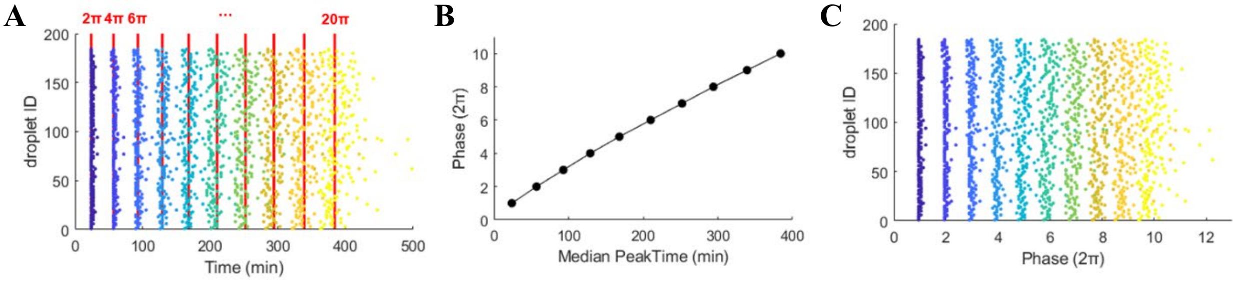

Figure 4.11. Phase correction for droplets with identical conditions.

(A) Raster plot before phase correction. Medians of each peak time are defined as real peaks. (B) linear interpolation to convert peak time information to phase information. (C). Raster plot after phase correction.

Similarly, when processing 2-channel tuning datasets, the droplets are binned according to ATP or apyrase concentration. Each bin is then phase-corrected using the same described method. Phase diffusion constants are then calculated and compared among different bins. Agreeing with previous observations, depleting ATP with apyrase significantly diminishes the oscillator's performance in precision (figure 4.12), while supplying additional ATP results in a non-monotonic response (figure 4.13). Although the highest precision still occurs at an intermediate ATP concentration, extremely high ATP level also exhibits higher precision contrary to previous analyses (figure 4.8), and the overall precision tend to increase instead of exhibiting a convex shape.

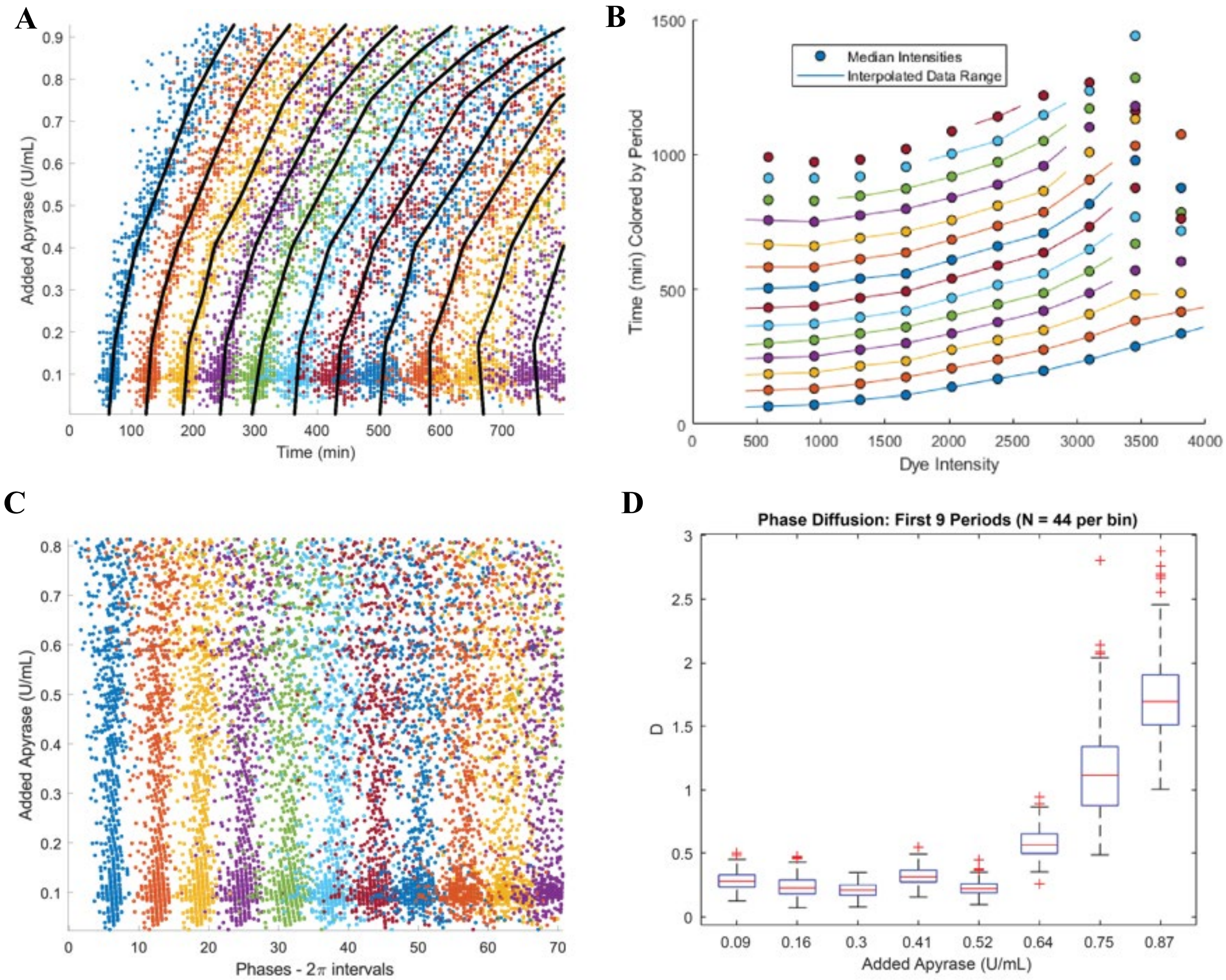

Figure 4.12. Phase-correcting apyrase tuning results and calculating phase diffusion coefficient.

(A) Raster plot before phase correction. Sample points are binned according to apyrase concentration, the median peak times are calculated for each bin at each cycle. Black lines represent connected lines of the medians. (B) Extracted median for binned droplets at each cycle. (C) Raster plot after phase correction. (D) Phase diffusion constants calculated for each bin. The first 9 cycles are used for linearly fitting for diffusion constant.

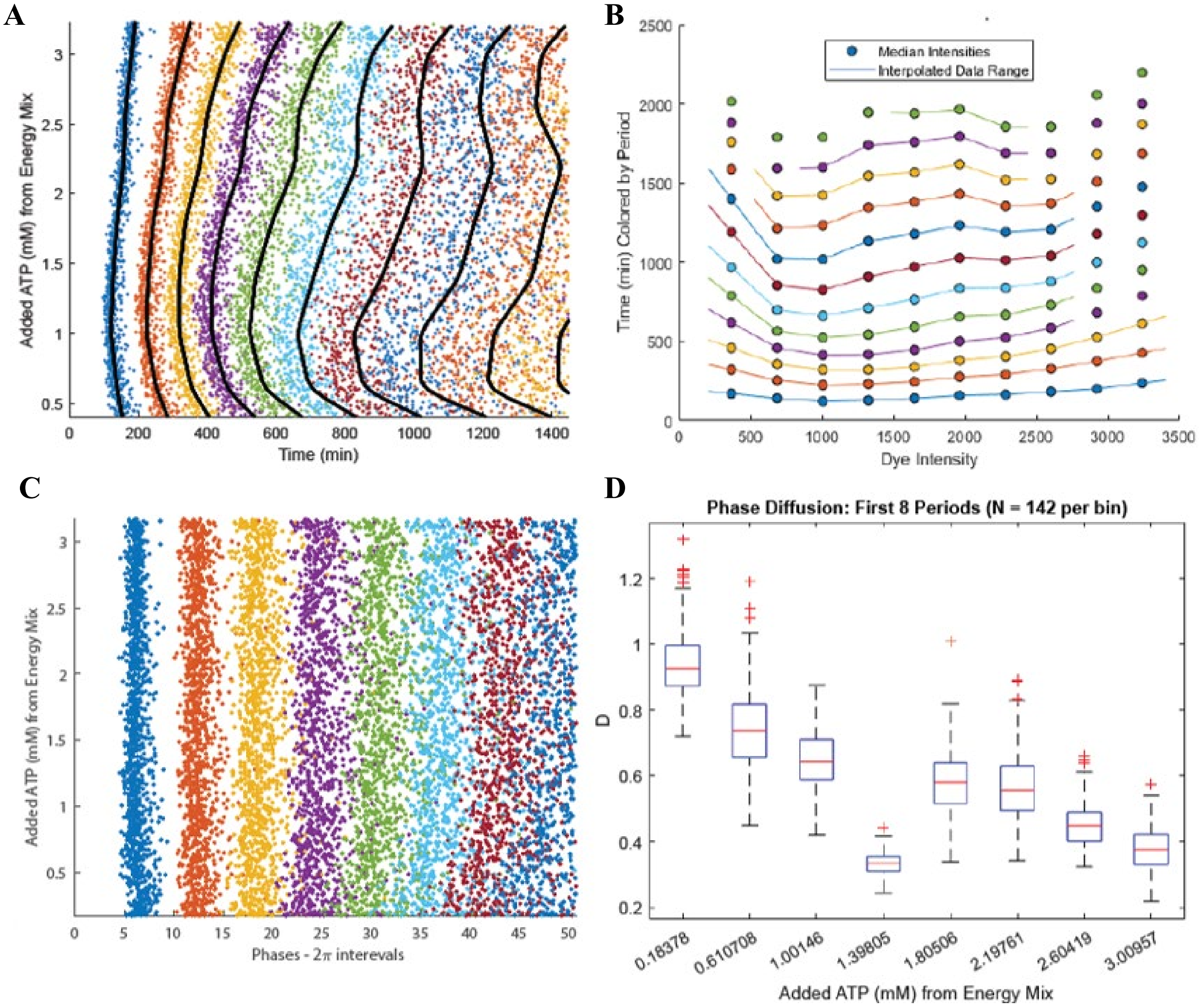

Figure 4.13. Phase-correcting ATP tuning results and calculating phase diffusion coefficient.

(A) Raster plot before phase correction. Sample points are binned according to ATP concentration, the median peak times are calculated for each bin at each cycle. Black lines represent connected lines of the medians. (B) Extracted median for binned droplets at each cycle. (C) Raster plot after phase correction. (D) Phase diffusion constants calculated for each bin. The first 8 cycles are used for linear fitting for diffusion constant.

Although phase correction analysis showed promising results, the quadratic trend in peak variance was still present after the phase correction, this indicated that there are sources of drift in the experimental system that are not accounted for in the stochastic simulations previously studied. During droplet encapsulation the population of oscillators may be not, strictly speaking, statistically identical oscillators. Encapsulation errors during droplet generation may give rise to a drift in the phase diffusion constant D, as one or more major components of the oscillatory network now exist as some normal distribution of possible concentrations. Additionally, as this is an early embryonic system, many components are dynamically variable within the droplet as several mRNAs are passively translated and proteins are under constant synthesis and degradation. This leads to a network that is not contained to a single limit cycle, but rather a distribution of limit cycles where the phase space of the limit cycles is also a function of time. These features of the experimental data are difficult to remove. Therefore, future analyses will aim to correct the drift in peak times to better quantify the phase diffusion of the network.

Besides comparing the characteristics of one cycle among different ATP levels, I also compared the oscillator's ability to maintain a constant cycle period over time. The amplitudes of individual droplet tracks were normalized and autocorrelation function is then calculated to compare the similarity of the track at any two given time points. The autocorrelation function was then fitted to a dampened oscillation which decays exponentially:

$$\begin{aligned} C(t) &\equiv \frac{\langle (x(t+s)-\langle x\rangle)(x(s)-\langle x\rangle)\rangle_s}{\langle x^2\rangle - \langle x\rangle^2} \\ &= \exp(-t/\tau_c) \times \cos(2\pi t/T) \end{aligned}$$

The coefficient τ_c, defined as the coherence time, can therefore quantify how fast the autocorrelation decays, thus how similar the oscillations over time.

Initial analysis shows a similar non-monotonic trend similar to that observed in period and phase diffusion as described above: coherence time is the lowest at the optimal ATP concentration and increases when ATP is changed either way, which seems to imply a tradeoff between long term stability and speed/accuracy. Surprisingly, when adding apyrase, coherence time also increases. However, similar to previous reasonings for phase correction analysis, these initial analysis methods need to be optimized to eliminate the effects of changing periods and poor fitting of the autocorrelation function so that the validity of the current findings remains to be seen.

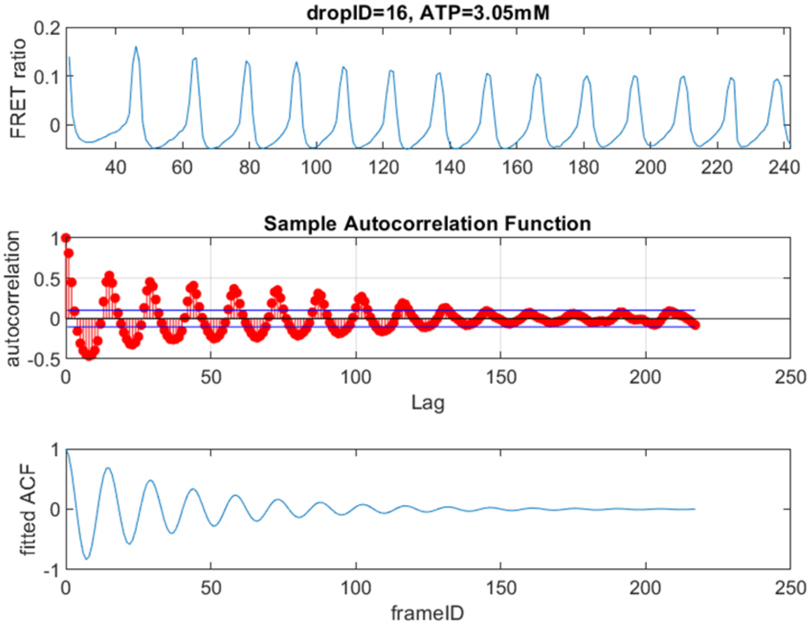

Figure 4.14. Autocorrelation function calculation and fitting for coherence time.

Top, partial oscillation track of an individual droplet. Middle, autocorrelation function of the track. Bottom, fitted damped oscillation.

4.5 Conclusion

Existing results show promise of unveiling the relationship between the energy landscape and oscillator properties. However, much is still to be explored. Although an interesting non-monotonic dependency is observed, further analysis and experimentation are needed to explain the phenomenon. New statistical methods, such as phase correcting the oscillation peaks and drift correcting to account for encapsulation errors, are need to further isolate oscillation properties from multiple interfering factors. While the droplet system is already a stripped-down version of the cell cycle without DNA replication, cell growth, cytokinesis and division, the use of whole cytosolic material still creates a complex environment in which what other mechanisms participate in energy production and consumption is still not fully understood, especially when the mitotic cycle is progressing constantly. New experimental designs have been proposed and tested with promising results, including Isothermal titration calorimetry (ITC), which saw successful implementation on zebrafish embryos and revealed periodic heat release cycle coinciding with cell cycle[90]; real-time cell metabolic analysis, which detect ATP production and consumption by monitoring oxygen consumption and intracellular acidification; mitochondrial inhibition, which allows more effective manipulation of ATP production; high-speed cycling extracts, which removes the mitochondria completely from the extract to create a purer system. To establish a link between energy sensing and PdP cycle dynamics, explorative tests have also been made by inhibiting the energy-intensive double positive and double-negative feedback loop with Wee1 or Cdc25 inhibitors (figure 4.15). In theory, by disabling these feedback loops, we expect to see dramatic changes in oscillatory behavior, however interpreting these results have been challenging. Overall, the current findings pose interesting questions regarding the cell’s usage of the energy budget and provide a solid foundation for many potential research topics.

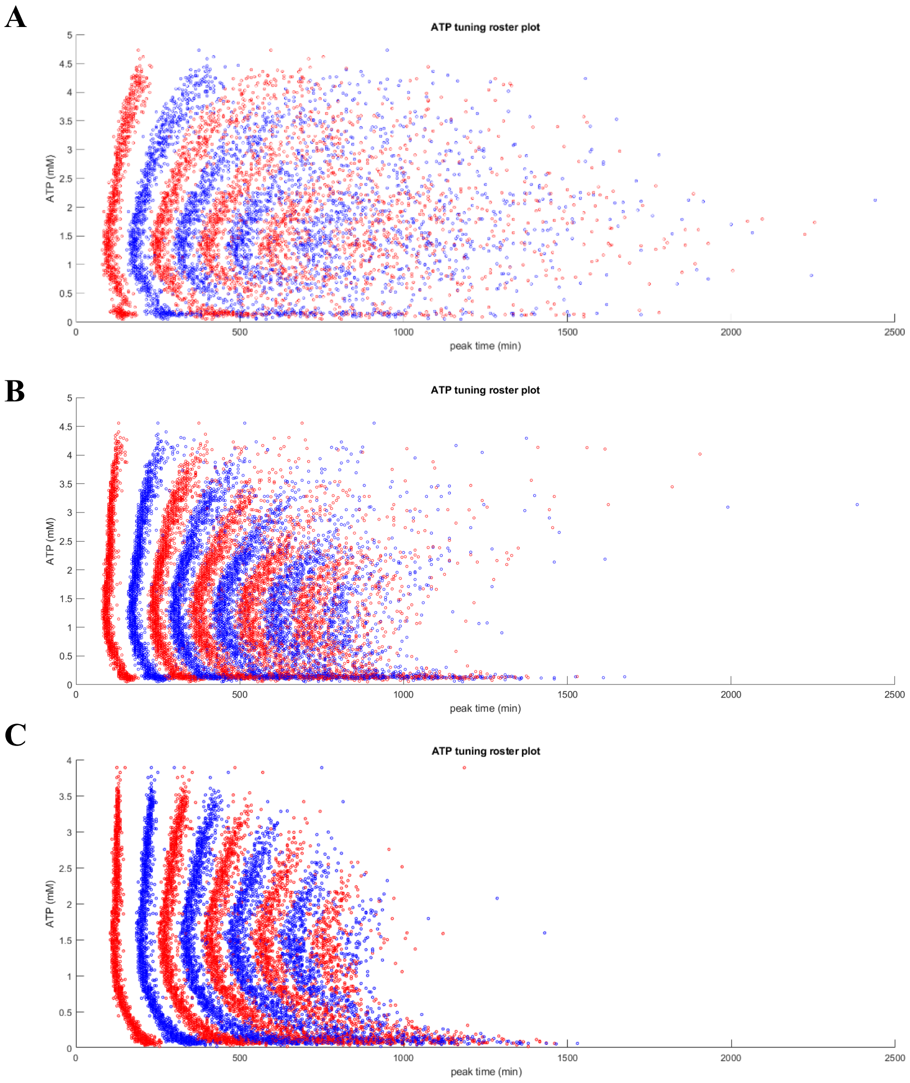

Figure 4.15. 2-channel ATP tuning at different Wee1 inhibition levels.

0 to 5mM ATP tuning when extract is supplied with (A) no PD166582, (B) 1μM PD166582, and (C) 5μM PD166582.

Chapter 5 Conclusions

5.1. Development of Droplet Microfluidics to Create Synthetic Cells at High-Throughput

In this dissertation, I have shown the development of a system suited for quantitatively studying complex biological systems. While the use of bulk extract has proven to be helpful in previous studies and contributed to various findings, the droplet system combined with microfluidic techniques has the distinct advantage of mimicking a cell's size and closed environment, as well as being able to generate thousands of replicates with very low sample volume. The droplet size can also be easily tuned by changing the pump pressure. In addition, the droplets are proven to maintain cell cycle dynamics much longer than their bulk counterparts. Chapter 2 has shown that combined with fluorescence microscopy, the system can successfully reconstitute and spatiotemporally track dynamic processes such as the Cdk1 activity during the mitotic cycle. Analysis on the effect of droplet size on the mitotic cycle also suggests the importance of reaction volume in biological processes, which casts doubt on the use of bulk extracts. Even though the focus of this dissertation and the application of the droplet system revolves around mitotic oscillations, in theory, any dynamic biological system that can be encapsulated can benefit from this pipeline. The versatility of the platform allows for endless possibilities. For example, Jin & Tavella studied the significance of cytoplasmic density in maintaining regular cell behavior by precisely diluting or condensing the xenopus extract[91]; Maryu studied the effect of nucleocytoplasmic compartmentalization on the cell's time-keeping capabilities by comparing the dynamics of the reconstituted mitotic circuit with and without nucleus and its corresponding transportation mechanisms[44]. Furthermore, the ability to produce large datasets comparable in sample size and scanning resolution to simulation results makes it a great tool for evaluating models and their prediction accuracies, as demonstrated in chapter 3 and 4. Continuous coverage of parameter ranges allows observations of changes in response to minute shifts in system conditions, making it an ideal candidate and visualization tool when conducting complex bifurcation analyses. The ability to change cellular environments also makes it possible to study far-from-equilibrium systems and their response to perturbations. Furthermore, while computational studies can perform blanket scans of network motifs and individual elements to analyze their functions, it would be extremely challenging to do so *in vivo* in complex organisms. With cell-free extracts, it is possible to achieve affects similar to computational methods by constructing artificial molecular networks or modifying existing ones. In this dissertation, I mainly used fluorescence microscopy to track temporal dynamics of a single cell cycle-related molecule, however the droplet system has the capacity to simultaneously record temporal and spatial profiles of multiple species. It can also output other types of information such as heat release, oxygen consumption and production when combined with reporting mechanisms other than fluorescence.

Despite the multitudes of advantages the droplet system brings, there is still space for improvement that can make the system even more accessible. While the cell membrane consists of a double lipid layer and embedded complexes, thus allowing selective transportation of certain molecules, the membrane of our droplets consists of a single layer of surfactant with the hydrophobic end facing outwards, in theory making the inside of droplets a completely isolated environment. Therefore, the system does not allow for almost any kind of manipulation post droplet generation. Although we have explored some optogenetic tools and caged molecules activatable by light, more testing needs to be done to prove its feasibility. The system is also not compatible with techniques that require fixed samples. Although some parallel experiments can be set up by allocating some extract for those kinds of tests besides droplet generation, they are almost always bulk extracts which might have different behaviors. Recovering extracts from already generated droplets is quite difficult. Furthermore, there is some evidence that tightly packed droplets might be able to exchange their contents with their neighbors[92], which might create complications for extract content tuning experiments, although this is less studied and not well characterized. Nevertheless, our high-throughput, cell-free, droplet-based system provides a powerful platform to study complex biological systems and has the potential to be applied to broader fields of study.

5.2. Future Explorations to Understand Biological Oscillators

For the ongoing research described in Chapter 4, there are multiple interesting directions to explore, as mentioned in the conclusion. Some questions of immediate interest include detailed characterization of the energy production/consumption in cycling extracts and ways to quantitatively manipulate them. ITC can measure heat release fluctuation with high sensitivity, which might give us temporal patterns of ATP consumption; real-time cell metabolic analysis can detect temporal patterns of ATP production and consumption. As some works have pointed out the significance of free energy dissipation, which is determined by [ATP]/[ADP], it would be extremely informative to include fluorescent [ATP]/[ADP] ratio reporters in the droplet. For precise manipulation, instead of adding ATP or apyrase, other methods include mitochondrial inhibition and making high-speed cycling extracts, from which mitochondria are removed completely and can then be gradually titrated, creating a purer system. It would also be interesting to dissect how the mitotic circuit receives the environmental cue of energy level and adapt accordingly by changing oscillator behavior. Our current assumption is that this kind of response is achieved through the Wee1/Cdc25 feedback loops, however more experimental evidence is needed. Although theoretical works about noise regulation in oscillators abound, experimental verification significantly lagged. My research project and its future potential can fill in the blanks.

In broader terms, the conceptualization of probing dynamics ensembles in biological systems can help solve theoretical problems in fields such as complex systems previously not thought reproducible in real life, just as the energy project described in Chapter 4 can contribute to the study of thermodynamic uncertainty relations. Taking advantage of the droplet system's ability to mimic random parameter scans of a computer simulation, there is no doubt it can be used to untangle complex cellular dynamics in the future.

Bibliography

(1) Roenneberg, T.; Merrow, M. The Circadian Clock and Human Health. *Curr. Biol.* **2016**, *26* (10), R432–R443. https://doi.org/10.1016/j.cub.2016.04.011.

(2) Diaz-Cuadros, M.; Pourquie, O. In Vitro Systems: A New Window to the Segmentation Clock. *Dev. Growth Differ.* **2021**, *63* (2), 140–153. https://doi.org/10.1111/dgd.12710.

(3) Hubaud, A.; Regev, I.; Mahadevan, L.; Pourquié, O. Excitable Dynamics and Yap-Dependent Mechanical Cues Drive the Segmentation Clock. *Cell* **2017**, *171* (3), 668-682.e11. https://doi.org/10.1016/j.cell.2017.08.043.

(4) Delaune, E. A.; François, P.; Shih, N. P.; Amacher, S. L. Single-Cell-Resolution Imaging of the Impact of Notch Signaling and Mitosis on Segmentation Clock Dynamics. *Dev. Cell* **2012**, *23* (5), 995–1005. https://doi.org/10.1016/j.devcel.2012.09.009.

(5) Kamenz, J.; Gelens, L.; Ferrell, J. E. Bistable, Biphasic Regulation of PP2A-B55 Accounts for the Dynamics of Mitotic Substrate Phosphorylation. *Curr. Biol.* **2021**, *31* (4), 794-808.e6. https://doi.org/10.1016/j.cub.2020.11.058.

(6) Murray, A. W. Cell Cycle Extracts. *Methods Cell Biol.* **1991**, *36*, 581–605.

(7) Masui, Y.; Markert, C. L. Cytoplasmic Control of Nuclear Behavior during Meiotic Maturation of Frog Oocytes. *J. Exp. Zool.* **1971**, *177* (2), 129–145. https://doi.org/10.1002/jez.1401770202.

(8) Murray, A. W.; Kirschner, M. W. Dominoes and Clocks: The Union of Two Views of the Cell Cycle. *Science* **1989**, *246* (4930), 614–621. https://doi.org/10.1126/science.2683077.

(9) Lohka, M. J.; Maller, J. L. Induction of Nuclear Envelope Breakdown, Chromosome Condensation, and Spindle Formation in Cell-Free Extracts. *J. Cell Biol.* **1985**, *101* (2), 518–523. https://doi.org/10.1083/jcb.101.2.518.

(10) Lohka, M. J.; Hayes, M. K.; Maller, J. L. Purification of Maturation-Promoting Factor, an Intracellular Regulator of Early Mitotic Events. *Proc. Natl. Acad. Sci.* **1988**, *85* (9), 3009–3013. https://doi.org/10.1073/pnas.85.9.3009.

(11) Hannak, E.; Heald, R. Investigating Mitotic Spindle Assembly and Function in Vitro Using Xenopus Laevis Egg Extracts. *Nat. Protoc.* **2006**, *1* (5), 2305–2314. https://doi.org/10.1038/nprot.2006.396.

(12) Heald, R.; Tournebize, R.; Blank, T.; Sandaltzopoulos, R.; Becker, P.; Hyman, A.; Karsenti, E. Self-Organization of Microtubules into Bipolar Spindles around Artificial Chromosomes in Xenopus Egg Extracts. *Nature* **1996**, *382* (6590), 420–425. https://doi.org/10.1038/382420a0.

(13) Görlich, D.; Prehn, S.; Laskey, R. A.; Hartmann, E. Isolation of a Protein That Is Essential for the First Step of Nuclear Protein Import. *Cell* **1994**, *79* (5), 767–778. https://doi.org/10.1016/0092-8674(94)90067-1.

(14) Hirano, T.; Mitchison, T. J. A Heterodimeric Coiled-Coil Protein Required for Mitotic Chromosome Condensation in Vitro. *Cell* **1994**, *79* (3), 449–458. https://doi.org/10.1016/0092-8674(94)90254-2.

(15) Hirano, T.; Kobayashi, R.; Hirano, M. Condensins, Chromosome Condensation Protein Complexes Containing XCAP-C, XCAP-E and a Xenopus Homolog of the Drosophila Barren Protein. *Cell* **1997**, *89* (4), 511–521. https://doi.org/10.1016/S0092-8674(00)80233-0.

(16) Novak, B.; Tyson, J. J. Modeling the Cell Division Cycle: M-Phase Trigger, Oscillations, and Size Control. *J. Theor. Biol.* **1993**, *165* (1), 101–134. https://doi.org/10.1006/jtbi.1993.1179.

(17) Novak, B.; Tyson, J. J. Numerical Analysis of a Comprehensive Model of M-Phase Control in Xenopus Oocyte Extracts and Intact Embryos. *J. Cell Sci.* **1993**, *106 (Pt 4)*, 1153–1168. https://doi.org/10.1242/jcs.106.4.1153.

(18) Tyson, J. J.; Novak, B. Bistability, Oscillations, and Traveling Waves in Frog Egg Extracts. *Bull. Math. Biol.* **2015**, *77* (5), 796–816. https://doi.org/10.1007/s11538-014-0009-9.

(19) *KEGG PATHWAY: Cell cycle - Xenopus laevis (African clawed frog).* https://www.genome.jp/pathway/xla04110 (accessed 2023-10-12).

(20) Den Haese, G. J.; Walworth, N.; Carr, A. M.; Gould, K. L. The Wee1 Protein Kinase Regulates T14 Phosphorylation of Fission Yeast Cdc2. *Mol. Biol. Cell* **1995**, *6* (4), 371–385.

(21) Strausfeld, U.; Labbé, J. C.; Fesquet, D.; Cavadore, J. C.; Picard, A.; Sadhu, K.; Russell, P.; Dorée, M. Dephosphorylation and Activation of a P34cdc2/Cyclin B Complex in Vitro by Human CDC25 Protein. *Nature* **1991**, *351* (6323), 242–245. https://doi.org/10.1038/351242a0.

(22) Tsai, T. Y.-C.; Choi, Y. S.; Ma, W.; Pomerening, J. R.; Tang, C.; Ferrell, J. E. Robust, Tunable Biological Oscillations from Interlinked Positive and Negative Feedback Loops. *Science* **2008**, *321* (5885), 126–129. https://doi.org/10.1126/science.1156951.

(23) Sha, W.; Moore, J.; Chen, K.; Lassaletta, A. D.; Yi, C.-S.; Tyson, J. J.; Sible, J. C. Hysteresis Drives Cell-Cycle Transitions in Xenopus Laevis Egg Extracts. *Proc. Natl. Acad. Sci.* **2003**, *100* (3), 975–980. https://doi.org/10.1073/pnas.0235349100.

(24) Pomerening, J. R.; Sontag, E. D.; Ferrell, J. E. Building a Cell Cycle Oscillator: Hysteresis and Bistability in the Activation of Cdc2. *Nat. Cell Biol.* **2003**, *5* (4), 346–351. https://doi.org/10.1038/ncb954.

(25) Yang, Q.; Ferrell, J. E. The Cdk1–APC/C Cell Cycle Oscillator Circuit Functions as a Time-Delayed, Ultrasensitive Switch. *Nat. Cell Biol.* **2013**, *15* (5), 519–525. https://doi.org/10.1038/ncb2737.

(26) Li, Z.; Liu, S.; Yang, Q. Incoherent Inputs Enhance the Robustness of Biological Oscillators. *Cell Syst.* **2017**, *5* (1), 72-81.e4. https://doi.org/10.1016/j.cels.2017.06.013.

(27) Cao, Y.; Wang, H.; Ouyang, Q.; Tu, Y. The Free Energy Cost of Accurate Biochemical Oscillations. *Nat. Phys.* **2015**, *11* (9), 772–778. https://doi.org/10.1038/nphys3412.

(28) Wang, T.; Zhao, J.; Ouyang, Q.; Qian, H.; Fu, Y. V.; Li, F. Phosphorylation Energy and Nonlinear Kinetics as Key Determinants for G2/M Transition in Fission Yeast Cell Cycle. arXiv October 30, 2016. https://doi.org/10.48550/arXiv.1610.09637.

(29) Peters, R. J. R. W.; Marguet, M.; Marais, S.; Fraaije, M. W.; van Hest, J. C. M.; Lecommandoux, S. Cascade Reactions in Multicompartmentalized Polymersomes. *Angew. Chem. Int. Ed.* **2014**, *53* (1), 146–150. https://doi.org/10.1002/anie.201308141.

(30) Peyret, A.; Ibarboure, E.; Pippa, N.; Lecommandoux, S. Liposomes in Polymersomes: Multicompartment System with Temperature-Triggered Release. *Langmuir* **2017**, *33* (28), 7079–7085. https://doi.org/10.1021/acs.langmuir.7b00655.

(31) Kumar, B. V. V. S. P.; Patil, A. J.; Mann, S. Enzyme-Powered Motility in Buoyant Organoclay/DNA Protocells. *Nat. Chem.* **2018**, *10* (11), 1154–1163. https://doi.org/10.1038/s41557-018-0119-3.

(32) Groaz, A.; Moghimianavval, H.; Tavella, F.; Giessen, T. W.; Vecchiarelli, A. G.; Yang, Q.; Liu, A. P. Engineering Spatiotemporal Organization and Dynamics in Synthetic Cells. *WIREs Nanomedicine Nanobiotechnology* **2021**, *13* (3), e1685. https://doi.org/10.1002/wnan.1685.

(33) Majumder, S.; Wubshet, N.; Liu, A. P. Encapsulation of Complex Solutions Using Droplet Microfluidics towards the Synthesis of Artificial Cells. *J. Micromechanics Microengineering* **2019**, *29* (8), 083001. https://doi.org/10.1088/1361-6439/ab2377.

(34) Trantidou, T.; S. Friddin, M.; Salehi-Reyhani, A.; Ces, O.; Elani, Y. Droplet Microfluidics for the Construction of Compartmentalised Model Membranes. *Lab. Chip* **2018**, *18* (17), 2488–2509. https://doi.org/10.1039/C8LC00028J.

(35) Vogele, K.; Frank, T.; Gasser, L.; Goetzfried, M. A.; Hackl, M. W.; Sieber, S. A.; Simmel, F. C.; Pirzer, T. Towards Synthetic Cells Using Peptide-Based Reaction Compartments. *Nat. Commun.* **2018**, *9* (1), 3862. https://doi.org/10.1038/s41467-018-06379-8.

(36) Shinoda, T.; Shinya, N.; Ito, K.; Ishizuka-Katsura, Y.; Ohsawa, N.; Terada, T.; Hirata, K.; Kawano, Y.; Yamamoto, M.; Tomita, T.; Ishibashi, Y.; Hirabayashi, Y.; Kimura-Someya, T.; Shirouzu, M.; Yokoyama, S. Cell-Free Methods to Produce Structurally Intact Mammalian Membrane Proteins. *Sci. Rep.* **2016**, *6* (1), 30442. https://doi.org/10.1038/srep30442.

(37) Godino, E.; López, J. N.; Foschepoth, D.; Cleij, C.; Doerr, A.; Castellà, C. F.; Danelon, C. De Novo Synthesized Min Proteins Drive Oscillatory Liposome Deformation and Regulate FtsA-FtsZ Cytoskeletal Patterns. *Nat. Commun.* **2019**, *10* (1), 4969. https://doi.org/10.1038/s41467-019-12932-w.

(38) Guan, Y.; Li, Z.; Wang, S.; Barnes, P. M.; Liu, X.; Xu, H.; Jin, M.; Liu, A. P.; Yang, Q. A Robust and Tunable Mitotic Oscillator in Artificial Cells. *eLife* **2018**, *7*. https://doi.org/10.7554/eLife.33549.

(39) Giessen, T. W.; Silver, P. A. Encapsulation as a Strategy for the Design of Biological Compartmentalization. *J. Mol. Biol.* **2016**, *428* (5, Part B), 916–927. https://doi.org/10.1016/j.jmb.2015.09.009.

(40) Ganji, M.; Shaltiel, I. A.; Bisht, S.; Kim, E.; Kalichava, A.; Haering, C. H.; Dekker, C. Real-Time Imaging of DNA Loop Extrusion by Condensin. *Science* **2018**, *360* (6384), 102–105. https://doi.org/10.1126/science.aar7831.

(41) Hwang, L. C.; Vecchiarelli, A. G.; Han, Y.; Mizuuchi, M.; Harada, Y.; Funnell, B. E.; Mizuuchi, K. ParA-mediated Plasmid Partition Driven by Protein Pattern Self-organization. *EMBO J.* **2013**, *32* (9), 1238–1249. https://doi.org/10.1038/emboj.2013.34.

(42) Litschel, T.; Ramm, B.; Maas, R.; Heymann, M.; Schwille, P. Beating Vesicles: Encapsulated Protein Oscillations Cause Dynamic Membrane Deformations. *Angew. Chem. Int. Ed.* **2018**, *57* (50), 16286–16290. https://doi.org/10.1002/anie.201808750.

(43) Puls, O.; Ruiz-Reynés, D.; Tavella, F.; Jin, M.; Kim, Y.; Gelens, L.; Yang, Q. Mitotic Waves in Frog Egg Extracts: Transition from Phase Waves to Trigger Waves. bioRxiv January 23, 2024, p 2024.01.18.576267. https://doi.org/10.1101/2024.01.18.576267.

(44) Maryu, G.; Yang, Q. Nuclear-Cytoplasmic Compartmentalization of Cyclin B1-Cdk1 Promotes Robust Timing of Mitotic Events. *Cell Rep.* **2022**, *41* (13), 111870. https://doi.org/10.1016/j.celrep.2022.111870.

(45) Guan, Y.; Wang, S.; Jin, M.; Xu, H.; Yang, Q. Reconstitution of Cell-Cycle Oscillations in Microemulsions of Cell-Free Xenopus Egg Extracts. *J. Vis. Exp.* **2018**, No. 139. https://doi.org/10.3791/58240.

(46) Sun, M.; Li, Z.; Wang, S.; Maryu, G.; Yang, Q. Building Dynamic Cellular Machineries in Droplet-Based Artificial Cells with Single-Droplet Tracking and Analysis. *Anal. Chem.* **2019**, *91* (15), 9813–9818. https://doi.org/10.1021/acs.analchem.9b01481.

(47) Sun, M.; Maryu, G.; Wang, S.; Yang, Q.; Bailey, R. C. Plug-in Tubes Allow Tunable Oil Removal, Droplet Packing, and Reaction Incubation for Time-Controlled Droplet-Based Assays. *Biomicrofluidics* **2021**, *15* (2), 024108. https://doi.org/10.1063/5.0047924.

(48) Li, Z.; Wang, S.; Sun, M.; Jin, M.; Khain, D.; Yang, Q. Comprehensive Parameter Space Mapping of Cell Cycle Dynamics under Network Perturbations. *ACS Synth. Biol.* **2024**, *13* (3), 804–815. https://doi.org/10.1021/acssynbio.3c00631.

(49) Pomerening, J. R.; Kim, S. Y.; Ferrell, J. E. Systems-Level Dissection of the Cell-Cycle Oscillator: Bypassing Positive Feedback Produces Damped Oscillations. *Cell* **2005**, *122* (4), 565–578. https://doi.org/10.1016/j.cell.2005.06.016.

(50) Nakajima, M.; Imai, K.; Ito, H.; Nishiwaki, T.; Murayama, Y.; Iwasaki, H.; Oyama, T.; Kondo, T. Reconstitution of Circadian Oscillation of Cyanobacterial KaiC Phosphorylation in Vitro. *Science* **2005**, *308* (5720), 414–415. https://doi.org/10.1126/science.1108451.

(51) Ho, K. K. Y.; Lee, J. W.; Durand, G.; Majumder, S.; Liu, A. P. Protein Aggregation with Poly(Vinyl) Alcohol Surfactant Reduces Double Emulsion-Encapsulated Mammalian Cell-Free Expression. *PLOS ONE* **2017**, *12* (3), e0174689. https://doi.org/10.1371/journal.pone.0174689.

(52) Good, M. C.; Vahey, M. D.; Skandarajah, A.; Fletcher, D. A.; Heald, R. Cytoplasmic Volume Modulates Spindle Size During Embryogenesis. *Science* **2013**, *342* (6160), 856–860. https://doi.org/10.1126/science.1243147.

(53) Kumagai, A.; Dunphy, W. G. Regulation of the Cdc25 Protein during the Cell Cycle in Xenopus Extracts. *Cell* **1992**, *70* (1), 139–151. https://doi.org/10.1016/0092-8674(92)90540-S.

(54) Mueller, P. R.; Coleman, T. R.; Dunphy, W. G. Cell Cycle Regulation of a Xenopus Wee1-like Kinase. *Mol. Biol. Cell* **1995**, *6* (1), 119–134. https://doi.org/10.1091/mbc.6.1.119.

(55) Chang, J. B.; Ferrell, J. E. Mitotic Trigger Waves and the Spatial Coordination of the Xenopus Cell Cycle. *Nature* **2013**, *500* (7464), 603–607. https://doi.org/10.1038/nature12321.

(56) Trunnell, N. B.; Poon, A. C.; Kim, S. Y.; Ferrell, J. E. Ultrasensitivity in the Regulation of Cdc25C by Cdk1. *Mol. Cell* **2011**, *41* (3), 263–274. https://doi.org/10.1016/j.molcel.2011.01.012.

(57) Kim, S. Y.; Ferrell, J. E. Substrate Competition as a Source of Ultrasensitivity in the Inactivation of Wee1. *Cell* **2007**, *128* (6), 1133–1145. https://doi.org/10.1016/j.cell.2007.01.039.

(58) Thron, C. D. A Model for a Bistable Biochemical Trigger of Mitosis. *Biophys. Chem.* **1996**, *57* (2–3), 239–251. https://doi.org/10.1016/0301-4622(95)00075-5.

(59) Rust, M. J.; Markson, J. S.; Lane, W. S.; Fisher, D. S.; O'Shea, E. K. Ordered Phosphorylation Governs Oscillation of a Three-Protein Circadian Clock. *Science* **2007**, *318* (5851), 809–812. https://doi.org/10.1126/science.1148596.

(60) Hoffmann, A.; Levchenko, A.; Scott, M. L.; Baltimore, D. The IκB-NF-κB Signaling Module: Temporal Control and Selective Gene Activation. *Science* **2002**, *298* (5596), 1241–1245. https://doi.org/10.1126/science.1071914.

(61) Cross, F. R. Two Redundant Oscillatory Mechanisms in the Yeast Cell Cycle. *Dev. Cell* **2003**, *4* (5), 741–752. https://doi.org/10.1016/S1534-5807(03)00119-9.

(62) Lee, K.; Loros, J. J.; Dunlap, J. C. Interconnected Feedback Loops in the Neurospora Circadian System. *Science* **2000**, *289* (5476), 107–110. https://doi.org/10.1126/science.289.5476.107.

(63) Weitz, M.; Kim, J.; Kapsner, K.; Winfree, E.; Franco, E.; Simmel, F. C. Diversity in the Dynamical Behaviour of a Compartmentalized Programmable Biochemical Oscillator. *Nat. Chem.* **2014**, *6* (4), 295–302. https://doi.org/10.1038/nchem.1869.

(64) Matthaei, J. H.; Jones, O. W.; Martin, R. G.; Nirenberg, M. W. Characteristics and Composition of Rna Coding Units*. *Proc. Natl. Acad. Sci.* **1962**, *48* (4), 666–677. https://doi.org/10.1073/pnas.48.4.666.

(65) Noireaux, V.; Bar-Ziv, R.; Libchaber, A. Principles of Cell-Free Genetic Circuit Assembly. *Proc. Natl. Acad. Sci.* **2003**, *100* (22), 12672–12677. https://doi.org/10.1073/pnas.2135496100.

(66) Marshall, R.; Maxwell, C. S.; Collins, S. P.; Jacobsen, T.; Luo, M. L.; Begemann, M. B.; Gray, B. N.; January, E.; Singer, A.; He, Y.; Beisel, C. L.; Noireaux, V. Rapid and Scalable Characterization of CRISPR Technologies Using an E. Coli Cell-Free Transcription-Translation System. *Mol. Cell* **2018**, *69* (1), 146-157.e3. https://doi.org/10.1016/j.molcel.2017.12.007.

(67) Yamamoto, T.; Fujii, T.; Nojima, T. PDMS–Glass Hybrid Microreactor Array with Embedded Temperature Control Device. Application to Cell-Free Protein Synthesis. *Lab. Chip* **2002**, *2* (4), 197–202. https://doi.org/10.1039/B205010B.

(68) Maerkl, S. J.; Quake, S. R. A Systems Approach to Measuring the Binding Energy Landscapes of Transcription Factors. *Science* **2007**, *315* (5809), 233–237. https://doi.org/10.1126/science.1131007.

(69) Stögbauer, T.; Windhager, L.; Zimmer, R.; Rädler, J. O. Experiment and Mathematical Modeling of Gene Expression Dynamics in a Cell-Free System. *Integr. Biol.* **2012**, *4* (5), 494–501. https://doi.org/10.1039/c2ib00102k.

(70) Almouzni, G.; Wolffe, A. P. Constraints on Transcriptional Activator Function Contribute to Transcriptional Quiescence during Early Xenopus Embryogenesis. *EMBO J.* **1995**, *14* (8), 1752–1765. https://doi.org/10.1002/j.1460-2075.1995.tb07164.x.

(71) Gilbert, D. A. The Nature of the Cell Cycle and the Control of Cell Proliferation. *Curr. Mod. Biol.* **1974**, *5* (4), 197–206. https://doi.org/10.1016/0303-2647(74)90032-x.

(72) Masui, Y.; Wang, P. Cell Cycle Transition in Early Embryonic Development of Xenopus Laevis. *Biol. Cell* **1998**, *90* (8), 537–548. https://doi.org/10.1016/S0248-4900(99)80011-2.

(73) Tyson, J. J.; Novák, B. Models in Biology: Lessons from Modeling Regulation of the Eukaryotic Cell Cycle. *BMC Biol.* **2015**, *13*, 46. https://doi.org/10.1186/s12915-015-0158-9.

(74) Krasinska, L.; Domingo-Sananes, M. R.; Kapuy, O.; Parisis, N.; Harker, B.; Moorhead, G.; Rossignol, M.; Novák, B.; Fisher, D. Protein Phosphatase 2A Controls the Order and Dynamics of

Cell-Cycle Transitions. *Mol. Cell* **2011**, *44* (3), 437–450. https://doi.org/10.1016/j.molcel.2011.10.007.

(75) Mochida, S.; Rata, S.; Hino, H.; Nagai, T.; Novák, B. Two Bistable Switches Govern M Phase Entry. *Curr. Biol.* **2016**, *26* (24), 3361–3367. https://doi.org/10.1016/j.cub.2016.10.022.

(76) Rata, S.; Suarez Peredo Rodriguez, M. F.; Joseph, S.; Peter, N.; Echegaray Iturra, F.; Yang, F.; Madzvamuse, A.; Ruppert, J. G.; Samejima, K.; Platani, M.; Alvarez-Fernandez, M.; Malumbres, M.; Earnshaw, W. C.; Novak, B.; Hochegger, H. Two Interlinked Bistable Switches Govern Mitotic Control in Mammalian Cells. *Curr. Biol.* **2018**, *28* (23), 3824-3832.e6. https://doi.org/10.1016/j.cub.2018.09.059.

(77) Panek, R. L.; Lu, G. H.; Klutchko, S. R.; Batley, B. L.; Dahring, T. K.; Hamby, J. M.; Hallak, H.; Doherty, A. M.; Keiser, J. A. In Vitro Pharmacological Characterization of PD 166285, a New Nanomolar Potent and Broadly Active Protein Tyrosine Kinase Inhibitor. *J. Pharmacol. Exp. Ther.* **1997**, *283* (3), 1433–1444.

(78) Wlodarchak, N.; Xing, Y. PP2A as a Master Regulator of the Cell Cycle. *Crit. Rev. Biochem. Mol. Biol.* **2016**, *51* (3), 162–184. https://doi.org/10.3109/10409238.2016.1143913.

(79) Bialojan, C.; Takai, A. Inhibitory Effect of a Marine-Sponge Toxin, Okadaic Acid, on Protein Phosphatases. Specificity and Kinetics. *Biochem. J.* **1988**, *256* (1), 283–290. https://doi.org/10.1042/bj2560283.

(80) Barato, A. C.; Seifert, U. Thermodynamic Uncertainty Relation for Biomolecular Processes. *Phys. Rev. Lett.* **2015**, *114* (15), 158101. https://doi.org/10.1103/PhysRevLett.114.158101.

(81) Tsai, T. Y.-C.; Theriot, J. A.; Ferrell, J. E. Changes in Oscillatory Dynamics in the Cell Cycle of Early Xenopus Laevis Embryos. *PLoS Biol.* **2014**, *12* (2), e1001788. https://doi.org/10.1371/journal.pbio.1001788.

(82) Zotin, A. I.; Faustov, V. S.; Radzinskaja, L. I.; Ozernyuk, N. D. ATP Level and Respiration of Embryos. *J. Embryol. Exp. Morphol.* **1967**, *18* (1), 1–12.

(83) Ciliberto, A.; Novak, B.; Tyson, J. J. Mathematical Model of the Morphogenesis Checkpoint in Budding Yeast. *J. Cell Biol.* **2003**, *163* (6), 1243–1254. https://doi.org/10.1083/jcb.200306139.

(84) Hochegger, H.; Klotzbücher, A.; Kirk, J.; Howell, M.; le Guellec, K.; Fletcher, K.; Duncan, T.; Sohail, M.; Hunt, T. New B-Type Cyclin Synthesis Is Required between Meiosis I and II during Xenopus Oocyte Maturation. *Dev. Camb. Engl.* **2001**, *128* (19), 3795–3807. https://doi.org/10.1242/dev.128.19.3795.

(85) Kobayashi, H.; Golsteyn, R.; Poon, R.; Stewart, E.; Gannon, J.; Minshull, J.; Smith, R.; Hunt, T. Cyclins and Their Partners during Xenopus Oocyte Maturation. *Cold Spring Harb. Symp. Quant. Biol.* **1991**, *56*, 437–447. https://doi.org/10.1101/SQB.1991.056.01.051.

(86) Kobayashi, H.; Stewart, E.; Poon, R. Y.; Hunt, T. Cyclin A and Cyclin B Dissociate from P34cdc2 with Half-Times of 4 and 15 h, Respectively, Regardless of the Phase of the Cell Cycle. *J. Biol. Chem.* **1994**, *269* (46), 29153–29160. https://doi.org/10.1016/S0021-9258(19)62024-7.

(87) Kampen, N. G. V. *Stochastic Processes in Physics and Chemistry*; Elsevier, 1992.

(88) Gillespie, D. T. Exact Stochastic Simulation of Coupled Chemical Reactions. *J. Phys. Chem.* **1977**, *81* (25), 2340–2361. https://doi.org/10.1021/j100540a008.

(89) Tuck, C.; Zhang, T.; Potapova, T.; Malumbres, M.; Novák, B. Robust Mitotic Entry Is Ensured by a Latching Switch. *Biol. Open* **2013**, *2* (9), 924–931. https://doi.org/10.1242/bio.20135199.

(90) Rodenfels, J.; Neugebauer, K. M.; Howard, J. Heat Oscillations Driven by the Embryonic Cell Cycle Reveal the Energetic Costs of Signaling. *Dev. Cell* **2019**, *48* (5), 646-658.e6. https://doi.org/10.1016/j.devcel.2018.12.024.

(91) Jin, M.; Tavella, F.; Wang, S.; Yang, Q. In Vitro Cell Cycle Oscillations Exhibit a Robust and Hysteretic Response to Changes in Cytoplasmic Density. *Proc. Natl. Acad. Sci. U. S. A.* **2022**, *119* (6). https://doi.org/10.1073/pnas.2109547119.

(92) Gonzales, D. T.; Suraritdechachai, S.; Zechner, C.; Tang, T.-Y. D. Bidirectional Communication between Droplet Interface Bilayers Driven by Cell-Free Quorum Sensing Gene Circuits**. *ChemSystemsChem* **2023**, *5* (6), e202300029. https://doi.org/10.1002/syst.202300029.